Hydrodynamics & Elasticity with Interfaces

Arnaud Antkowiak

Hydrodynamics &
Elasticity
with Interfaces

Arnaud Antkowiak

Hydrodynamics
&
Elasticity
with Interfaces

Fig. 1

"Now I shall begin by performing an experiment which you have all probably tried dozens of times without recognizing that you were making an experiment at all. I have in my hand a common camel's-hair brush. If you want to make the hairs cling together and come to a point, you wet it, and then you say the hairs cling together because the brush is wet. Now let us try the experiment; but, as you cannot see this brush across the room, I hold it in the lantern, and you can see it enlarged upon the screen (Fig. 1, left hand). Now it is dry, and the hairs are separately visible. I am now dipping it in the water, as you can see, and, on taking it out, the hairs, as we expected, cling together (Fig. 1, right hand), because they are wet, as we are in the habit of saying. I shall now hold the brush in the water, but there it is evident that the hairs do not cling at all (Fig. 1, middle), and yet they surely are wet now, being actually in the water. It would appear then that the reason which we always give is not exactly correct. This experiment, which requires nothing more than a brush and a glass of water, then, shows that the hairs of a brush cling together not only because they are wet, but for some other reason as well which we do not yet know."

Charles Vernon Boys, excerpt from the first lecture ("The elastic skin of liquids") of a series of three delivered in the theatre of the London institution on the afternoons of Dec. 30, 1889, Jan. 1 and 3, 1890, before a juvenile audience. (Boys, 1890).

Contents

À Claire, Jules, Marius & Aurèle

Introduction

I have had the chance to perform my PhD thesis in Toulouse under the supervision of Pierre Brancher. The core idea of the thesis was then to investigate how a vortex reacts when disturbed. From the understanding of the vortex' behavioural properties, we wanted to design smart perturbations that would destroy (or, more realistically, bother significantly) the vortex. Although the tools we used for this investigation were quite technical, I remember from these years that we kept on focusing on the physics underpinning the phenomena at play – physics which can be somewhat dimmed behind technicalities. And this is probably the foremost learning that I retain from these last student years: a tropism to understand the physics underlying vortices, and flows in general. After all, this is what it is all about: fluid mechanics, and more broadly mechanics, is physics at the human scale.

With this is mind, I then moved to Marseille where I did a postdoc with Emmanuel Villermaux and Stéphane Le Dizès on the formation of stretched liquid jets, a topic that I later continued to work on (see chapter 1). There I changed the object of study and the tools, but not the general approach. I also made my first steps as an experimentalist (who "confronts with realness") in Marseille and I am indebted to Emmanuel for this, because these first years preluded and shaped the way I conduct research since then.

I came to Paris in 2007 to live the last months of the LMM (Laboratoire de Modélisation en Mécanique) and be part of the newly formed Institut d'Alembert. This lab, whose trademark was theory and numerical analysis, was by the time welcoming an experimental touch. Aided by the university and CNRS, and also by the Ville de Paris and an ANR grant I was lucky to get, I therefore set up a small experimental lab within the institute: la salle Savart. This small experimental facility allowed me to take further the study of liquid jets resulting from the relaxation of bubbles (postdoc Thomas Séon) or cavities (PhD thesis Élisabeth Ghabache) but also to follow new tracks. Among these, I have to quote particularly the broad field of elastic deformation of thin structures imparted by capillarity, which we have investigated with Christophe Josserand, Basile Audoly, Sébastien Neukirch and several PhD students (Marco Rivetti, Hervé Elettro, Aurélie Fargette and Paul Grandgeorge). At this point I have to stress how important a role have colleagues and students played in my scientific life. I have been most lucky to meet nice and skilful researchers since I arrived in this lab, especially of different horizons. In particular I have launched into the field of elastocapillarity thanks to colloboration with next-door elasticity experts, and Sébastien Neukirch especially. PhD students have obviously played a central

role since my arrival and I am most thankful to each of them for sharing a three-years research adventure (Marco, Elisabeth, Hervé, Julien, Aurélie, Paul) – clearly most of the work presented in this document could not have been done without them.

We have now come a long way since the first experiments in Jussieu, and there has been so to speak a constant accretion of experimentalists onto the salle Savart through the years – which signs the success of the experiments implant in Jussieu. I truly believe this added facet makes d'Alembert a most unique site, mixing skills and expertise, devoted to this physics at the human scale.

In the following, I trace an account of my scientific trajectory so far, at the interface between liquids and solids.

1 | **Transient Jets**

Among the variety of liquid jets developing over scales ranging from microscopic up to astronomical (Eggers and Villermaux, 2008), transient jets or squirts bear a particular importance for they often are a signature of a rapid relaxation event: capillary levelling
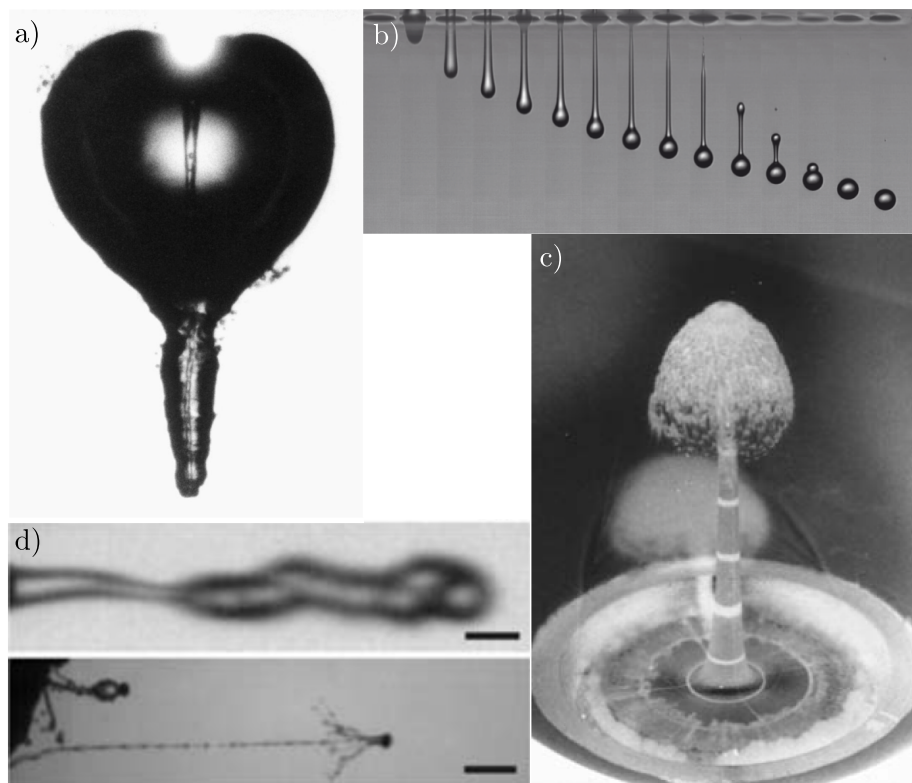
FIG. 1.1 – **A collection of transient liquid jets**. a) Cavitation jet developing inside a collapsing bubble (Brujan *et al.*, 2001; Popinet, 2000), b) Time-resolved chronophotography of a single drop produced in an inkjet setup (van der Bos *et al.*, 2014), c) Liquid metal jet traveling at 9.2 km/s produced by a shaped-charge weapon (snapshot taken 31.5 μs after detonation, Shaw *et al.*, 1994), d) Spore-carrying liquid squirts produced by fungi (Yafetto *et al.*, 2008).

of an interface after the bursting of a bubble, pressure reduction following an impact, a detonation, the piezoelectric compression of an ink chamber etc. As these jets develop they exhaust their source. As a result of this decaying feeding, these jets feature a marked stretching. In turn, this stretching affect the way capillary wavepackets ride over the jet surface (Frankel and Weihs, 1985) and select the final fragments, therefore determining the size distribution of e.g. spray aerosols.

In the following, we focus on the dynamics of such discharge jets, from their early formation up to their late development – prior to their disintegration.

1.1   A link between hydrodynamics and geometry

The overpressure initiating discharge jets may arise from quite different origins, as already illustrated in Fig. 1.1. But regardless of the nature of this pressure drive, the initial geometry of the free surface systematically plays a crucial role in the jet dynamics starting from its formation. We elucidate in the following this link for a few typical drivers.

1.1.1   Regular jet formation

Impact- or gravity-driven jets are typically rooted in a pressure field having the extent of the initial cavity or ripple deforming the free surface. Such jets have therefore a typical transverse size scaling with the initial cavity, i.e. are regular – as opposed to singular jets that develop following the self-similar focusing of cavity, see §1.1.2.

▷ **Impact-driven jets.**   Liquid impacts are often associated with thin and violent ejecta near the region where the liquid hits a surface: wave impact on dams (Peregrine, 2003), drop impact on ground (Josserand and Thoroddsen, 2016)... But impacts can also set free surface liquids into motion at a distance from the walls, provided the interface is curved. Probably the most elementary illustration of this fact is proposed with the experiment of Prof. Pokrovski that consists in impacting a test tube filled with a wetting liquid displaying a curved interface (sketch alongside excerpted from Lavrentiev and Chabat, 1980). Just after impact a fast and focused jet develops axially from the tube centre. While Pokrovski and collaborators initially thought that jet formation was the result of (acoustic) compressive waves focusing by the curved bottom, it soon became clear that it was not the case, for the same jet kept on developing in flat- and even concave-bottomed tubes. The key ingredient in jet formation is revealed with the experiments reported figure 1.2: free surface geometry. There, it can be seen that a tube filled with a wetting liquid, which has its interface quickly sculpted into an hemispherical meniscus during free fall, gives rise to a strong jet just after impact. Conversely a liquid contained in a tube chemically treated so that the contact angle is close to 90° sees
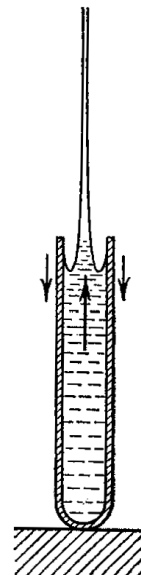
Note: We have not been able to find the original article of Pokrovski. But for completeness, let's note that this experiment is also presented in the PhD thesis of Tony Maxworthy (Maxworthy, 1960) and also in Milgram, (1969).
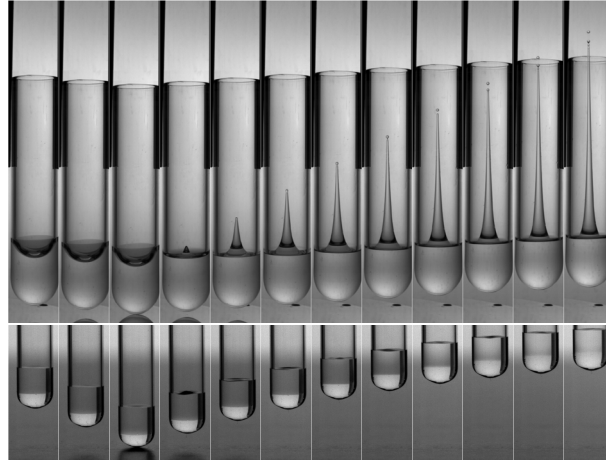
FIG. 1.2 – **Pokrovski's experiment.** Top: a tube filled with a wetting liquid freely falls axially. Upon impact on a rigid substrate, the interface curvature reverses violently and gives birth to an intense and concentrated jet (Antkowiak *et al.*, 2007a). Bottom: Similar experiment but with a silanized-glass tube displaying ca 90° contact angle with the carried fluid, making the interface flat during free-fall. Upon impact, the liquid now rebounds as a whole.

its interface kept flat during free fall. Upon impact the liquid rebounds with the container in a solid-body motion, without any deformation nor jet.
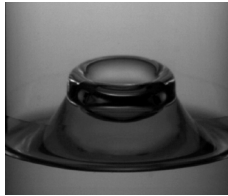
The critical role of interface geometry in jet formation can be witnessed by varying the surface shape. For example if the free surface is still in the process of relaxing to hemispherical shape when the tube hits the ground (because the liquid is too viscous, or the tube too large) the free surface imprints its shape to the jet, which now becomes annular (see inset). Other types of free surface corrugations – chiefly bubbles or foams – each produce a jet upon impact, with the jet typical radial length scaling with the cavity radius (Antkowiak *et al.*, 2007b). To shed light on the link between jet hydrodynamics and surface geometry, it is worth noting that over the impact duration, the velocity of the boundaries changes abruptly. This sudden velocity change is imparted in turn to the fluid particles by means of an intense pressure field, warrantying incompressibility throughout impact. Formally, the balance between these dominant terms of the Navier-Stokes equations reads:

$$\frac{\partial \boldsymbol{u}}{\partial t} = -\frac{1}{\rho} \nabla p. \tag{1.1}$$

As classic in water impact theory (Batchelor, 1967, §6.10; Cooker and Peregrine, 1995), we integrate this equation over the impact duration τ to get:

$$\boldsymbol{u}(\tau) - \boldsymbol{u}(0) = -\frac{1}{\rho} \nabla P, \tag{1.2}$$

where P is the pressure impulse defined as:

$$P = \int_0^\tau p \, dt. \tag{1.3}$$

The significance and importance of pressure impulse for liquid impact problems was revealed by Bagnold, (1939) who recorded experimentally the instantaneous pressures exerted by a breaking wave impacting a wall. Bagnold found that the data were highly scattered, presumably because of the ever varying precise interface shape and also of the multiple reflections of acoustic waves radiated from the boundaries. He also noted that the impact duration τ (based on the rise and fall of the pressure) was typically much larger (by a factor ten at least) than the acoustic timescale. But behind this apparent
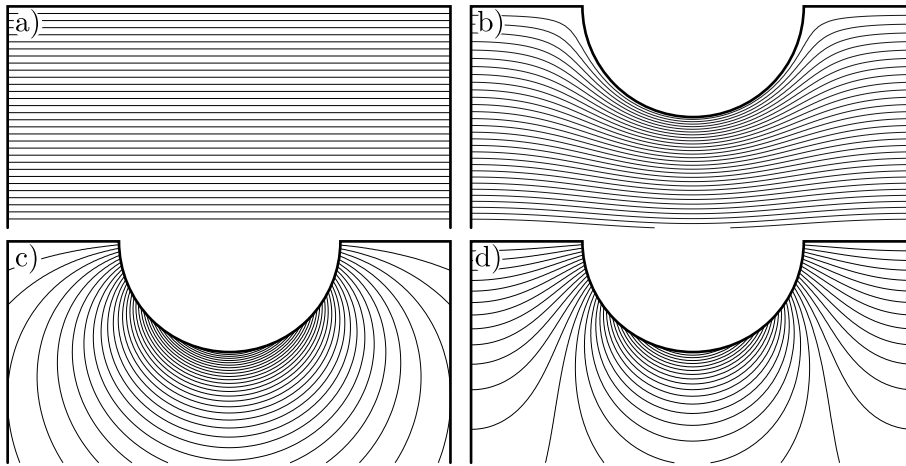
FIG. 1.3 - **Pressure impulse structure.** Top: Pressure impulse fields developed upon impact for different free surface geometries. a) For a flat free surface the pressure impulse field resembles a hydrostatic pressure field. b) When the free surface is dimpled, by a bubble for example, the spatial distribution of the pressure field is altered and a clustering of isobars under the cavity is observed. The resulting enhanced impulse pressure gradient preludes jet formation (Antkowiak *et al.*, 2007a). Bottom: Elementary solutions to Laplace equation. c) A classic spherical dipolar scalar field satisfies Laplace equation and the antisymmetry condition at $z = 0$ but fails to meet the homogeneous Neumann condition on the wall. d) Adding the correct amount of cylindrical elementary solutions to the previous solution forms a modified dipole having the desired properties on the wall.

irreproducibility the time integral of the pressure – the pressure impulse P – was found to be constant for given conditions. Actually there is no paradox here: while the global momentum transferred from a wave to the wall (the pressure impulse) is constant for given conditions, this momentum is built with a complex acoustic wavefield (the instantaneous pressure) that depend on the fine details of the setup. In such liquid impact problems, there is no need to grasp these intricate details to predict the velocity field post-impact,

as a global momentum balance already provides it, just as in the problem of billiard ball collision where there is no need to solve the elastic field to determine the direction of the balls.

To determine the pressure impulse setting off jet formation, we make use of equation (1.2). Incompressibility requires P to be an harmonic function:

$$\Delta P = 0 \tag{1.4}$$

associated with the impact boundary condition $\partial P/\partial z = -\rho U_0$ at the deep bottom, anti-symmetry conditions on the plane $z = 0$, homogeneous Neumann conditions $\partial P/\partial r = 0$ at the walls and an homogeneous Dirichlet condition $P = 0$ at the free surface. Here we have noted U_0 the velocity change of the boundaries imparted by impact. If the free surface is flat and lies in the plane $z = 0$, the pressure impulse is the trivial hydrostatic-like field $P_{\text{flat}} = -\rho U_0 z$. From equation (1.2) we see that such a field imparts homogeneously the velocity U_0 to each of the fluid particle: this is the solid-body rebound observed in Fig. 1.2. If the free surface is now dimpled by a meniscus or a bubble then there is a mismatch between the impact-induced pressure field P_{flat} and the free surface geometry. If the free surface deformation is spherical, we might calculate a correction to the homogeneous impulse pressure field P_{flat} involving the dipolar field $\phi(r, \theta) = -\partial r^{-1}/\partial z = \cos\theta/r^2$ and higher multipoles. The problem with such elementary solutions to Laplace equation in spherical co-ordinates is that the homogeneous Neumann condition is lost upon their addition. Knight, (1936) faced a similar problem when trying to derive the electrostatic potential surrounding a non-uniformly charged dielectric sphere placed inside a conductive cylinder. To cope with these different geometries, Knight devised a strategy consisting in performing a surgery to the dipole by adding to it the right amount of cylindrical elementary solutions to Laplace equation (i.e. Bessel functions) – so as not to break the conductive wall boundary conditions. We transpose this strategy to our problem and design a modified dipole F_0 by adding to $\phi(r, \theta)$ the function:

$$\varphi(\xi, z) = \int_0^\infty f(m) \sin(mz) I_0(m\xi) \, \mathrm{d}m, \tag{1.5}$$

where the weight function $f(m)$ is such that the normal derivatives of the singular (dipolar) and regular part balance each other along the wall, see Fig. 1.3. Let's remark that upon differentiating twice along z this solution, we obtain another elementary solution F_2 still complying with the boundary conditions, i.e. a higher-order modified multipole. Repeating this procedure we get an entire family of modified multipoles F_{2s}, and the impulse pressure P of our problem can be expressed as a weighted sum of these elementary functions:

$$P(r, \theta)/\rho U_0 R = -\left(\frac{r}{R}\right) P_1(\cos\theta) + \sum_{s=0}^\infty A_{2s} F_{2s}. \tag{1.6}$$

The precise weight sequence $\{A_{2s}\}$ is then determined by the imposition of the last boundary condition $(P = 0)$ along the free surface. The corresponding theoretical prediction for the impact-induced motion is confronted Fig. 1.4 with time-resolved PIV measurements performed on a single experiment just after impact.
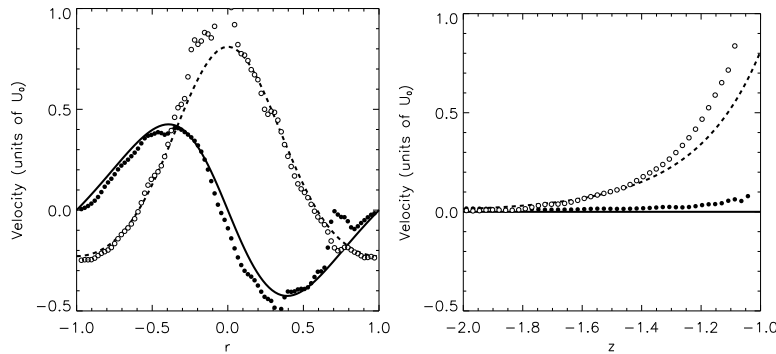
FIG. 1.4 - **Pressure impulse prediction vs PIV measurements.** Comparison between the velocity field predicted with impulse pressure theory and time-resolved PIV on a single experiment where a 3 cm diameter-tube containing a wetting liquid impacts the ground at U_0 = 6 m/s. Left: radial (plain line/filled symbols) and axial (dashed/open) components of velocity taken along an horizontal radius tangenting the free surface. Right: same comparison along the symmetry axis (Antkowiak *et al.*, 2007a).

Interestingly the only role of surface tension here is to prepare the initial free surface condition by shaping its geometry, but it plays no further role in the – purely inertial – jet formation. This link between jet formation and interface geometry is actually reminiscent of the so-called "hollow-charge principle". This old mining principle dating back from the XVIII$^{\text{th}}$ century states that charges detonated can concentrate their action and perforate a nearby object if the explosive has been hollowed out prior to ignition. Munroe, (1888) documented this phenomenon and demonstrated that an engraved guncotton charge detonated near an iron plate transfers its inscription onto the metal block: the portion of metal facing the hollowed-out explosive is gouged out as well upon detonation (see inset). This effect was not exploited outside the mining area until World War II where it has been militarized and industrialized with the design of shaped-charge weapons such as the US Army bazooka, the german Panzerfaust or the japanese suicide lunge mine. These weapons consisted in confining the explosive in the head by means of a metal cone, or liner. Upon explosion, the stresses developed by the deflagration made the metal flow and concentrate into a thin and rapid metal jet traveling at up to 8 km/s. This powerful jet could then pierce heavily armoured vehicles, making it possible for single infantrymen to defeat tanks (Birkhoff *et al.*, 1948). After the war, peacetime applications were developed, in particular for oil well completion (i.e. for perforating the bottom of oil wells and start production, see Poulter and Caldwell, 1957). Note that this type of shaped-charge jet has a velocity scaling with the detonation wave celerity (i.e. $O(\text{km/s})$) whereas the impact-induced jets presented above rather scale with the impact
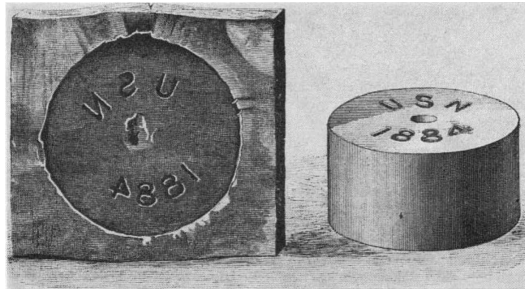
velocity, hence betraying a slightly different jet formation mechanism (viz. compressible vs incompressible). Another application, still in the explosive area, but having an even closer connection to Pokrovski's experiment, is the spontaneous ignition of nitroglycerine upon shocks. This explosive, notoriously known for its instability, should theoretically need shock pressures of $O(100\,\text{kbar})$ for compressive heating to reach the threshold needed to trigger explosive chemical reactions. However it is a fact that even moderate shocks developing pressures 10 to 20 times lower can ignite nitroglycerine. Actually nitroglycerine contains dispersed micro-bubbles which, upon impact, develop tiny jets in each of the bubbles. The point where this concentrated jet collides with the surrounding liquid walls is coined a hot spot, for pressures developed in the jet impact region can be sufficient to initiate the reaction and therefore form the seed for nitroglycerine detonation (Bowden and McOnie, 1965; Dear *et al.*, 1988).

50 μm
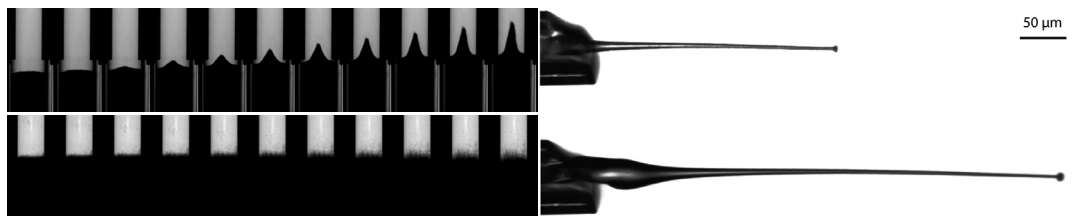
FIG. 1.5 – **Impact-driven-like jets.** Left: impact-driven jets in granular media. Top: a tube filled with sand has its interface sculpted into a meniscus-like cavity prior to impact. Just after impact, a strong granular jet, reminiscent of impact-induced liquid jets, is produced. Bottom: when the interface is left flat, no jet is produced (Antkowiak *et al.*, 2007a). Right: when a laser is focused inside a 50 μm wide capillary containing a wetting liquid, a cavitation bubble may appear. Shortly thereafter, a thin liquid jet traveling at 490 m/s is ejected from the capillary (Tagawa *et al.*, 2012).

Finally let's note that the kind of impact-driven jets presented here can develop in a broad context, largely exceeding the impact of slightly viscous liquids, or even the impact of liquids. Fig. 1.5 illustrates such a wide variety of applications with the formation of jets in a granular medium, where it is probable that the stress field built upon impact follows the same rules as the one outlined for inviscid liquid impacts, and also with the formation of supersonic thin liquid jets that could serve as a basis to design needleless syringes.

▷ **Gravity-driven jets in open and sealed cavities.** Jets can be produced from cavities even in absence of impact: the gravity relaxation of an hollow often goes together with jet formation. The essence of such gravity-driven jet formation is perhaps best illustrated with the elegant experiment designed by Élise Lorenceau during her PhD thesis (Fig. 1.6). It consists in plunging a tube closed at its upper extremity in a liquid bath. At initial time, the lid is removed and the liquid invades the tube. Interestingly, the motion of the liquid column does not stop once it is level with the free surface. Rather, the column keeps on ascending, and then falls down before ascending again. This oscillatory

FIG. 1.6 - **Model experiment for gravity-driven jet formation.** An initially sealed tube is immersed in a liquid bath thereby creating a confined cavity. Upon lid release, a liquid column starts rising and oscillating around the equilibrium level (Lorenceau *et al.*, 2002).

motion can be sustained for several tens of periods before finally being damped. This gravity-driven liquid oscillation is reminiscent of a pendulum's oscillations, where there is a ceaseless transfer between gravity potential and kinetic energies. Accordingly there is an analogous transfer of energy in these liquid column o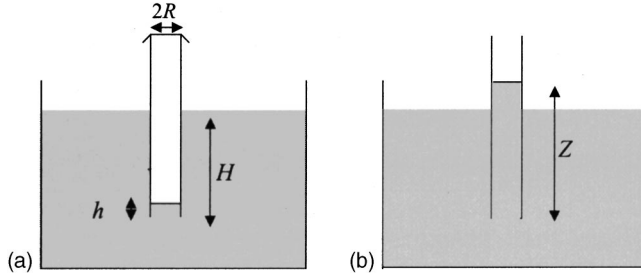scillations. To describe this motion, we start by introducing the generalized coordinates Z and $\dot{Z}$ and by noting $E_{\mathrm{kin}} = \frac{1}{2}\rho\pi R^2 Z \dot{Z}^2$ the kinetic energy of the column. The column is subject to an hydrostatic pressure force

$$F = \rho g \pi R^2 (H - Z)$$

acting on its bottom. This force derives from the potential

$$E_{\mathrm{pot}} = -\int_0^Z F \, \mathrm{d}z = \rho g \pi R^2 \left(\frac{1}{2} Z^2 - ZH \right).$$

Note that E_{pot} is also exactly the excess gravity potential energy $\int_0^Z \rho g \,(z - H)\, \mathrm{d}z$. Following Lorenceau *et al.*, (2002) we might be tempted by disregarding at first dissipative phenomena and write the constancy of the mechanical energy $E_{\mathrm{kin}} + E_{\mathrm{pot}}$, but this is too much of an approximation. Indeed, in such open systems care must be taken in examining the flowing in (or out) of matter and amending either Newton's law (Sommerfeld, 1952, chap. I, §4) or the work-energy theorem (Copeland, 1982) with appropriate source or sink terms: matter intake also means momentum/energy intake. Specifically, two improvements have to be considered. First, reckoning the energy influx, the work-energy theorem can be rewritten as:

$$E_{\mathrm{kin}} + E_{\mathrm{pot}} - \frac{1}{2}\rho\pi R^2 \int_0^Z \dot{Z}^2 \, \mathrm{d}z = \mathrm{const.} \tag{1.7}$$

Second, the force exerted by the bottom is equal to the hydrostatic load only at the very beginning. A crude approximation of the pressure modification imparted by dynamics consists in modifying F with the Bernoulli contribution $-\frac{1}{2}\rho\pi R^2 \dot{Z}^2$. Noteworthy enough, the corresponding defect work exactly compensates the energy influx of equation (1.7), so that the naive relation $E_{\mathrm{kin}} + E_{\mathrm{pot}} = \mathrm{const}$ indeed holds in this particular case. From the initial state the constant is easily seen to be 0. From this relation we can now infer that

the value of the column velocity when it erupts at $Z = H$ is simply $\sqrt{gH}$, a fact confirmed experimentally (Bergmann *et al.*, 2008; Lorenceau *et al.*, 2002). In other words the Froude number at eruption $\mathrm{Fr} = \dot{Z}_\mathrm{erupt}/\sqrt{gH}$ is systematically equal to 1 whatever the geometry of the tube. Note in particular that the tube radius R (or the aspect ratio of the initial cavity) has not any influence on the column velocity.

Does the condition $\mathrm{Fr} = 1$ also holds for jets resulting from the collapse of real hollows at a free surface? Not exactly. During the PhD thesis of Élisabeth Ghabache we investigated specifically the formation of such gravity-driven jets. The cavities were sculpted by means of a short air pulse directed towards a free surface. Driven by gravity, the transient cavity then quickly relaxed and formed a rapid liquid jet, see Fig. 1.7. Quite surprisingly, the
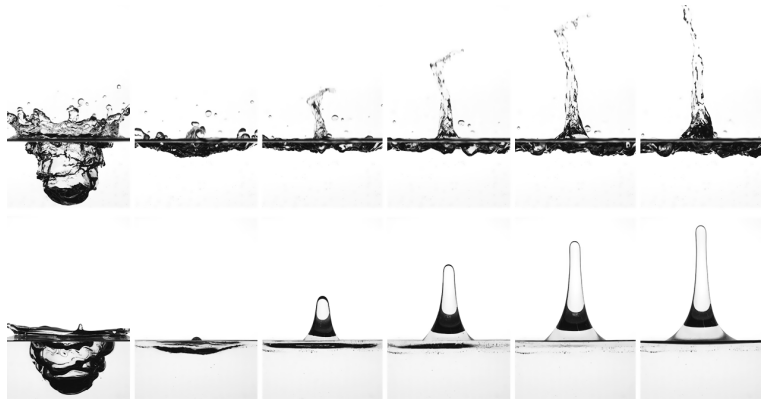
FIG. 1.7 – **Gravity-driven jets.** A cavity is formed at a free surface by gently blowing a pulse of pressurized air. As the air blow stops, the cavity relaxes and forms a liquid jet. The top time sequence corresponds to the formation of a cavity in water (μ = 1 mPa·s). The cavity has a maximum depth of H = 4.6 cm and a width L = 6.3 cm. The resulting jet has a velocity V_tip = 3.59 m·s^{-1}. The bottom sequence reports a similar experiment performed in a water-glycerol mixture with μ = 833 mPa·s. There, the cavity geometrical parameters are H = 6 cm, L = 10 cm and V_tip = 1.85 m·s^{-1} (Ghabache *et al.*, 2014b).

Froude numbers of the resulting jets are no more constant and now depend on the cavity aspect ratio H/L, as reported Fig. 1.8. Upon carefully examining the experimental data we found in Ghabache *et al.*, (2014b) the following dependence for the jet velocities V_tip to hold over the whole range of explored parameters:

$$V_\mathrm{tip} = \alpha \sqrt{gH}\frac{H}{L} - \beta \frac{\mu}{\rho L}, \tag{1.8}$$

with α and β being nondimensional constants ($\alpha = 6.59; \beta = 104$). Equivalently this relation may be written as:

$$\mathrm{Re} = \alpha \frac{H}{L}\mathrm{Ar} - \beta, \tag{1.9}$$

where Re and Ar stand respectively for the jet Reynolds number $\mathrm{Re} = \rho V_\mathrm{tip} L/\mu$ and Archimedes number $\mathrm{Ar} = \rho\sqrt{gH}L/\mu$. Relation (1.9) allows the data to collapse onto a

single line in the (Ar H/L, Re $+ \beta$) space, see Fig. 1.8. Although a full theoretical picture
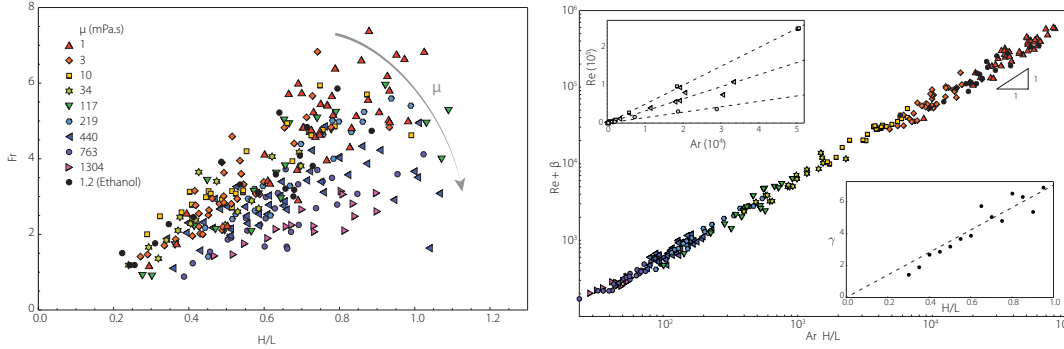
FIG. 1.8 – **Universal scaling law for gravity-driven jet velocities.** Left: the Froude numbers associated with jets produced in different liquids each exhibit a marked dependence with the cavity initial aspect ratio *H/L*. Right: all the experimental data gather onto a universal curve when represented in the (Ar *H/L*, Re $+ \beta$) space. The top left inset shows that subsets of fixed aspect ratio *H/L* exhibit a linear dependence between Re and Ar, albeit with a slope γ depending on the aspect ratio *H/L*. Note that each curve exhibits a constant *y*-intercept -β, hardly visible on the graph. Bottom right inset: the slope γ is actually linearly dependent on *H/L*: $\gamma = \alpha \, H/L$ (Ghabache *et al.*, 2014b).

of jet formation is still lacking, considerable insight into the physics of jet formation can be gained from the analysis of the scaling law (1.8). First, the nice collapse of the jet velocities onto a single master curve over almost 4 decades in Archimedes number might seem surprising when looking at the initial cavities' shapes Fig. 1.7 – which are quite irregular as a result of the method of formation. This agreement is telling, and emphasizes the fact that only the global geometry of the cavity matters for jet formation, and not the overprinted corrugations. In this regard gravity-driven jet formation is utterly different from impact-driven one, where even tiny free surface defects are transferred into the jet (see e.g. the ring jet page 5). This is because the pressure impulse field P is set at initial time and can be thought of an instantaneous photograph of the free surface, whereas the gravitational pressure field, although resulting from a much less intense acceleration, is applied continuously as the free surface deforms – and is therefore less sensitive to the precise shape of the cavity at a precise time. Second, (1.8) is informative about the dissipative phenomena at play in jet formation. As detailed in Ghabache *et al.*, (2014b), viscosity clearly alters the velocity of the jet tip, but this slowing action is limited to events preceding jet eruption (the jet essentially following a ballistic trajectory). This spatial localization of the dissipation $\mathcal{D} = \iiint 2\mu \mathbf{D} : \mathbf{D} \, \mathrm{d}V$, presumably just underneath the jet root where the velocity gradients are important, probably explains why viscosity does not appear in a prefactor but rather in an offset. Interestingly when Tagawa *et al.*, (2012) produced fast and tiny jets by focusing a laser pulse of energy E in a capillary, they observed an analogous energy loss E_{heat} that was attributed to the heating of the liquid.

Note: there is no need to invoke the generation of vorticity to explain this energy loss, for viscous potential flows do dissipate energy (e.g. as in the Rayleigh-Plesset oscillations of a bubble or in the attenuation of a gravity wave, see Boussinesq, 1877; Joseph, 2006; Lamb, 1932; Plesset and Prosperetti, 1977; Stokes, 1851)

Gravity-driven jets can also develop in the quite different context of sealed cavities. Indeed, large gas bubbles are known to evolve spontaneously into beautiful spherical cap bubbles, commonly produced by divers for example (see inset – photograph by Melissa Fiene). These bubbles, studied in great details by Davies and Taylor, (1950), are interesting soft objects that deform in response to the surrounding hydrodynamics, thereby modifying their drag coefficient and the flow around the bubble, which in turn affect the shape of the bubble etc. When equilibrium is reached, the ascending velocity of the bubble can be inferred directly from its shape : $U = \frac{2}{3}\sqrt{gR}$, with R the curvature radius of the bubble. Note that though at equilibrium the energy fed per unit time by buoyancy is exactly dissipated by viscosity, the velocity does not depend on it – which is reminiscent of aerodynamics problems and more generally of inertia-dominated flows.
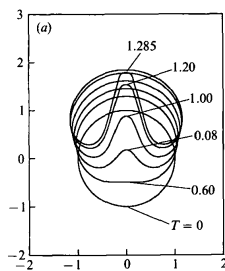
Bubbles are rarely directly produced in this spherical cap shape, but they rather evolve from a given initial condition, say spherical, to this shape. Walters and Davidson, (1963) examined this relaxation dynamics and showed that it involved the formation of a tongue of liquid. According to the initial condition and physical parameters, this tongue can even touch the bubble front and induce the reconnection into a vortex ring bubble (see e.g. Bonometti and Magnaudet, 2006; Lundgren and Mansour, 1991, and the inset extracted from their work). As as in the previous example of open cavity recoil, the relaxation dynamics of a bubble is much dependent on its initial geometry. And if the liquid is sufficiently viscous, bubbles produced from a typical bubbling setup can be initially markedly prolate. During the postdoc of Thomas Séon and within the framework of a collaboration with glass-maker Saint-Gobain, we examined the intense relaxation dynamics of such highly elongated bubbles, illustrated Fig. 1.9. There we see that just after bubble pinch-off (first image of the time sequence), an intense liquid jet develops upwards. Pinch-off events are known to be catastrophic events that can give rise to two thin and very rapid opposite jets (Worthington, 1908). In the recent years, this pinch-off has been showed to be associated with a true hydrodynamical universal singularity (Fontelos et al., 2011; Gekle and Gordillo, 2010). So is the jet observed in our experiments a mere signature of this pinch-off singularity? Probably not. Actually in our experiments we have been unable to witness the formation of the downwards jet (acknowledging that the proximity of the nozzle makes the observation difficult). Second, the jet does not appear to be universal and the tip velocity exhibits a sharp dependence with the bubble height H, reminding of the gravity-powered jets seen earlier. Figure 1.10 reports the dependence of the jet velocity V_{tip} with H. Even if there is a clear increasing trend, the scatter is disappointing, for quite different bubbles (e.g. the ones pictured in inset) can give rise to jets with the same velocity. Upon closer observation, it also appears that, for a given jet velocity, the taller bubbles also display the most curved fronts, resulting also in more pressurized bubbles. In absence of surface tension, H could roughly be seen as a measure
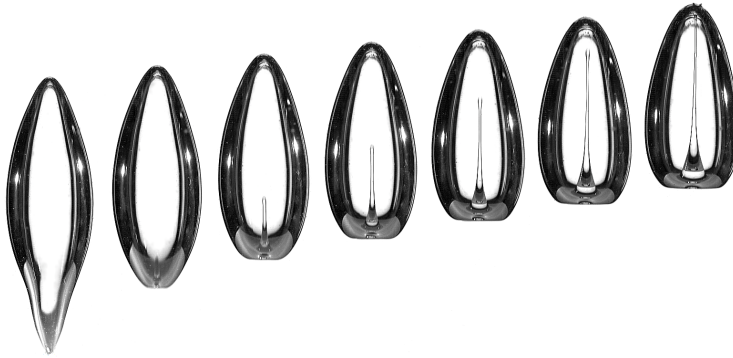
FIG. 1.9 - **A fast liquid jet develops inside a relaxing bubble.** Right after detachment in a surrounding liquid of viscosity μ = 420 mPa·s, the bubble has an initial height H = 4.22 cm. The bubble top rises at a steady velocity V_{front} = 0.67 m·s^{-1} and the jet velocity is here V_{jet} = 2.69 m·s^{-1}. The airflow rate is Q = 4.4 ℓ· min^{-1} and the nozzle diameter is R_0 = 900 μm (Séon and Antkowiak, 2012).

of the hydrostatic pressure difference $\rho g H$ between the liquid underneath the bubble and the inner bubble gas. Now reckoning the overpressure $2\gamma/R_{\text{front}}$ induced by capillarity, we see that surface tension has actually a quenching action tending to lessen the pressure difference. This correction can appropriately been taken into account by introducing a corrected height $H^\star = H - 2\gamma/\rho g R_{\text{front}}$. And indeed, when plotting the jet tip velocities as a function of $H^\star$, the scatter is significantly reduced (Fig. 1.10), therefore comforting the capillary quenching scenario specific to sealed cavities, and also to a large extent the gravity-driven nature of jet formation. With this correction we are now essentially facing a problem very close to that of jet formation from air-blown cavities. This connection is even made clearer since using the gravity-driven jet scaling law (1.9) appearing in open cavity relaxation also allows to gather all the experimental result onto a universal curve, see Fig. 1.10 (albeit with different numerical values for the parameters α and β and the nozzle radius being taken as the horizontal scale).

The robustness of this scaling relation across experiments of very different nature points to a universal mechanism linking jet formation to cavity geometry. But the extent of validity of this law is unclear at the moment, and a deeper theoretical modelling is certainly needed to unravel the physics of jet formation in the broad context of interface gravity relaxation.

1.1.2 Singular jets and the detrimental action of capillary waves

We now turn briefly to cavities having a much smaller size than previously. In this limit, cavity recoil is again violent and leads to a jet – but now for a different reason, for capillarity drives this time the relaxation process. Figure 1.11 illustrates a typical jetting event following the bursting of a small bubble. There we see that the cavity promptly reverses
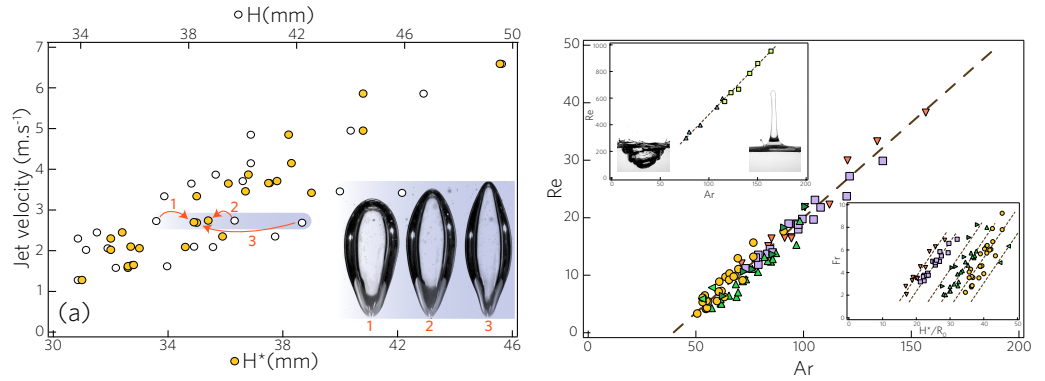
FIG. 1.10 – Left: jet tip velocities V_{tip} represented as a function of the bubble height H and of corrected height $H^\star$ for a collection of experiments. Right: all experimental data follow the scaling law (1.9) valid for open cavity relaxation jets, with α = 0.33, β = 13 and $L \equiv R_0$ the nozzle radius. (Séon and Antkowiak, 2012)

and forms a jet that further ruptures, leaving small droplets in free flight. Woodcock *et al.*, (1953) were the first to document this phenomenon and to recognize the role of these droplets propelled from bursting ocean bubbles in the formation of cloud condensation nuclei (see also Blanchard, 1967).

Actually the events preluding capillary-driven jet formation ut-terly differ from the impact- or gravity-driven jets examined ear-lier. Rather than gently everting, the cavity now shrinks and col-lapses virtually up to a point: an hydrodynamic singularity ap-pears and jet formation follows from this singularity. This route to singularity relies only on capillarity and inertia and follows a self-similar evolution where all lengths shrink as $\left(\frac{\gamma}{\rho}\right)^{\frac{1}{3}} (t^\star - t)^{\frac{2}{3}}$, with $t^\star$ being the singularity time (Keller and Miksis, 1983). This self-similar evolution is universal and generic, i.e. it can be detected in quite different settings, such as overdriven Faraday waves (see inset with raw and rescaled cavity profiles in self-

similar space by Zeff *et al.*, 2000) or collapsing bubbles (Duchemin *et al.*, 2002). During the PhD thesis of Elisabeth Ghabache, we paid a close attention to jets sparking from small bursting bubbles, and found an unexpected role played by viscosity in their dynam-ics. Actually **bubbles made in more viscous liquids squirt thinner and faster jets**, as demonstrated Fig. 1.12. Viscosity is known to promote instabilities when a large kinetic energy reservoir is present (e.g. Tollmien-Schlichting waves) but there is no such reservoir here, making this result all the more startling. What is the mechanism for jet enhance-ment then? The answer is provided Fig. 1.12, where we see that the smallest cavity width reached is viscosity dependent. Actually, the cavity may be thought as a combination of a crunching cavity and of capillary waves riding on it. If the damping action of viscosity
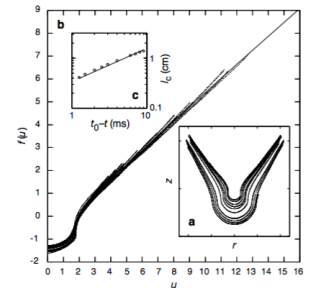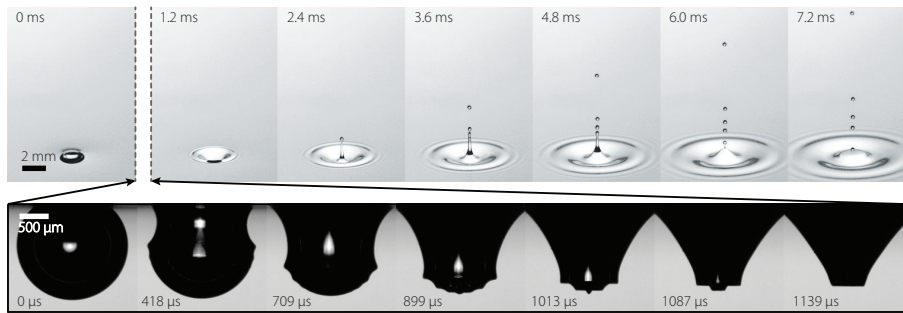
FIG. 1.11 - **Jet forming from a bursting bubble.** Top: bubble bursting event, as seen from above the free surface. Bottom: cavity dynamics as seen from under the free surface, exhibiting the collapse of the cavity and ripples riding onto its surface. This sequence takes place between the two first images of the top one (Ghabache *et al.*, 2014a).

is not sufficient, these waves will interfere destructively with the self-similar collapse and make it stop at a typical size L_{min}. When viscosity is larger, these waves are damped and the self-similar collapse proceeds up to its limit (presumably the visco-capillary length). This interplay between self-similarity and (detrimental) capillary waves is intriguing and suggests that the jet properties (e.g. tip velocity) critically depend on the cavity geometry (Ghabache *et al.*, 2014a) – properties that could be finely controlled by imprinting a desired pattern on the bubble surface by e.g. acoustic means.

1.2 Feeding flow and flow focusing

So far, we have observed experimentally a strong link between the jet velocity and the initial cavity geometry for a variety of situations. But there is still large dimmed areas in the fluid dynamics of jet formation; Could we describe and fully grasp the chronology of the hydrodynamical events presiding jet formation, development up to fragmentation? One of the most important missing link in this story so far is the flow pattern feeding the jet, for it governs the jet geometry and hydrodynamics, and also because most of the dissipation presumably happen at the jet root level. Obviously unsteadiness and nonlinear free surface deformation are strong impediments to this feat, and disregarding those by e.g. just transporting vertically (or radially) the free surface from the knowledge of the velocity at initial time would be a bad idea, leading to absurd results such as finite time geometrical singularities (see e.g. Dear *et al.*, 1988). Rather, we might be tempted to use the approach of Davies and Taylor, (1950) or Bisighini *et al.*, (2010) to determine the flow beneath the surface, where the authors consider a simple elementary harmonic potential interacting with either a steady surface or a simple and reasonable approximation of it. The problem in our situation is that the free surface is far from trivial and there is just no simple ansatz for its description. Layzer, (1955) was facing in the fifties a similar situation in an astrophysical context, and proposed to consider the free surface as an unknown of
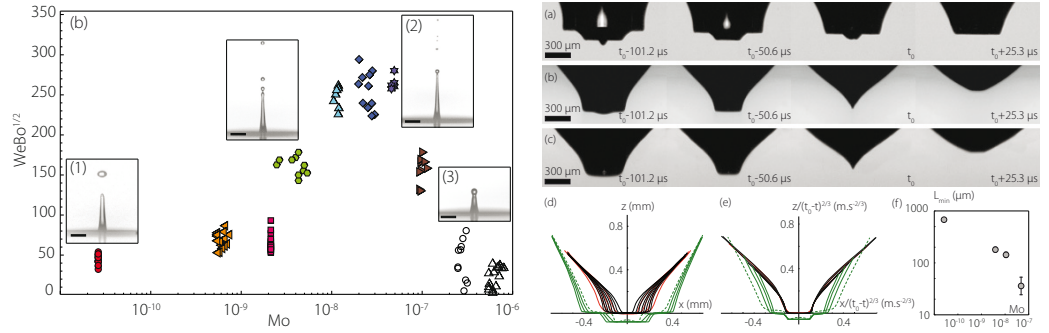
FIG. 1.12 – **More viscous but faster.** Left: bubble jet velocities measured as We $\sqrt{\text{Bo}}$ (note the presence of $\sqrt{\text{Bo}}$ to absorb a bubble size dependence effect) versus the nondimensional viscosity measured here with the Morton number Mo $= g\mu^4/\rho\gamma^3$. A velocity peak clearly appears for a specific value of Mo. Right: cavity dynamics corresponding to the jets labeled 1, 2 and 3 on the leftmost graph, and their rescaled contours in the self-similar space. For the less viscous case, capillary waves riding on the cavity prevents the collapse to proceed up to its limit. Bottom and rightmost: the smallest width of the cavity L_{min} decreases with the viscosity (Ghabache *et al.*, 2014a).

the problem as well. Transposing his approach to Pokrovski's problem, we approximate the velocity potential at any time with:

$$\phi(r, z, t) = Uz + F(t)e^z J_0(r). \tag{1.10}$$

Figure 1.13 displays the flow pattern associated with this potential and we readily see, from mere kinematical arguments, that the feeding flow is concentrated just beneath the free surface. Upon injecting this ansatz into Bernoulli equation, it can unfortunately be seen that this dynamical equation cannot be satisfied over the entire surface. Nonetheless it is possible to verify this equation in a small neighbourhood of the apex. Lengthy but straightforward calculations allow to recast this condition into a single nonlinear differential equation for $F(t)$ which can be solved numerically, and to deduce the flow hydrodynamics and free surface evolution. Following our example of impulsive jet formation, we represent Fig. 1.13 the free surface eversion and jet formation as described by this small model. Interestingly, we here remark that key features such as flow focusing are already captured within this simple approximation.

1.3 Jet development: hints of universality

The trouble with Layzer's theory (also coined single-mode approximation in the Rayleigh-Taylor community) resides in its poor ability to capture fine features – which would require higher-order modes. Unfortunately, the jet shape itself falls into this category, and it seems quite tedious a task to include a collection of higher harmonics in this approximation.
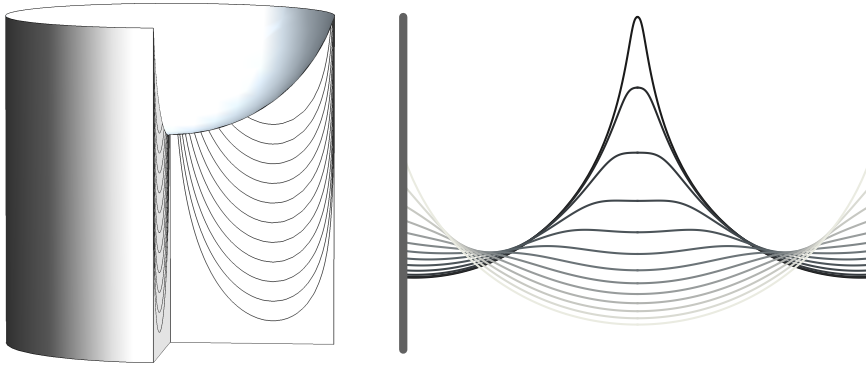
FIG. 1.13 - **Layzer's theory for Pokrovski's jet.** Left: cut-out view of the initial geometry (here a fluid bounded with a spherical cap meniscus with a wetting angle of 18°), revealing the streamlines underneath the free surface, in the tube reference frame. Note that this flow pattern is steady through time. Right: corresponding evolution of the free surface just after impact within the framework of Layzer's theory (or single-mode approximation).

Yet experimentally several strikingly simple facts about transient jets emerge from direct observation. First, the structure of the velocity field within the jet seems to be attracted by the simple expansion wave profile z/t. This behaviour was already noted by DiPersio *et al.*, (1960) in the context of shaped charge jets. DiPersio *et al.* analysed with the help of triple-flash radiographs the velocity of jets fragments (see inset) and found a close-to-perfect linear velocity profile within the shaped-charge jet (see Fig. 1.14). During the PhD thesis of Élisabeth Ghabache we also investigated by means of PIV the velocity field within transient jets for a variety of setups, each characterised with a different injection law for the jet, and found that the velocity profiles were invariably attracted by the linear profile. To understand why this particularly velocity profile is so stable, we may first reckon that the evolution of the velocity within the jet is pressureless and does not rely on capillarity in the inertial limit:

$$\frac{\partial u}{\partial t} + u \frac{\partial u}{\partial z} = 0. \tag{1.11}$$

Looking for monomial solutions $z^\alpha t^\beta$ we readily see that the equation selects the single exponents pair $(\alpha, \beta) = (1, -1)$ which is precisely the relaxation wave profile z/t. Now posing $\eta = z/t$ as the self-similar variable, we look for the behaviour of solutions $u(\eta, \tau)$ close to the self-similar profile (Eggers and Fontelos, 2009). Note that we have explicitly kept the time variable, now expressed via its logarithm $\tau = \ln t$, to estimate departures or convergence to
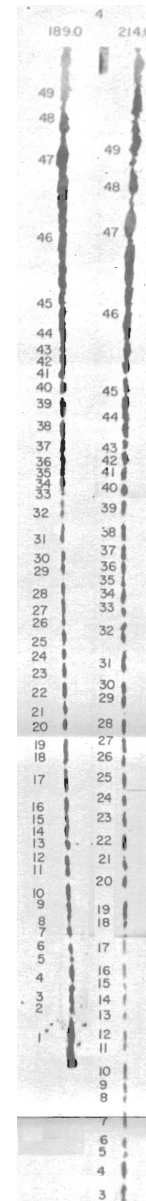
the self-similar profile. Bürgers equation (1.11) is then recast into:

$$\frac{\partial u}{\partial \tau} = (\eta - u)\frac{\partial u}{\partial \eta}. \tag{1.12}$$

Solutions close to the self-similar profile may be written as $u(\eta, \tau) = \eta + \epsilon u_1(\eta, \tau)$. Linearising the equation around the self-similar state we end up with:

$$\frac{\partial u_1}{\partial \tau} = -u_1, \tag{1.13}$$

which admits an exponentially decaying solution in the logarithmic variable τ. We conclude that the relaxation wave profile is a stable fixed point of equation, and is therefore an inertial attractor for the jet dynamics (Ghabache *et al.*, 2014b).
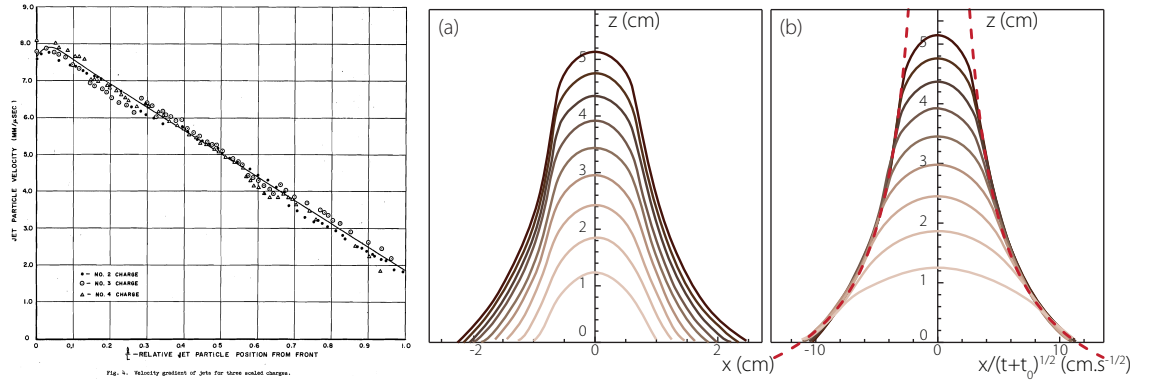
FIG. 1.14 - **Transient jet geometry and hydrodynamics.** Left: transient jets, such as shaped-charge jets, naturally evolve so as to exhibit a linear velocity profile (DiPersio *et al.*, 1960). Right: geometry of transient jets. (a) Experimental jet profiles obtained in gravity relaxation experiments (here originating from a cavity such that H = 4.9 cm, L = 9.6 cm) in a liquid of viscosity μ = 763 mPa·s. The velocity of the jet is V_{tip} = 1.41 m·s⁻¹. The interval between two profiles is 5 ms and it appears that the jet widens linearly with time. (b) Same jet profiles after rescaling of the x coordinate by $\sqrt{t+t_0}$. The dashed line red curve follows the equation $z = C\,x^{-1} - z_0$

Having examined the structure of the velocity field we now turn to the shape of inertial jets. Mass conservation reads, in the same 1D approximation as earlier:

$$\frac{\partial r}{\partial t} + u\frac{\partial r}{\partial z} = -\frac{1}{2}r\frac{\partial u}{\partial z}, \tag{1.14}$$

noting $r(z,t)$ the local jet radius and $u(z,t)$ the local velocity in a fluid slice.
As previously we may enquire about jet shape similarity, by looking for solutions $r(z,t)$ of the mass conservation equation (1.14) in the form of monomials $z^a t^b$. A one-parameter

family of solutions such that $a = -(2b + 1)/2$ is readily obtained. It is impossible to go further on purely heuristic grounds, but experimentally it appears that transient jets appear to widen linearly versus time, at least in all our gravity relaxation-induced jets. This observation allows us to infer that the particular exponent pair $(a, b) = (-1, \frac{1}{2})$ is selected:

$$r_{\mathrm{jet}}(z, t) = C \frac{\sqrt{t + t_0}}{z + z_0}, \tag{1.15}$$

where C is a constant prefactor.

Figure 1.14 reports typical profiles observed in gravity relaxation experiments. These jets are representative of transient jets formed in a variety of configurations. Representing the same profiles now as a function of the self-similar variable $r/\sqrt{t + t_0}$ reveals that the jet actually develops in a self-similar sheath (see Fig. 1.14). It is noteworthy that the jet flanks adopt a perfect hyperbolic shape, consistent with the purely inertial prediction (1.15). The experimental observations reported Fig. 1.14 therefore demonstrate not only the shape similarity of the evolving jet (square-root of time spreading of the radius and hyperbolic shape), but also the validity of the assumptions made for obtaining (1.11) and (1.15). Interestingly Stuhlman, (1932), performing an a posteriori analysis of prior experimental photographs obtained by Worthington, also evidenced an hyperbolic shape for jets following a drop impact on a liquid surface.

This example emphasizes the fact that an accurate description of jets does not necessarily rely on deploying an intricate strategy with high-order harmonics. Conversely, some links between the different steps of the jet chronology still need to be elucidated, such as the shape selection just seen. To establish, with first principles, the chain of events running from jet formation up to fragmentation into droplets is more than ever an direct prospect of the here presented study and will be the subject of future investigations.

2 | Drop Impact

The impact of a droplet, whether on a rigid ground or on a liquid surface, has fascinated scientists for more than a century. This is partly due to the instant complexity arising from the collision : a single drop with a single radius R and velocity U is suddenly deformed, torn apart up to rupture into myriads of fragments of various sizes and velocities. Impact foremost is a source of heterogeneity. Second, these phenomena are fast. The typical duration of an impact R/U or the characteristic oscillation period of a droplet, i.e. the capillary timescale $\sqrt{\rho R^3/\gamma}$, are both of the order of the millisecond for millimetric droplets, certainly explaining why we only catch a glimpse of capillary events, however commonplace they are. If complexity and swiftness drives the scientist curiosity, they also restrain him from a full understanding – if a complex experiment is difficult to apprehend, a complex experiment you cannot see is probably even more difficult. This is presumably why the first scientific investigations on drop impact coincide with the advent of photography, see the pioneering studies of Worthington, (1908). Half a century later, the emergence of fast cameras in a military context (Engel, 1955) (and then of course with their popularization in the late 90s) allowed for a deeper analysis of the rapid sequence of events characterizing drop impact : spreading or splashing (Stow and Hadfield, 1981), interface tearing (Villermaux and Bossa, 2011) and ultimate fragmentation (Stow and Stainer, 1977). We do not intend here to review all the different forms of drop impact (of e.g. newtonian, viscoplastic liquids onto e.g. liquid, dry, yielding, corrugated substrates) nor the consequences of drop impact for soil erosion, plant disease dissemination, aerospace industry etc. and refer the interested reader to relevant review papers (Josserand and Thoroddsen, 2016; Rein, 1993). Let's rather mention that if a large number of studies have investigated the many facets of drop impact, the literature on the early stages of impact is however scarce in comparison. Probably one of the first depiction of the very first instants of drop impact dates back to Engel, (1955) precisely. Interestingly, she noted the unvarying shape of the drop apex during the earliest moments of impact. To explain this observation, Engel put forward at the time the possible roles of inertia, viscosity or surface tension. This behaviour was later confirmed with detailed experimental data depicting the instants following impact in the work of Rioboo *et al.*, (2002), who evidenced a "kinematic phase" where the drop merely resembles a truncated sphere and spreads as the square-root of time. This phase precedes the apparition of the liquid lamella.

   A common feature of these experimental observations is the fact that they present shapes and not forces, so to speak. A force measurement represents a real technical chal-
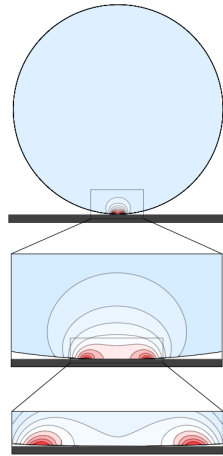
FIG. 2.1 - **Pressure field in an impacting drop.** Close-ups of increasing magnitude on the pressure field developing inside an impacting drop in the inertial limit. The pressure field is extracted from Navier-Stokes *Gerris* computations of a drop impacting a solid surface at early times (note that the surrounding gas dynamics is computed as well, but not represented here). Noticeably the motion is essentially pressureless (and therefore corresponds to a free fall) except in a concentrated region in the contact zone. The successive close-ups on pressure field structure in the contact region reveal a pressure peak near the contact line (the physical parameters are here Re = 5000, We = 250, $t\,U/R = 4\times10^{-4}$. The total size of the numerical axisymmetric domain is $2R\times 2R$, and the adaptive mesh has locally a mesh density corresponding to 32768×32768 grid points; Philippi *et al.*, 2016).

lenge and, without such a direct information, it proves quite difficult to extract the pressure field from the knowledge of the interface geometry only. On the other hand, numerical simulations would offer the possibility to compute all these fields at once, but typically the large spatial scale separation and the density/viscosity ratios strongly hinder the practical realization of these simulations. Fortunately, we have benefited in the laboratory from the *Gerris* code (Navier-Stokes solver, volume of fluid, adaptive mesh), developed by Stéphane Popinet, that incorporates the latest state-of-the-art numerical techniques allowing to overcome these difficulties (Popinet, 2003; 2009). During the PhD thesis of Julien Philippi, we made an extensive use of such numerical simulations to unravel the short-time dynamics of drop impact. Figure 2.1 represents a typical illustration of these simulations. There, the numerically computed pressure field within an impacting drop is represented shortly after impact (details to follow). It is readily seen that the structure of the pressure field is extremely concentrated near the contact zone, as in Hertz' classic elastic contact problem. Conversely the outer region is essentially pressureless. This strong inhomogeneity in the pressure distribution therefore sheds light over Engel's observation and explains why, in the absence of any pressure hindrance, the upper part of the drop freely falls even after impact while remaining undeformed.

This sets the scene for this chapter, which central motivation is to revisit the prob-

lem of a single spherical drop impacting a solid surface at early times. More precisely, the goal will be to unfold the peculiar structure of the pressure field perceived Fig. 2.1. By confronting and cross-testing systematically theoretical predictions with detailed and accurate numerical simulations, the whole hydrodynamics and geometry of an impacting droplet will prove to be self-similar, and furthermore to have connections with three classic problems of fluid mechanics, as explained next.

2.1 Short-time self-similarity, and three analogies

The pressure field structure illustrated Fig. 2.1 is actually reminiscent of the pressure fields developed during the water entry of a solid object. Furthermore, as already noted by Cointe, (1989), drop impact may be viewed as water entry's opposite, for here a liquid object impacts a rigid flat surface at a given velocity (see Fig. 2.2). This remark is key and will feed our line of thought for the remaining of this part, as well as drive us to use the analytical techniques developed since the thirties to describe with great precision the flow generated with the impact of an object, and proven to be in close agreement with experimental data. This analogy with the water entry problem will actually spring two further analogies allowing to understand the main flow features of impact and also the structure of the boundary layer. But let's start by examining further the connection between drop impact and water entry.
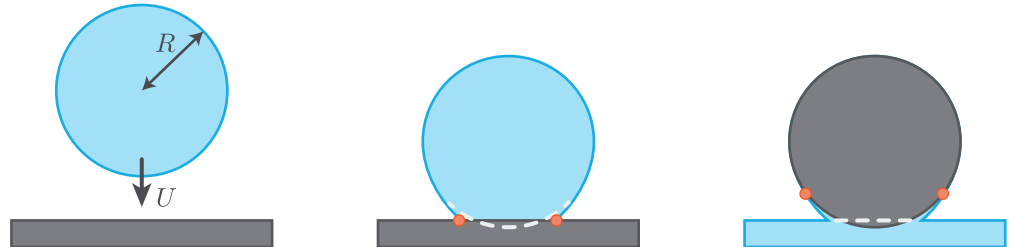
FIG. 2.2 – **Drop impact as the dual problem of water entry.** Sketch of the drop before contact (left), and shortly after impact (middle). The shape the drop would assume in absence of wall is outlined with a dashed line, and the contact line position is marked with red dots. This problem may be viewed as the dual of the classic water entry of a solid object (right).

2.1.1 Wagner's water entry and Lamb's flow around a disk

The modern understanding of the liquid motion and forces generated by an impacting object in water originates in the pioneering work of Wagner in the early thirties (Wagner, 1932). The primary motivation of Wagner was to provide a detailed characterization of the impulsive forces generated with impact – already known to be of sufficient amplitude to induce bouncing (ricochet), and even possibly structural failure of alighting seaplanes or slammed ships (Nethercote *et al.*, 1986). The foremost issue in this problem evidently

stems from its highly unsteady and nonlinear nature. The central idea of Wagner was to model the flow induced by the impact of a float or a keel by the one induced by a flat "plate", propelling the fluid particles downwards at the float or keel velocity, and having an extent growing with time as the waterline length. The corresponding flow (*"gleiche Tragflügelbewegung"* – equivalent aerofoil motion) is typically found to wind around the plate and therefore to promote jetting or splashing. The knowledge of this flow field then allows to determine the motion of the free surface, and finally provides the needed condition in the determination of the wet length $d(t)$. To summarize, Wagner's idea therefore consists in three steps sequence:

1. Forget about the precise object shape, and seek for the flow induced by a growing plate of extent $d(t)$ (corresponding to the waterline length, unknown for the moment) that would propel the fluid downwards at velocity U. The free surface motion is not considered here and the fluids fills a half-plane.

2. Deduce from the knowledge of the velocity field the displacement of the free surface corresponding to any $d(t)$.

3. Finally, by remembering the object shape and writing the condition that a free surface fluid particule initially at the position $d(\tau)$ touches the object exactly at $t = \tau$, the law $d(t)$ is uncovered thereby solving for the last unknown in the problem.

This last condition is now referred to as Wagner's condition in the literature. This resolution scheme calls for a few remarks. First, it is sequential, or in other words, this scheme provides a way to uncouple an otherwise fully intricated problem. Second, it might seem surprising at first that the flow established at step one does not depend on history (of the flow itself, and of $d(t)$). Such dependence on history would indeed appear if vorticity or deformation of the free surface were taken into account. But there is more. Even in absence of these effects, potential flows may exhibit transients (i.e. history effects) if the motion is set with forces (boundary stresses or body forces). Conversely, in a rigid-loading problem where velocity is imposed on the boundaries there is no such dependence. This is because in the first case Newton's laws of motion have to be considered: the liquid mass is accelerated with forces and this takes time. In the second case there is no need to have recourse to the laws of motion because the knowledge of the boundary velocity and of the incompressible potential character of fluid motion sets everything; the first step of Wagner's idea is therefore definitely kinematical. Finally, let's note that the geometry and equations used in Wagner' scheme of resolution can be fully justified with asymptotic arguments (see e.g. Howison *et al.*, 1991; Oliver, 2002).

Now if we get back to the drop impact problem, we already noted the similitudes between the pressure field developed in water entry problems and the one observed in accurate simulations of drop impact. But these similitudes also appear in other flow features. More particularly, a winding motion around the contact line can clearly be seen from the simulations (see the flow streamlines in the
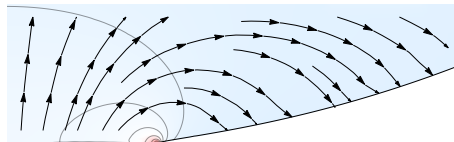
falling drop reference frame in inset). Such a motion is again a trademark of water entry problem where the liquid winds around the edge of the growing plate of extent $d(t)$. This means that the free surface of the drop on the verge of touching the substrate falls faster than the drop itself, which is rather unexpected. We also remark that this particular bypass of the contact line also implies that the wet area does not increase as a result of a sweeping, but rather of a tank-treading motion near the contact line. In other words, the kinematics of horizontal extension for the wet radius is controlled by the vertical motion of the free surface. All these observations advocate for the use of a water entry-analogue
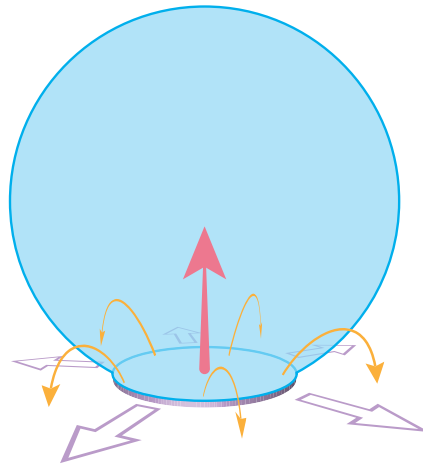
FIG. 2.3 - **Lamb disk analogy.** In the reference frame of the falling drop, the flow induced by impact may be seen as the one induced by a flat rising disk. The winding motion is here represented with orange arrows, and the radial expansion of the disk with the wet area is indicated with purple arrows. The motion of the disk itself is given by the red arrow.

description of impact, but also for picturing drop impact another way. Indeed we now put forward a 'Lamb analogy' mirroring the flow within the impacting drop with the one induced by a flat expanding disk in normal incidence, see Fig. 2.3 – the extent of the disk being set by the wet area. Following this vision of drop impact as a dual version of the water entry problem, we adopt from now on the corresponding formalism to describe the fluid mechanics of impact.

2.1.2   Liquid impact equations and self-similar solutions

The motion inside an impacting drop may be described, if we neglect for now the development of viscous rotational boundary layers, with the help of the harmonic potential $\bar{\phi}(\bar{r}, \bar{z}, \bar{t})$ such that the velocity field $\bar{\boldsymbol{u}}(\bar{r}, \bar{z}, \bar{t}) = \bar{\nabla}\bar{\phi}(\bar{r}, \bar{z}, \bar{t})$, where bars indicate a proper nondimensionalization with the liquid density ρ, the free flight velocity U and the drop radius R. Note also that axisymmetry is implicitly supposed here. The problem is therefore governed by the harmonicity of $\bar{\phi}$, Bernoulli's equation over the free surface and

appropriate boundary conditions which read:

$$\frac{1}{\bar{r}}\frac{\partial}{\partial \bar{r}}\left(\bar{r}\frac{\partial \bar{\phi}}{\partial \bar{r}}\right) + \frac{\partial^2 \bar{\phi}}{\partial \bar{z}^2} = 0 \quad \text{in the liquid,} \tag{2.1a}$$

$$\frac{\partial \bar{\phi}}{\partial \bar{t}} + \frac{1}{2}|\bar{\nabla}\bar{\phi}|^2 + \bar{p} = \frac{1}{2} \quad \text{in the liquid,} \tag{2.1b}$$

$$\frac{\partial \bar{\phi}}{\partial \bar{z}}(\bar{r}, \bar{z} = 0, \bar{t}) = 0 \quad \text{over the wet area } \bar{r} < \bar{d}(\bar{t}), \tag{2.1c}$$

$$\bar{p} = 0 \quad \text{on the free surface,} \tag{2.1d}$$

$$\frac{\mathrm{d}\bar{\mathcal{S}}}{\mathrm{d}\bar{t}} = 0 \quad \text{on the free surface.} \tag{2.1e}$$

Here $\bar{\mathcal{S}}(\bar{r}, \bar{z}, \bar{t})$ is a function vanishing on the free surface. We could also add an extra-equation describing the far-field behaviour of the solution, and which will prove useful later:

$$\bar{\phi} \to -\bar{z} \quad \text{far from the contact region.} \tag{2.1f}$$

As posited, the problem entirely depends on the wet area extent $\bar{d}(\bar{t})$, whose dynamics has still to be determined.
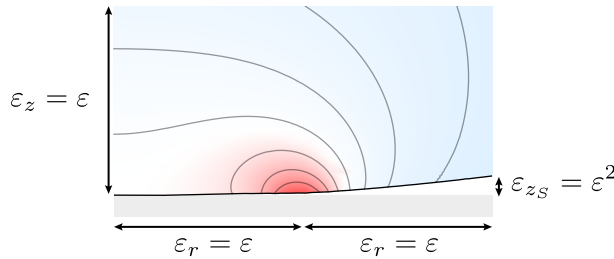
FIG. 2.4 - **Scalings in the contact zone.** At the earliest times only a very small portion (of order ε) of the drop touches the wall. The fluid sets into motion with impact is in a region of extent ε in every direction. The air wedge confined between the wall and the drop presents an angle of order ε as well.

▷ **Leading-order description.** Interested in the early-time behaviour of the impact-induced flow, we set out by examining time-dependent solutions of system (2.1a–2.1e) in the vicinity of the contact zone. To this end, we introduce ε as a measure of the wet region: $d(t)/R = O(\varepsilon)$ (see Fig. 2.4). This ε is the fundamental small parameter of our problem. As typical in two-phase phenomena, the lengthscales for the dynamical fields

$$\bar{r} = \varepsilon\, r,$$

$$\bar{z} = \varepsilon\, z,$$

$$\bar{t} = \varepsilon^2\, t,$$

$$\bar{p} = \varepsilon^{-1}\, p,$$

$$\bar{\phi} = -\bar{z} + \varepsilon\, \phi,$$

$$(\bar{u}, \bar{v}) = (u, v).$$

TABLE 2.1 - Asymptotic scales for the drop impact problem.

and for the geometry of the free surface differ in this problem. Starting by considering the space variables $\bar{r}$ and $\bar{z}$ on which depend the dynamical fields (such as the velocity potential $\bar{\phi}$ or the pressure $\bar{p}$), we introduce the following rescaling: $\bar{r} = \varepsilon_r r$ and $\bar{z} = \varepsilon_z z$, where r and z are $O(1)$ quantities and ε_r and ε_z are gauge functions. From the structure of Laplace operator, we expect the dynamical fields to display identical length scales in each direction, so that $\varepsilon_r = \varepsilon_z = \varepsilon$.

Insights into the relevant lengthscales for the description of the free surface geometry can be gained by decomposing the position of the surface into that of a translating sphere $\bar{z}_S(\bar{r}, \bar{t})$ plus a surface disturbance $\bar{h}(\bar{r}, \bar{t})$ (see Fig. 2.2b). Assuming the drop falls with constant velocity, the shape of the unperturbed translating sphere obeys $\bar{r}^2 + (\bar{z}_S - (1 - \bar{t}))^2 = 1$. Sufficiently close to the contact area, we introduce gauge functions for the vertical position of the moving sphere $\bar{z}_S$ and the time $\bar{t}$: $\bar{z}_S = \varepsilon_{z_S} z_S$ and $\bar{t} = \varepsilon_t t$. The equation for the sphere surface can be approximated by $\varepsilon_{z_S} z_S = \frac{1}{2}\varepsilon^2 r^2 - \varepsilon_t t$. As previously the determination of these scaling functions is obtained by dominant balance arguments: $\varepsilon_{z_S} = \varepsilon_t = \varepsilon^2$. We remark that as in the original study of Wagner, a scale separation between $\bar{z}_S$ and $\bar{z}$ exists (small deadrise angle hypothesis, see e.g. Oliver, 2002). This scale separation arises because the drop typical radius of curvature $O(1)$ is very large in front of the other lengthscales of the problem, see Fig. 2.4. Similarly working out the other equations of the problem, we naturally introduce a translation of the velocity potential so as to work with $\bar{\phi} + \bar{z}$ and find all the asymptotic scales, which are summarized in table 2.1. Plugging these scales into the governing equations allows to rewrite them in a simpler, leading-order setting. For example, inserting these different scaled variables into Bernoulli's equation, we obtain:

$$\frac{1}{\varepsilon}p + \frac{1}{\varepsilon}\frac{\partial\phi}{\partial t} + \frac{1}{2}\left[\left(\frac{\partial\phi}{\partial r}\right)^2 + \left(-1 + \frac{\partial\phi}{\partial z}\right)^2\right] = \frac{1}{2} \quad \text{in the liquid.} \tag{2.2}$$

The scale of the pressure $1/\varepsilon$ is here seen to be as large as the contact zone is small – as expected in an impact problem. At leading order, Bernoulli's equation is therefore reduced

to:

$$p = -\frac{\partial \phi}{\partial t} \quad \text{in the liquid.} \tag{2.3}$$

This is in stark contrast with the classic steady version of Bernoulli where the pressure is as small as the kinetic energy is large $p + \frac{1}{2}\rho U^2 = \text{cte}$. Here, unsteadiness drives the pressure, and this results in counterintuitive effects, such as the peak pressure near the contact line.

Finally, the geometry of the problem as well can be simplified at leading order; as classic in water wave theory, we exploit the shallowness of the gap between the free surface and the plane to transfer the boundary condition at the free surface onto the plane (see e.g. Van Dyke, 1975, §3.8).

Summarizing, this near-field model problem takes the following form:

$$\frac{1}{r}\frac{\partial}{\partial r}\left(r\frac{\partial \phi}{\partial r}\right) + \frac{\partial^2 \phi}{\partial z^2} = 0 \quad \text{in the liquid,} \tag{2.4}$$

$$p = -\frac{\partial \phi}{\partial t} \quad \text{in the liquid,} \tag{2.5}$$

the locus $d(t)$ of the contact line is determined with the Wagner condition:

$$h(r,t) = \frac{1}{2}r^2 - t \quad \text{for} \quad r = d(t), \tag{2.6}$$

so that the boundary conditions at $z = 0$ read:

$$\phi = 0 \quad \text{for} \quad r > d(t), \tag{2.7}$$

$$\frac{\partial h}{\partial t} = -\frac{\partial \phi}{\partial z} \quad \text{for} \quad r > d(t), \tag{2.8}$$

$$\frac{\partial \phi}{\partial z} = 1 \quad \text{for} \quad r < d(t), \tag{2.9}$$

and the far-field behaviour is given by:

$$\phi \to 0 \quad \text{as} \quad r, z \to \infty \tag{2.10}$$

$$h \to 0 \quad \text{as} \quad r \to \infty. \tag{2.11}$$

Finally the corresponding model geometry is sketched Fig. 2.5. We remark that the previous set of equations resembles to that of the classic water entry problem, and can be solved using the methodology described in e.g. Oliver, (2002), though we will now present an alternate derivation based on self-similar solutions.

▷ **Self-similarity.** To reveal the self-similar nature of our problem, we classically look in the following for scale invariance (Darrozès and François, 1982). We start by expressing the fact that any variable q in (r, z, t, ϕ, h, d, p) can be rewritten as $q = \lambda_q Q$, where Q is a rescaled variable and λ_q a numerical stretching coefficient embodying the change of scale. Inserting these variables into the governing equations, it is straightforward to see
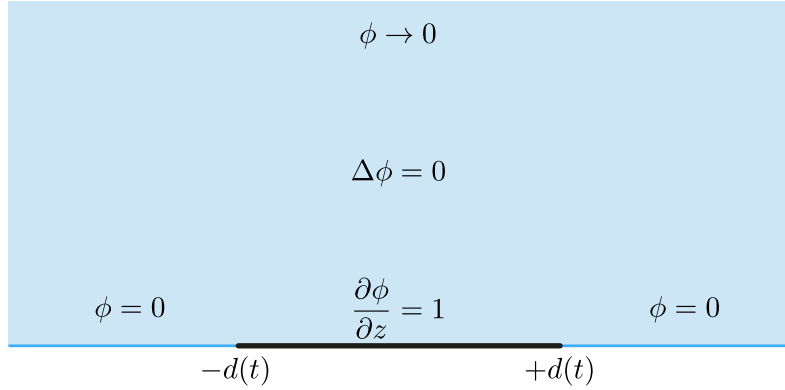
FIG. 2.5 - **Leading order outer problem** for times of order ε^2.

that invariance of Laplace equation through this stretching requires $\lambda_r = \lambda_z$. Similarly, expressing the invariance of Wagner condition yields $\lambda_h = \lambda_t$, $\lambda_r = \sqrt{\lambda_t}$ and $\lambda_d = \sqrt{\lambda_t}$. The same operation performed on the additional boundary conditions finally imposes $\lambda_\phi = \sqrt{\lambda_t}$ and $\lambda_p = 1/\sqrt{\lambda_t}$. Note that λ_t remains here as the sole stretching parameter. The pressure field can be written as an implicit function of time and space as follows: $\mathcal{F}(p, r, z, t) = 0$. Upon using the previous scale invariance arguments, this relation may be rewritten as $\mathcal{F}(P/\sqrt{\lambda_t}, \sqrt{\lambda_t}R, \sqrt{\lambda_t}Z, \lambda_t T) = 0$. A simple algebraic manipulation allows to remove the λ_t dependence for all but one variables, so that finally $\mathcal{G}(\sqrt{T}\,P, R/\sqrt{T}, Z/\sqrt{T}, \lambda_t T) = 0$, for any λ_t. Remarking that for a given T, this function has to cancel whatever the choice of the scale λ_t, it readily appears that the last variable is superfluous. In other words, a relation linking $\sqrt{T}P$ to $R/\sqrt{T}$ and $Z/\sqrt{T}$ only must exist.

The pressure field may therefore be rewritten explicitly as:

$$p = \frac{1}{\sqrt{t}}\mathcal{P}\left(\frac{r}{\sqrt{t}}, \frac{z}{\sqrt{t}}\right). \tag{2.12}$$

With a similar reasoning, and upon introducing the self-similar variables $\xi = r/\sqrt{t}$ and $\eta = z/\sqrt{t}$, we readily obtain :

$$\phi(r, z, t) = \sqrt{t}\,\Phi(\xi, \eta), \quad h(r, t) = t\,\mathcal{H}(\xi) \quad \text{and} \quad d(x, t) = \sqrt{t}\,\delta, \tag{2.13}$$

where Φ and $\mathcal{H}$ are unknown functions of the self-similar variables and δ a constant representing the (fixed) position of the contact line in self-similar space.

Rewriting again the governing equations but now in the self-similar space, we get:

$$\frac{1}{\xi}\frac{\partial}{\partial \xi}\left(\xi\frac{\partial \Phi}{\partial \xi}\right) + \frac{\partial^2 \Phi}{\partial \eta^2} = 0 \quad \text{in the liquid,} \tag{2.14}$$

$$\mathcal{P}(\xi, \eta) = \frac{1}{2}\left(-\Phi(\xi, \eta) + \xi\frac{\partial \Phi}{\partial \xi} + \eta\frac{\partial \Phi}{\partial \eta}\right) \quad \text{in the liquid,} \tag{2.15}$$

the boundary conditions at $\eta = 0$ take the following form:

$$\mathcal{H} - \frac{1}{2}\xi\frac{\partial\mathcal{H}}{\partial\xi} = -\frac{\partial\Phi}{\partial\eta} \quad \text{for} \quad \xi > \delta, \tag{2.16}$$

$$\frac{\partial\Phi}{\partial\eta} = 1 \quad \text{for} \quad \xi < \delta, \tag{2.17}$$

$$\Phi = 0 \quad \text{for} \quad \xi > \delta, \tag{2.18}$$

the far-field behaviour is:

$$\Phi \to 0 \quad \text{as} \quad \xi, \eta \to \infty \tag{2.19}$$

$$\mathcal{H} \to 0 \quad \text{as} \quad \xi \to \infty, \tag{2.20}$$

and the self-similar version of Wagner condition is finally given by:

$$\mathcal{H}(\xi) = \frac{1}{2}\xi^2 - 1 \quad \text{for} \quad \xi = \delta. \tag{2.21}$$

This problem can now be solved in several steps.

▷ **Resolution.**   We look for an harmonic solution for the potential of the form:

$$\Phi(\xi, \eta) = \int_0^\infty \mathcal{C}(k)J_0(k\xi)e^{-k\eta}\,\mathrm{d}k. \tag{2.22}$$

The weight function $\mathcal{C}(k)$ is determined with boundary conditions (2.17) and (2.18), leading to the following pair of dual integral equations:

$$\begin{cases} \displaystyle\int_0^\infty k\mathcal{C}(k)J_0(k\xi)\,\mathrm{d}k = -1 & \text{for } \xi < \delta, \tag{2.23a} \\[2ex] \displaystyle\int_0^\infty \mathcal{C}(k)J_0(k\xi)\,\mathrm{d}k = 0 & \text{for } \xi > \delta. \tag{2.23b} \end{cases}$$

Solving these dual integral equations using the technique described in Sneddon, (1960), we obtain a closed-form expression for the weight function:

$$\mathcal{C}(k) = \frac{2}{\pi}\frac{\delta k \cos(k\delta) - \sin(k\delta)}{k^2} = \frac{2}{\pi}\frac{\mathrm{d}}{\mathrm{d}k}\left(\frac{\sin(k\delta)}{k}\right). \tag{2.24}$$

Anticipating the description of the contact line dynamics, we now derive $\partial\Phi/\partial\eta$ at the substrate level $\eta = 0$:

$$\frac{\partial\Phi}{\partial\eta} = -\frac{2}{\pi}\int_0^\infty \frac{k\delta\cos(k\delta) - \sin(k\delta)}{k^2}J_0(k\xi)k\,\mathrm{d}k, \tag{2.25}$$

where we recognize the sum of two Hankel transforms (see e.g. Sneddon, 1995, table IV, page 528). This allows us to obtain the following explicit expression for $\partial\Phi/\partial\eta$ for $\eta = 0$:

$$\frac{\partial\Phi}{\partial\eta} = 1 \text{ for } \xi < \delta \quad \text{and} \quad \frac{\partial\Phi}{\partial\eta} = -\frac{2}{\pi}\left(\frac{\delta}{\sqrt{\xi^2 - \delta^2}} - \arcsin\left(\frac{\delta}{\xi}\right)\right) \text{ for } \xi > \delta. \tag{2.26}$$

This result was originally obtained by Schmieden, (1953) in the water entry framework. With the help of the vertical velocity expression in the near wall region just derived, we can rewrite the kinematic boundary condition (2.16) as:

$$\mathcal{H}(\xi) - \frac{1}{2}\xi\frac{\partial\mathcal{H}}{\partial\xi}(\xi) = \frac{2}{\pi}\left(\frac{\delta}{\sqrt{\xi^2 - \delta^2}} - \arcsin\left(\frac{\delta}{\xi}\right)\right) \text{ for } \xi > \delta. \tag{2.27}$$

This inhomogeneous differential equation can be solved using variation of parameters, *i.e.* looking for a solution of the form $\mathcal{H}(\xi) = \xi^2 f(\xi)$. This gives:

$$\left[f(\xi)\right]_\delta^{+\infty} = -\frac{2}{\pi}\int_\delta^\infty \frac{2}{\xi^3}\left(\frac{\delta}{\sqrt{\xi^2 - \delta^2}} - \arcsin\left(\frac{\delta}{\xi}\right)\right)\mathrm{d}\xi. \tag{2.28}$$

Upon using the far-field decaying behaviour of $\mathcal{H}$ (see equation (2.20)), this last equation reduces to $f(\delta) = \frac{1}{2}\delta^{-2}$ so that at the contact line the drop deformation is:

$$\mathcal{H}(\delta) = \delta^2 f(\delta) = \frac{1}{2}. \tag{2.29}$$

In the self-similar space, the Wagner condition therefore takes the following remarkably simple form:

$$\frac{1}{2} = \frac{1}{2}\delta^2 - 1, \tag{2.30}$$

from which we finally derive the position of the contact line:

$$\delta = \sqrt{3}. \tag{2.31}$$

▷ **Lamb's analogy and the flow around a disk.** In §2.1.1 we proposed to visualize the flow in an impacting drop as the one induced by a flat rising disk expanding radially as the wet area (see also Fig. 2.3). We are now in a position to formally justify this water-entry analogy. The axisymmetric flow induced by *'the motion of a thin circular disk with velocity U normal to its plane, in a infinite mass of liquid'* is for example analysed in Lamb's classic textbook §101 (Lamb, 1932). After deriving some elementary axisymmetric solutions of Laplace equation of the form $\exp(\pm kz)J_0(kr)$ in §100, Lamb examined a variety of axisymmetric potential flows. Among those was the one (later connected to the flow around a flat circular disk in normal incidence) where at the symmetry plane $z = 0$ the potential takes the value $\phi = C\sqrt{a^2 - r^2}$ for $r < a$ and $\phi = 0$ for $r > a$, with a the disk radius. The solution for this problem was stated under the following integral representation:

$$\phi(r, z) = -C\int_0^\infty e^{-kz}J_0(kr)\frac{\mathrm{d}}{\mathrm{d}k}\left(\frac{\sin ka}{k}\right)\mathrm{d}k. \tag{2.32}$$

And from *'a known theorem in Electrostatics'*, Lamb obtained the expression for the vertical velocity in the symmetry plane:

$$-\left(\frac{\partial\phi}{\partial z}\right)_{z=0} = \begin{cases} \frac{1}{2}\pi C & \text{for } r < a, \tag{2.33a} \\[2ex] C\left(\arcsin\left(\frac{a}{r}\right) - \frac{a}{\sqrt{r^2 - a^2}}\right) & \text{for } r > a. \tag{2.33b} \end{cases}$$

This corresponds precisely to the flow within the impacting drop, after posing $C = -2/\pi$ and $a = \delta$, thereby justifying formally our initial analogy between the impact-induced flow with the one associated with a flat rising disk rapidly expanding with the wet area. Figure 2.6 offers a comparison between the streamlines of this Lamb analogy (see Philippi
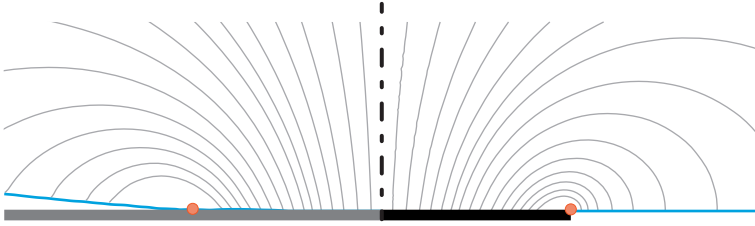
FIG. 2.6 – **Instantaneous streamlines in Lamb's problem and in simulations.** Comparison between the flow pattern within an impacting drop (left) and around a rapidly expanding disk (Lamb analogy, right) in the self-similar space. In both cases, the streamlines are represented in the moving frame. The red dots represent the theoretical position of the contact line $\xi = \sqrt{3}$. The numerical streamlines represented on the left are derived from the velocity field computed with *Gerris* at short times. The theoretical streamlines are shown on the right (note the correspondence with Lamb's figure page 145).

et al., 2016, for details) and the ones computed with *Gerris* for the drop impact problem in the self-similar space. A good overall agreement between the analytical and the numerical streamlines is manifest, comforting the expanding disk analogy followed here. Interestingly the winding motion around the contact line, as well as the falling velocity overshoot near this region, are both captured with this analogy and can be correlated with the peculiarities of the winding flow near the edge of a rising disk.

Similarly the pressure can be derived as the time derivative of the potential. In the self-similar space, the pressure field is given by equation (2.15). Figure 2.7 proposes a comparison between the structure of the self-similar pressure extracted from numerical computations performed with *Gerris* and the theoretical prediction. There it can be seen that the overall structure of the pressure field developing in the impacting drop, and in particular the pressure peak in the vicinity of the contact line already pinpointed out in Fig. 2.1, nicely matches with the theory. Interestingly, the structure just described is at variance with the pressure distribution around a flat disk rising steadily (Lamb's original problem). Indeed in such a configuration the pressure is expected to be maximal in the stagnation point area, whereas in our model problem the pressure peaks near the contact line/disk edge. This is a consequence of the motion unsteadiness: the pressure is here dominated by the $\partial\phi/\partial t$ contribution rather than the steady $\frac{1}{2}\nabla\phi^2$ term.
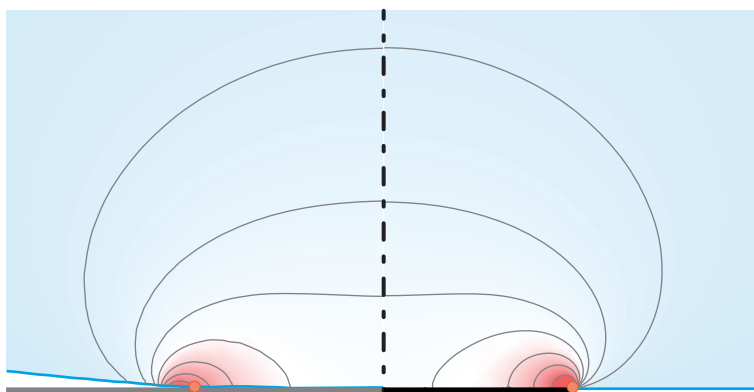
FIG. 2.7 – **Pressure field in the model and in the numerics.** Comparison between the pressure field developing inside an impacting drop (left) and around a rapidly expanding disk (Lamb analogy, right). The pressure field represented on the left is extracted from *Gerris* computations and represented in the self-similar space (isovalues: 0.12, 0.24, 0.36, 0.48, 0.6, 0.72, 0.84). The self-similar theoretical pressure field represented on the right is given by equation (2.15) (isovalues: 0.13, 0.28, 0.445, 0.57, 0.73, 0.9, 1.2). Though isovalues have been slightly changed between the two panels, theoretical and numerical results are in a good overall agreement.

2.1.3 Mirels' analogy, and the particular boundary layer of drop impact

The inertial limit (large Reynolds number) investigated thus far has allowed for a self-similar potential description of the impact-induced flow in nice agreement with the numerical results, both qualitatively and quantitatively (see e.g. Figs. 2.7 and 2.6 and Philippi *et al.*, 2016). Viscous effects are here dominating only in very thin boundary layers developing along the web substrate. And indeed, a careful examination of the numerical results reveals the presence of these thin layers in the very vicinity of the solid wall. Even if spatially confined, these boundary layers nonetheless play a key role when comes e.g. the question of the erosion potential of an impacting drop.

It appears that a classical boundary layer analysis (neglecting nonlinear terms and the pressure gradient) leads to a paradoxical cancelling of shear stresses at the wall. This unreasonable result stems from the fact that the sharp longitudinal variations associated with the contact line motion have here been disregarded. Specifically non linear terms do balance unsteady terms, at least near the contact line location $r = \sqrt{3t}$. As a result, the boundary layer actually grows from this moving point both in space and time. While a comprehensive analysis of this problem demands a careful balance of each term likely resulting in a non linear boundary layer problem, beyond the scope of the present study, we nonetheless propose in the following an approximation based on an analogy with boundary layers developing behind shockwaves.

First remembering the tank-treading movement in the vicinity of the contact line, we point out the violent change in radial velocity when passing through the contact line. In
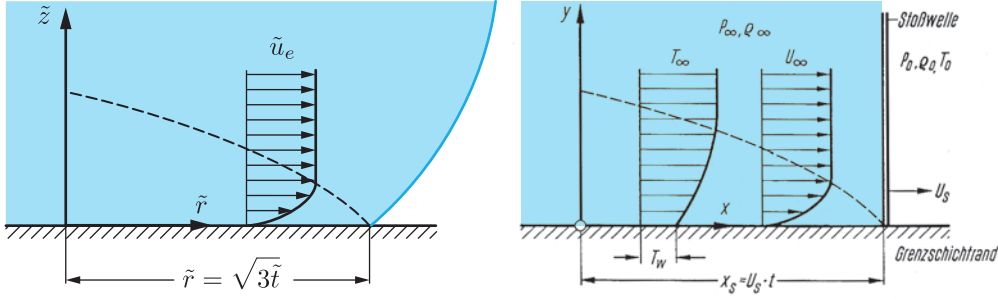
FIG. 2.8 - **An analogy with shock-induced boundary layers.** Left: Sketch of the contact line during its motion and of the growing boundary layer in its trail, analogous to that developing behind a shockwave. Right: Shockwave-induced boundary layer, reproduced from the german edition of Schlichting textbook (Schlichting, 1968). Notations are from Schlichting, with a correspondence between x and r. Note that in the shockwave case, U_∞ and U_s are both constant.

other words, the contact line embodies a neat discontinuity where the slip velocity sees its value suddenly change from 0 to u_e. Building on this observation, we consider in the following the contact line as a kind of shock wave sweeping the substrate, and seeding a boundary layer in its trail (see figure 2.8). This problem is classic in compressible flows and was solved by Mirels, (1955) in the context of a shock tube (see Schlichting, 1968, for more details). In this study, a fluid initially at rest is swept by a shockwave travelling at celerity U_s in the direction x and instantly acquires an impulse of velocity U_∞ in the process. Behind the normal shockwave is left a growing viscous boundary layer.

The *Ansatz* for Mirel's solution is to introduce $\eta_m = z/\sqrt{t - x/U_s}$ as the self-similar variable. This variable not only takes into account time variations but also longitudinal effects from the shock backwards in x. Disregarding any pressure gradient but considering both unsteady and nonlinear effects, the momentum equation may be rewritten in terms of η_m and of the velocity $U_\infty f'(\eta_m)$:

$$f'''(\eta_m) + \frac{1}{2}(\eta_m - \frac{U_\infty}{U_s}f(\eta_m))f''(\eta_m) = 0, \text{ with } f(0) = f'(0) = 0, \text{ and } f'(\infty) = 1. \quad (2.34)$$

Two limiting cases clearly emerge from the picture. For large U_∞/U_s (and after a rescaling and a change of sign due to the choice of origin), the velocity profile tends to a Blasius profile. Conversely, for small values of the velocity ratio, the velocity rather adopts an error function profile. Note that profiles corresponding to intermediate values of this ratio can be found in Schlichting's textbook. From this sound result we may by analogy transpose this approach to the drop impact problem (see Fig. 2.8). Obviously the outer solution for the drop impact problem is quite more complex for neither U_s nor U_∞ are constant. The core idea consists in drawing a parallel between the shock (at position U_st) and the contact line (at position $\sqrt{3t}$) on the one hand, and between the steady slip velocity U_∞

and $u_e(r,t)$ on the other hand. Following this simple analogy the longitudinal velocity is approximated with:

$$U_r(r,z,t) = \frac{2r}{\pi\sqrt{3t-r^2}}\,f'\left(\frac{z}{2\sqrt{t-r^2/3}}\sqrt{\text{Re}}\right) = \frac{2}{\pi}\frac{\xi}{\sqrt{3-\xi^2}}f'\left(\frac{\eta\sqrt{\text{Re}}}{2\sqrt{1-\xi^2/3}}\right) \quad (2.35)$$

where f' is solution of an equation which is analogous to Eq. (2.34). The so-called composite solution (Van Dyke, 1975), which is an expansion valid in the ideal fluid and in the boundary layer, then follows:

$$\begin{aligned}\tilde{u}_r^{\text{comp}} = &-\frac{2}{\pi}\int_0^\infty \frac{\sqrt{3}k\cos(\sqrt{3}k)-\sin(\sqrt{3}k)}{k}e^{-k\eta}J_1(k\xi)\,\mathrm{d}k \\ &+\frac{2}{\pi}\frac{\xi}{\sqrt{3-\xi^2}}\left(f'\left(\frac{\eta}{2\sqrt{1-\xi^2/3}}\sqrt{\text{Re}}\right)-1\right).\end{aligned} \quad (2.36)$$

In practice we approximated f' with erf function. The inset shows a comparison between numerical velocity profiles extracted from *Gerris* computations at different times and space corresponding to $\xi = 1.5$ and the present theoretical approximation (red dashed line), which proves to provide a fairly good description for the flow. The collapse of the different numerical profiles onto a single curve in the self-similar space is noticeable, and the agreement with the boundary layer prediction is remarkable. Noteworthy enough, the self-similar variables entering in

$$\left.\frac{\tilde{u}_r^{\text{comp}}(\xi,\eta)}{\tilde{u}_e(\xi)}\right|_{\xi=1.5}$$

the description of the boundary layer are the exact same self-similar variables used in impact-induced flow problem. This allows for a seamless representation of the velocity field in Eq. 2.36 encompassing both impact and viscous effects.
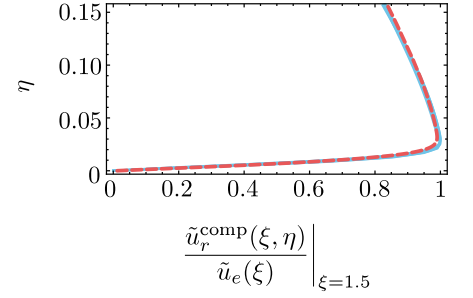
▷ **A note on the impact forces.** From our theoretical predictions we can infer the value of the normal force exerted on impact at short times from the pressure knowledge:

$$F(t) = \frac{1}{\sqrt{t}}\iint_{\mathcal{S}}\mathcal{P}(\xi,\eta=0)\,\mathrm{d}S. \quad (2.37)$$

But interestingly, note that $F(t)$ can also been inferred directly from energy arguments, with no knowledge of the pressure distribution. Indeed, writing the global kinetic energy conservation for the upper semi-infinite space, we have:

$$\frac{\mathrm{d}}{\mathrm{d}t}T = -\oint p\,\boldsymbol{u}\cdot\boldsymbol{n}\,\mathrm{d}S, \ \text{where } T = \left(\iiint\frac{\rho u^2}{2}\,\mathrm{d}V\right). \quad (2.38)$$

In the context of a flat rising disk, the kinetic energy reduces to $T_{\text{disk}} = \frac{4}{3}\rho a^3 U^2$ (Lamb §102). This expression can immediately be transposed to the impacting drop problem

so that $T = 4\sqrt{3}\rho U^{7/2} R^{3/2} t^{3/2}$. The power of pressure forces then follows as $\frac{\mathrm{d}}{\mathrm{d}t}T = 6\sqrt{3}\rho U^3 R^2 \left(\frac{Ut}{R}\right)^{1/2}$. Dividing this power by U, we obtain the (dimensional) net normal total force.

$$F(t) = 6\sqrt{3}\rho U^{5/2} R^{3/2}\sqrt{t}. \tag{2.39}$$

This alternate derivation of the normal force provides with yet an other illustration of the relevance of Lamb's analogy for the drop impact problem.

From the structure of boundary layer we may also estimate the integrated shear stress (which can be viewed as the erosion potential)

$$D(t) = \int_0^{2\pi}\int_0^{\sqrt{3t}} \tau(t)\, r\,\mathrm{d}r\,\mathrm{d}\theta, \tag{2.40}$$

where τ is the wall shear stress. As is, this expression diverges. Most presumably, a physical cut-off regularizes this expression but this requires to describe the solution at higher order. Actually, it appears from the numerical simulations that the integrand saturates at a fixed distance from the contact line in the self-similar space. We do not want to elaborate on this point here and refer the interested reader to Philippi *et al.*, (2016) for further details. Let's simply note as a conclusion that the (dimensional) integrated shear stress is closely approximated by:

$$D(t) \simeq 10.7\mu^{\frac{1}{2}}\rho^{\frac{1}{2}}U^2 R\sqrt{t}. \tag{2.41}$$

2.2   Drop impact on a soft substrate

Following the impact of a liquid droplet onto a solid surface, a splash may be triggered. This splash may be a desirable feature if one wants to coat a given surface, but it may also represent a nuisance in inkjet printing or splash-induced disease dissemination in plants. Many parameters influence splash formation and the current research still tries to disentangle the root of this phenomenon. For example, about a decade ago only, a team from the James Frank Institute in Chicago demonstrated the critical role of air pressure, long thought to be secondary, in triggering the splash process (Xu *et al.*, 2005). In this last section we outline a starting colloboration with Rob Style at ETH Zürich, Alfonso Castrejón-Pita at the Mechanical Engineering Dept in Oxford and Sam Howison and James Oliver at the Mathematical Institute of Oxford as well. Within the framework of this collaboration, we got interested in the possibility of controlling the splash appearance with the stiffness of the substrate, see Fig. 2.9. To shed light over the role of substrate deformation into splash suppression, we performed some numerical simulations with *Basilisk* (the successor of *Gerris*, also written by Stéphane Popinet, see http://basilisk.fr). In these simulations, dynamic contact angle effects were not implemented and a constant value of π – corresponding to the high-velocity limit – was chosen for the wetting angle. The soft substrate was modeled as a simple Kelvin-Voigt solid deforming in reaction to the applied pressure with the following constitutive law:

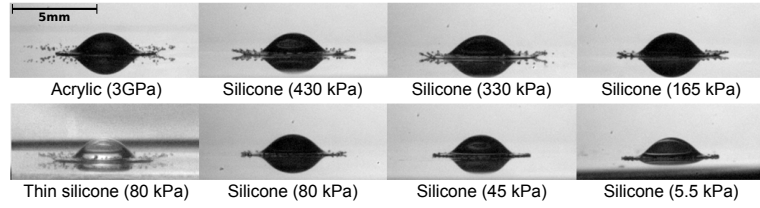$$k\frac{\dot{y}}{U} + \eta\frac{y}{R} = \frac{p}{\rho U^2} \quad \text{on the substrate surface,} \tag{2.42}$$

FIG. 2.9 - **Soft impact.** Examples of ethanol droplet impacts on flat substrates with a range of stiffnesses. All droplets have a radius of 0.88±0.02 mm and impact speed of 2.61±0.02 m/s. Images shown are taken approximately 350 μs after impact. All silicone substrates are 10 mm thick, except the bottom left image which is 3 μm thick. The scale bar is the same for all eight images. (Experiments by Rob Style and Alfonso Castrejón-Pita)

y corresponding to the wall deformation. Making use of the fact that the substrate displacements were small, we flattened this boundary condition, i.e. we linearised it so that it is applied at the initial position of the substrate throughout the droplet motion. The numerical implementation of the soft substrate therefore amounted to the following:

1. At each time step, compute the entire pressure field with the Navier-Stokes solver,

2. From the knowledge of the pressure on the fluid-solid interface, deduce the substrate instantaneous velocity from equation (2.42),

3. Feed this velocity into an inhomogeneous Dirichlet condition for the fluid normal velocity at the wall.

The modification of the boundary velocity then reflects into the evaluation of the fluid pressure at the next timestep, therefore allowing to efficiently couple the subtrate deformation with the drop dynamics.

These simulations allow to reveal the pressure as the key control for splash formation. Figure 2.10 illustrates the typical evolution of the maximum pressure measured over the substrate, with a rise as the drop approaches and touches the substrate, followed by an algebraic decline following sheet ejection. Remarkably the pressure fall-off in neat agreement with the second-order Wagner theory $p_{\max} = 3\rho RU/8(t - t_i)$ with t_i the time of impact in absence of air cushioning, an expression which follows from Wagner theory's asymptotic results that $p_{\max} = \rho \dot{a}^2/2$ (Howison *et al.*, 1991). The simulations also allow us to understand why p_{peak} is lower (and thus splashing is less likely) on softer substrates. We find that a reduction in p_{peak} is associated with downwards substrate motion, as this reduces liquid deceleration on the substrate. Significant substrate motion does not occur until when p_{peak} exceeds the substrate's modulus, E. Thus splash reduction by a soft substrate can only occur when

$$p_{peak}^r = \frac{\rho RU}{(t_{ej}^r - t_i^r)} \gtrsim E. \tag{2.43}$$
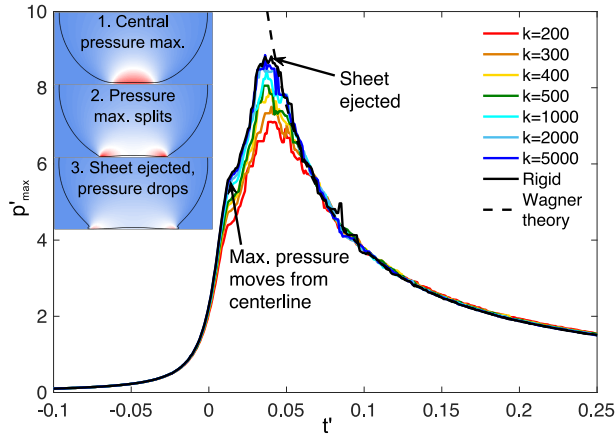
FIG. 2.10 – **Fall-off of peak pressure on soft substrates.** Simulations give the maximum pressure $p'_{max} \equiv p_{max}/\rho U^2$ exerted on a substrate as a function of time $t' \equiv (t - t_i)U/R$. The insets illustrate how the pressure distribution evolves in an impacting droplet (here impacting a rigid substrate). p'_{max} reaches a peak at the point of sheet ejection before decaying following Wagner theory's prediction $p'_{max} = 3/8 \, t'$ (dashed curve).

Here superscript r's refer to impact on a rigid substrate. This result agrees with our experimental results. Using the typical data experiments, we take $R = 1.5$mm, $U_c = 2.36$m/s, $t^r_{ej} - t^r_i = 30\mu s$ and $\rho = 789$kg/m^3, to find $E_c = 93$kPa. This is consistent with substrate stiffnesses where we start to observe significant reductions in splashing.

This outline of a current work provides an illustration of the impact of elasticity on drop dynamics. It also preludes the next chapter where we now turn to the study of drop interacting with soft and, this time, thin elastic substrates.

3 | Elasticity with Interfaces

When we think of how a fluid could deform a solid body, we probably picture a flapping flag, algae or cables fluttering with waves or vibrating vocal chords. In these examples, the fluid structure interaction is mediated with fluid inertia. But at small scales, inertia and body forces can become subdominant with respect to surface forces if interfaces are present, as for example in the context of droplet sitting on a soft object. Specifically the ratio of surface over volume becomes increasingly larger at small scales, thereby promoting the emergence of surface tension as a leading force in this limit. This particular type of fluid-structure interaction, where surface tension deforms and shapes elastic surroundings has been coined elastocapillarity in the recent literature. These phenomena are quite counter-intuitive at the human scale, but can have tremendous effects in broad areas, such as neonatal pulmonary collapse, clumping of wet hairs, splash suppression as we just saw in the last chapter or even play a crucial role in spider silk mechanics as we will see in chapter 4 (see Roman and Bico, 2010, for a review). The statics and dynamics of elastocapillarity involving slender structures along with the identification of the key physical parameters governing these effects form the main matter of the present chapter.

3.1 Elastocapillarity statics

3.1.1 A simple model

Let's start by introducing a worked out example illustrating the energetics of elastocapillarity in a 2D setting. We first consider a long rigid plate of length L. The surface energy of the plate would then be $\gamma_{\mathrm{sv}} L$, where γ_{sv} is the surface energy of the plate per unit area (remember that in our 2D setting, all results have to be understood per unit length in the transverse direction). But for simplicity we choose to subtract this quantity in our definition of energy E, so that the dry plate has the reference energy $E = 0$.

We now consider three situations involving a liquid drop:

i) In the first situation, we introduce a drop of radius R and surface tension with the surrounding vapour $\gamma_{\ell\mathrm{v}}$. The drop does not interact with the substrate and lies at a distance from it. In absence of gravity, the drop reaches a circular shape and the total energy of the system is $E_0 = 2\pi R \gamma_{\ell\mathrm{v}}$, see Fig. 3.1. To put figures, if we are dealing with a millimeter-sized water droplet in this 2D world, we would have $R = 1$ mm, $\gamma_{\ell\mathrm{v}} = 72$ mJ·m^{-2} and $E_0 = 4.52 \times 10^{-4}$ J/m.

ii) Now we make the drop contact the solid. If we know the interaction energies between the substances, can we predict the shape of the droplet on the substrate? Of course we can, because we know Young-Dupré equation relating the contact angle of the circular cap with the energies. But actually we could calculate this angle without having recourse to this additional relation; simply stating that the total energy of the system E is minimal is sufficient to determine it. For the purpose of this example, we work out in the following this minimization.

The total energy of the system is here $E \equiv E(R_{\mathrm{cap}}, \theta, D)$, with:

$$E(R_{\mathrm{cap}}, \theta, D) = 2\theta R_{\mathrm{cap}} \gamma_{\ell\mathrm{v}} + 2D\Delta\gamma, \tag{3.1}$$

where θ is the contact angle, D the wet half-length, and $\Delta\gamma = \gamma_{\mathrm{s}\ell} - \gamma_{\mathrm{sv}}$ the energy difference between the wet and the dry solid (positive is solid is hydrophobic, and negative if it is hydrophilic). Further recalling that the volume of the drop cannot change during the minimization process and that D must be related to R_{cap} and θ, we end up with the following constrained minimization problem:

Search $(R_{\mathrm{cap}}, \theta, D)$ minimizing $E(R_{\mathrm{cap}}, \theta, D)$ subject to the constraints of:
> *constant drop volume:* $\mathcal{V} = \theta R_{\mathrm{cap}}^2 - D R_{\mathrm{cap}} \cos\theta - V = 0,$ (3.2)
> *geometrical dependence:* $\mathcal{G} = D - R_{\mathrm{cap}} \sin\theta = 0.$

This constrained minimization problem can conveniently be rewritten as an unconstrained minimization problem by introducing the following Lagrange functional:

$$\mathcal{L}(R_{\mathrm{cap}}, \theta, D, \lambda, \mu) = E(R_{\mathrm{cap}}, \theta, D) - \lambda\mathcal{V} - \mu\mathcal{G}. \tag{3.3}$$

Here λ and μ are Lagrange multipliers enforcing the constraints directly into the functional. This variational problem can be solved by looking for an extremal point of the functional, that is, a 5-tuplet $(R_{\mathrm{cap}}, \theta, D, \lambda, \mu)$ satisfying:

$$\begin{cases} \dfrac{\partial\mathcal{L}}{\partial R_{\mathrm{cap}}} = 2\theta\gamma_{\ell\mathrm{v}} - 2\lambda\theta R_{\mathrm{cap}} + \lambda D\cos\theta + \mu\sin\theta = 0, & \text{(3.4a)} \\[2mm] \dfrac{\partial\mathcal{L}}{\partial\theta} = 2R_{\mathrm{cap}}\gamma_{\ell\mathrm{v}} - \lambda R_{\mathrm{cap}}^2 - \lambda D R_{\mathrm{cap}}\sin\theta + \mu R_{\mathrm{cap}}\cos\theta = 0, & \text{(3.4b)} \\[2mm] \dfrac{\partial\mathcal{L}}{\partial D} = 2\Delta\gamma + \lambda R_{\mathrm{cap}}\cos\theta - \mu = 0, & \text{(3.4c)} \end{cases}$$

and the constraints $\mathcal{V}$ and $\mathcal{G}$. Combining (3.4a)$R_{\mathrm{cap}}\cos\theta$ with (3.4b)$(-\sin\theta)$ allows to reveal λ, the volume constraint Lagrange multiplier, as the drop pressure:

$$\lambda = \frac{\gamma_{\ell\mathrm{v}}}{R_{\mathrm{cap}}}. \tag{3.5}$$

FIG. 3.1 - **A 2D energetical view on elastocapillarity.** We start by considering a rigid ground (reference energy level). *i)* A droplet is introduced and adopts a circular shape. The energy of this configuration is $E_0 = 2\pi R\gamma_{\ell v}$. *ii)* If the drop touches the substrate, the total energy is lowered to 9.4% E_0 for the parameters used in the model (see text). Note that the exposed free surface is extended, but that the energy gained by wetting the surface largely compensates for this additional cost. If the wet footprint was larger, the cap would have a too large area and the energy would be higher. If the footprint was smaller, the energy gain by wetting would not be maximal. The better trade-off therefore corresponds to this situation where the contact angle of 20° is given by Young-Dupré wetting relation. *iii)* If the surface is made flexible, the elastic energy cost of bending is again largely recovered by the less exposed free surface allowed by this folded configuration. The energy is here 1% E_0.

Young-Dupré's wetting relation then naturally arises from this set of equations. Indeed, writing (3.4b) + (3.4c)$R_{cap} \cos\theta$ gives:

$$\gamma_{\ell v} \cos\theta + \Delta\gamma = 0. \tag{3.6}$$

From this relation the contact angle θ follows.

Carrying on with our previous example, if we suppose that the substrate is wetting with $\Delta\gamma = -67.66$ mJ·m^{-2}, we find a contact angle of the spherical cap of 20° (see Fig. 3.1). The total energy of the system is then $E = 4.25 \times 10^{-5}$ J/m, which is 9.4 % of the initial energy budget: so there is a large pay-off achieved by wetting the substrate. But it is interesting to look at how this energy E is distributed. The liquid-air cap surface energy is now 5.36×10^{-4} J/m, or 119 % E_0! But the energy gained by wetting the substrate (-4.25 $\times 10^{-5}$ J/m) largely outweighs this additional energy cost. Energy minimization is a global process, and does not mean that each contribution in energy component have to be a minimum – this example illustrates quite the opposite.

iii) Suppose now that the substrate is a thin elastic lamella. This lamella can be distorted by the pulling action of surface tension, but can we make an estimate of this deformation, and of the resulting energy gain? To start with, let's neglect the action of gravity and approximate the shape of the elastic strip under the drop by a circular arc of radius θ_{bend} subtended by the angle $2\theta_{bend}$. Similarly we note R_{cap} and

θ_{cap} the corresponding radius and angle for the liquid cap. This model, probably oversimplified (e.g. exhibiting curvature discontinuities), is nonetheless sufficient for the present illustration.

The Lagrange functional for this problem now reads:

$$\mathcal{L}(R_{bend}, \theta_{bend}, R_{cap}, \theta_{cap}, D, \lambda, \mu, \xi) = E(R_{bend}, \theta_{bend}, R_{cap}, \theta_{cap}, D) \\ - \lambda \mathcal{V} - \mu \mathcal{G}_1 - \xi \mathcal{G}_2, \tag{3.7}$$

where the energy is now:

$$E(R_{bend}, \theta_{bend}, R_{cap}, \theta_{cap}, D) = 2\theta_{cap} R_{cap} \gamma_{\ell v} + 2\theta_{bend} R_{bend} \Delta\gamma + \frac{EI\theta_{bend}}{R_{bend}}, \tag{3.8}$$

the last term corresponds to the bending elastic energy $\frac{1}{2} \int EI\kappa^2 ds$ involving the bending stiffness EI of the strip and the curvature $\kappa \equiv 1/R_{bend}$ (Audoly and Pomeau, 2010). The volume and geometrical constraints here read:

$$\mathcal{V} = R_{bend}^2 \theta_{bend} - R_{bend} \cos\theta_{bend} D + R_{cap}^2 \theta_{cap} - R_{cap} R_{cap} D - V = 0$$
$$\mathcal{G}_1 = R_{cap} \sin\theta_{cap} - D = 0 \tag{3.9}$$
$$\mathcal{G}_2 = R_{bend} \sin\theta_{bend} - D = 0$$

The minimization proceeds then as previously, with straightforward (albeit lengthy) calculations. Even in this simple configuration, there is unfortunately no full analytical solution but the equations can still be solved numerically with a continuation procedure. Several messages can be learnt from these numerical resolutions. First, when the bending stiffness EI tends to infinity, the curvature of the strip falls sufficiently rapidly to 0 so that $\frac{1}{2} \int EI\kappa^2 ds \to 0$ in the rigid limit, as expected. Second, as previously we observe a trade-off between the different contributions in energies as minimization proceeds. More particularly, strip bending, undesirable at first sight because costly, can promote a reduction of exposed liquid surface, as illustrated Fig. 3.1. Whenever this energy gain exceeds the cost of bending, elastocapillary folding occurs.

If we pursue our numerical example, we can now suppose that the strip on which the drop sits has a bending stiffness $EI = 1.14 \times 10^{-7}$ J. The minimum energy configuration corresponds to a markedly deformed strip, see Fig. 3.1. The total energy of this setting is 4.53×10^{-6} J·m^{-1}, or 1 % E_0. Folding the strip has allowed to gain a factor 10 in energy in comparison with the rigid case. Note that in this configuration, the elastic energy stored in the folded strip corresponds to 12.5 % E_0 and the net surface energy is -11.5 % E_0, so that there is here almost an anti-equipartition of energy: each of the term can be quite important but almost exactly balance the other. This is not a general result, for following equilibria leads to negative energy states.

This elementary example already contains all the ingredients composing the elastocapillary interactions that will be reviewed in the remaining of this chapter. Interestingly, a more thorough analysis of the last example combining bending with capillary effects reveals a rich bifurcation diagram exhibiting fold (or limit) points for example. This type of bifurcation, and the possible coexistence of multiple stable equilibria, is commonplace in elastocapillary systems – and, as a matter of fact, in slender elastic objects. Such a bistability was first exemplified by Py *et al.,* (2007) who showed that a 2D drop drying on a strip could result on very different outcomes according to the value of the elastocapillary length $\sqrt{EI/\gamma}$. Below a critical threshold the strip would end up open, while above this threshold complete folding would occur, see inset. Noteworthy enough, open and closed

states coexist for every elastocapillary lengths, but sometimes there is a path smoothly connecting these states, and sometimes not. This bistability will for a large part be at the origin of phenomena such as snap-through buckling or selective folding presented in what follows.
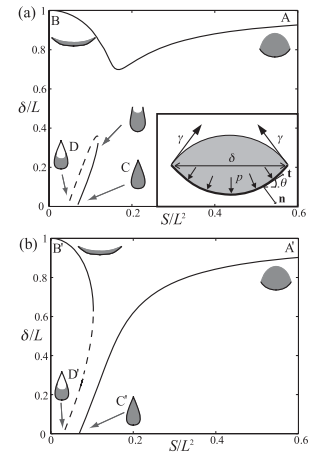
3.1.2   Capillary forces exerted on a soft object

An important concept in the study of elastocapillary phenomena is the one of force. Buckling, folding, packing of soft structures by liquid surfaces can all be thought to be mediated by forces of capillary origin. Recently there has been some debate on the nature of the force developed by liquid-gas interfaces contacting solid objects. The structure of this force – classically thought to be of intensity $\gamma_{\ell v}$ and lying along the interface (e.g. Adamson and Gast, 1997; de Gennes *et al.*, 2003) – has been challenged by some groups (Marchand *et al.*, 2012; 2011; Seveno *et al.*, 2013). The question raised here is an important one and deserves some attention, not only as far as elastocapillarity is concerned, but for wetting phenomena in general. Part of the reason why such a question can be raised today is that most of the experimental studies on wetting have focused on the shapes of interfaces, and not on the forces developed by those because of the obvious technical challenges to overcome for such a measurement (see however Guo *et al.*, 2013). Another might be that forces cannot be observed; only the effect (i.e. imparted deformation) of these forces can be witnessed.

An analysis of the forces at play near the contact line is a delicate matter, and subtle questions about the subsystems on/from which forces apply inevitably arise. On the other hand, there is a consensus about the energies involved, and conclusions reached following a energetical (i.e. variational) approach are clear-cut. In Neukirch *et al.,* (2013), we therefore followed such a variational approach and found the minimal energy state for a (2D) drop sitting on an inextensible Elastica (i.e. flexible filament). Interestingly, the equations describing this equilibrium state turned out to correspond exactly to the equations of an Elastica withstanding the Laplace drop pressure along the wet area **and point forces of intensity $\gamma_{\ell v}$ oriented along the interface at each meniscus** – that is, the classic

description of surface tension forces acting on solids. This sound result, obtained without any prior assumption on the forces at play, certainly substantiates the use of surface tension forces oriented along interfaces. Aside from this result the variational approach also evidenced the validity of Young-Dupré's wetting relation on flexible substrates (Neukirch *et al.*, 2013). Let's note however that for very soft objects of Young's modulus E (typically $O(\text{kPa})$) or very small droplets of radius R such $R \lesssim \gamma/E$ there can be significant distortion at the contact line and the last Young-Dupré's wetting relation ceases to hold and evolves towards a fluid-like Neumann construction (Style *et al.*, 2013).

▷ **A note on the constitutive relation of soft slender objects.** We just saw how a liquid interface pulls on a contacting object, but how this object deforms in reaction? Obviously within the framework of an inextensible Elastica no deformation (apart from bending) can be expected. But if we take into account the stretchiness of the fibre, then we expect Hooke's law $N = EA\,\varepsilon$ to hold, with N a longitudinal deformation, EA the stretching modulus and ε the deformation of the fibre. But does this constitutive relation stands true if we consider surface effects? To answer this question we considered in Neukirch *et al.*, (2014) the soft stretchable beam depicted in inset and bearing a tension force T. The equilibrium state of this rod can be found using the same variational approach introduced earlier. Specifically, the arc-length $x(s)$ and local extension $e(s)$ of such a rod minimize the following Lagrange functional:
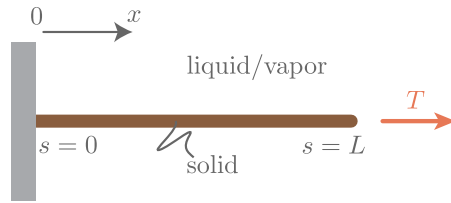
$$\mathcal{L}(x(s), e(s)) = V_\text{e} + V_\text{s} + W_T + \int_0^L \nu(s)\left[x'(s) - (1 + e(s))\right]\mathrm{d}s, \tag{3.10}$$

where $V_\text{e} = \frac{1}{2}\int_0^L EA\,e^2(s)\,\mathrm{d}s$ is the stretching energy, $V_\text{s} = \gamma P \int_0^L [1 + e(s)]\,\mathrm{d}s$ is the rod surface energy (P being the perimeter and γ the rod' surface energy), $W_T = -T\int_0^L x'(s)\,\mathrm{d}s$ is the work done by the external load and the continuous Lagrange multiplier $\nu(s)$ allows to enforce the definition of the strain $x'(s) = 1 + e(s)$. Introducing perturbations of the form $x \to x + \varepsilon\bar{x}$, $e \to e + \varepsilon\bar{e}$ we expand $\mathcal{L}$ as follows:

$$\mathcal{L}(x + \varepsilon\bar{x}, e + \varepsilon\bar{e}) = \mathcal{L}(x, e) + \varepsilon \left.\frac{\mathrm{d}\mathcal{L}}{\mathrm{d}\varepsilon}\right|_{\varepsilon=0} + \dots \tag{3.11}$$

Cancelling the first variation then implies:

$$\left.\frac{\mathrm{d}\mathcal{L}}{\mathrm{d}\varepsilon}\right|_{\varepsilon=0} = \int_0^L (EAe + P\gamma - \nu)\,\bar{e}(s) - \int_0^L \nu'(s)\,\bar{x}(s) - \left[(T - \nu)\bar{x}\right]_0^L \tag{3.12}$$

Requiring (3.12) to vanish for all $(\bar{x}(s), \bar{e}(s))$ brings a set of equations and natural boundary conditions allowing to interpret the Lagrange multiplier $\nu(s)$ as the beam internal tension $N(s)$, which appears to be governed by the following constitutive relation:

$$N(s) = EA\,e(s) + P\gamma. \tag{3.13}$$

This equation shows that Hooke's law should not be used directly for problems exhibiting surface stresses, but instead must include an offset accounting for the beam self-contraction under surface tension. This is actually analogous to Hooke's law in thermoelasticity where local stress is created by both strain and temperature change. The deformation due to interface energy is then analogous to the classic deformation observed when heating a beam away from its fabrication temperature, the surface energy γ playing the role of a negative thermal expansion coefficient (Landau and Lifshitz, 1959).

3.2 Capillary adhesion on soft objects

We just saw how many aspects of classic wetting and elasticity could be altered when dealing with soft objects. Adhesion is another trademark of capillarity: removing an object floating on a liquid surface requires more than to simply lift the weight of the object, because liquid surfaces stick. Actually the added force corresponds to the weight of the liquid column drawn behind the object, which could seem surprising at first glance for capillarity is the root cause of this adhesion. There is in fact no paradox because the liquid column is sculpted by surface tension, and therefore adhesion ultimately depends on capillarity. Laplace was to first to address this problem in his founding monograph on capillarity. Further, on his request Gay-Lussac undertook careful experiments on the traction of glass disks adhering to a liquid surface, and they obtained a beautiful agreement between experiments and this first-ever theory of capillarity (Laplace, 1805).

a)   b)
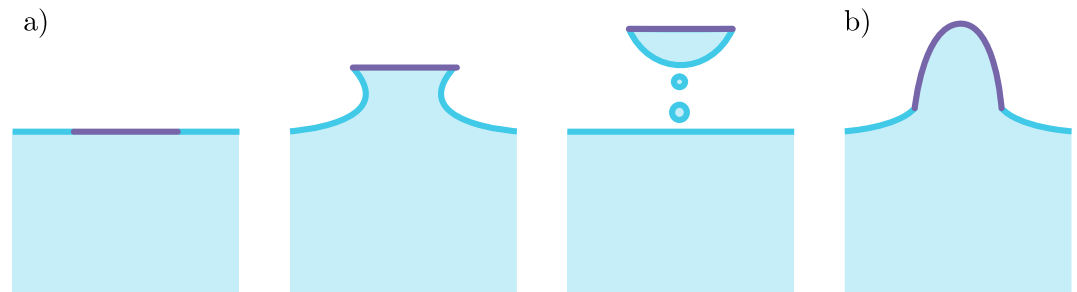
FIG. 3.2 - **Capillary adhesion.** a) The Laplace/Gay-Lussac problem. A flat and rigid object floats on a liquid surface. Upon pulling on the object, a liquid column, shaped by capillarity, is drawn behind it. The force needed to lift the object is therefore increased by the weight of the liquid column. Above a critical height, the meniscus spontaneously ruptures and the object is released. b) If the object is now made soft, we can expect the liquid drawn behind the column to change. Would that increase or lower capillary adhesion?

In view of the previous considerations, we might wonder: Do soft objects stick more – or less – to a liquid surface than their rigid counterpart? (see Fig. 3.2). To address this question, we designed during the PhD thesis of Marco Rivetti an Hele-Shaw cell containing a liquid and a clamped elastic strip. At initial time, we made the strip float onto the bath and we then slowly drained the cell, as illustrated Fig. 3.3. There we see how the strip

deforms under the combined action of hydrostatic pressure and capillary forces, forming an elasto-capillary meniscus. Above a critical depth, the liquid column suddenly ruptures, thereby releasing the soft object (Rivetti and Antkowiak, 2013).
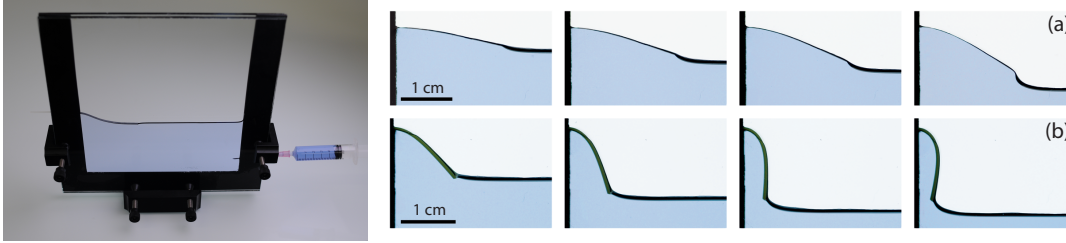
FIG. 3.3 - **Elastocapillary meniscus.** Left: experimental setup used to investigate soft capillary adhesion, consisting in a Hele-Shaw cell partly filled with liquid. A flexible strip is clamped within the cell and adheres to the liquid. Right: different configurations achieved by this elasto-capillary meniscus as the cell is drained or the stiffness of the strip changed. (a) Equilibrium configurations for a Mylar strip floating on water. The length of the strip here is L = 21 mm. From left to right, the meniscus height is respectively H= 5.0, 7.2, 8.9 and 12.5 mm. (b) Same snapshot sequence for a PVS strip resting on water. The length of the strip is L = 15.8 mm. From left to right, the meniscus height is respectively H= 10.7, 13.6, 16.1 and 16.6 mm.

A considerable insight into this problem can be gained by expliciting the equations governing the coupled shapes of the strip and of the fluid surface. If we start by introducing the notations of Fig. 3.4, we can write the equation describing the shape of the fluid meniscus as:

$$\psi''(S) = \frac{1}{L_{\text{gc}}^2}\sin\psi(S), \tag{3.14}$$

where $L_{\text{gc}} = (\gamma/\rho g)^{1/2}$ is the gravity-capillary length. In the limit where the meniscus vanishes far from the contact zone $\psi(S \to \infty) \to 0$, equation (3.14) has the following closed-form solution (Landau and Lifshitz, 1959):

$$\psi(S) = 4\arctan\left(\tan\frac{\psi_0}{4}\exp\left(-\frac{S}{L_{\text{gc}}}\right)\right). \tag{3.15}$$

Here ψ_0 is a constant whose value is in general linked to the contact angle at the end strip. If we now turn to the solid side, the equations governing the shape of the Elastica under distributed hydrostatic loading and end meniscus point force can be recast into the following compact form:

$$EI\,\theta'''(S) + \frac{EI}{2}\theta'(S)^3 + \gamma\theta'(S)\cos\varphi + \rho g(Y(S) + H) = 0, \tag{3.16a}$$

$$X'(S) = \cos\theta(S), \tag{3.16b}$$

$$Y'(S) = \sin\theta(S), \tag{3.16c}$$

with associated boundary conditions:

$$X(0) = 0 \quad ; \quad Y(0) = 0 \quad ; \quad \theta(0) = 0$$
$$\theta'(L) = 0 \quad ; \quad EI\,\theta''(L) = \gamma \sin\varphi \qquad (3.17)$$

These two problems are matched with the geometrical constraint expressing the anchoring of the meniscus at the strip edge:

$$Y_{\text{strip}}(L) = Y_{\text{meniscus}}(L). \qquad (3.18)$$

Figure 3.4 shows some (numerical) solutions of this coupled set of equations compared with experimental realizations.
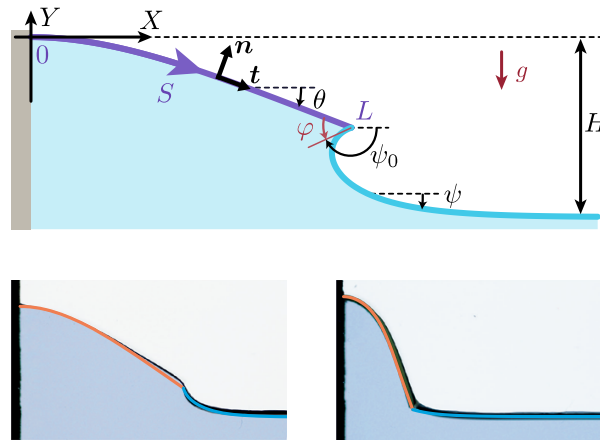
FIG. 3.4 – **Notations and comparison between theory and experiments.** Top: notations used to describe the elasto-capillary meniscus. Bottom: comparison between the theoretical profile and its experimental realization. Left: ℓ = 1.83, ℓ_{gc} = 0.24 and h = 1.09. Right: ℓ = 2.44, ℓ_{gc} = 0.48 and h = 2.06.

We may now wish to track these equilibria as the strip length L, the imposed depth H, the gravity-capillary length L_{gc} and the stiffness of the strip are varied. A convenient measure of the strip stiffness is actually another length: the elasto-gravity length $L_{\text{eh}} = (EI/\rho g)^{1/4}$, first introduced by Hertz, (1884) and Föppl, (1897) because naturally appearing in the buckling of a fluid supported slender structure. It is therefore convenient to non dimensionalize all lengths with L_{eh}, so that the problem depends on three parameters : $\ell = L/L_{\text{eh}}, h = H/L_{\text{eh}}$ and $\ell_{\text{gc}} = L_{\text{gc}}/L_{\text{eh}}$. In Fig. 3.5 we represent the path followed by the edge angle φ as the non-dimensional depth h is varied for various ℓ (keeping $\ell_{\text{gc}} = 0.24$ constant). When ℓ is close to 0 (black curve), the strip is very stiff, and the edge angle φ goes smoothly from π to 0 as the liquid depth increases. When $\varphi = 0$, the lamella snaps off and detaches suddenly from the liquid bath. This event occurs when $h = 0.48 = 2\ell_{\text{gc}}$, corresponding exactly to the Laplace/Gay-Lussac limit. When the lamella gets softer (coloured curves), significant distortion can take place, allowing to reach much larger depths.
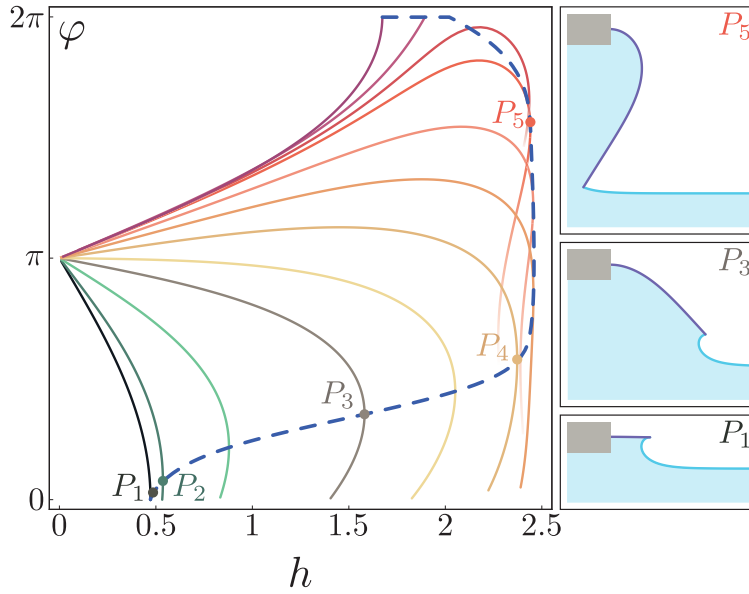
FIG. 3.5 – **Equilibrium limit.** Equilibria paths tracked by continuation in the (h,φ) plane. The curves correspond to increasing values of the nondimensional strip length ℓ, starting with a near zero value for the black curve (from bottom to top ℓ = 0.01, 1, 1.5, 1.8, 2, 2.2, 2.4, 2.6, 2.8, 2.9, 3, 3.2 respectively). Note the appearance of limit (or fold) points. The dashed blue line trace these limit points as ℓ is varied.

Noteworthy enough, most of the equilibrium branches exhibit a limit point. In other words, this means that for a given value of h two equilibria coexist – presumably one stable and the other unstable. But at the critical value, these two equilibria coalesce and then disappear : no equilibrium state exist past the limit point. This saddle-node (or fold) bifurcation is quite commonplace and akin e.g. to the catenoid (soap film held between two rings) problem. Past the limit point, the catenoid just bursts into droplets. In our case, the elasto-capillary meniscus ruptures and adhesion stops: the lamella is released.

If we were to predict the maximal depth reached by the elasto-capillary meniscus as the lamella length ℓ changes, we'd just have to connect the fold points and plot the corresponding path in the $(\ell, h_{\max})$ plane.

We have tested this theoretical prediction with experiments and found a good agreement between prediction and observation, except when the edge angle φ was very small. In this limit, pinning becomes faulty and contact line slipping occurs, making the prediction inaccurate. Such slipping can also be included in the theoretical prediction, and an hybrid pin-slip boundary condition prove to fully capture the experimental observations (see inset and Rivetti and Antkowiak, 2013). Comforted by this agreement, we are now in a position to address the central question asked at the beginning: Do soft objects stick
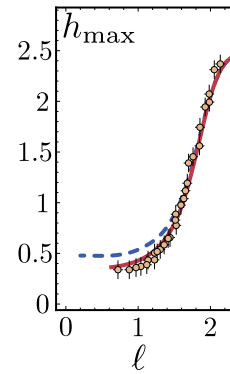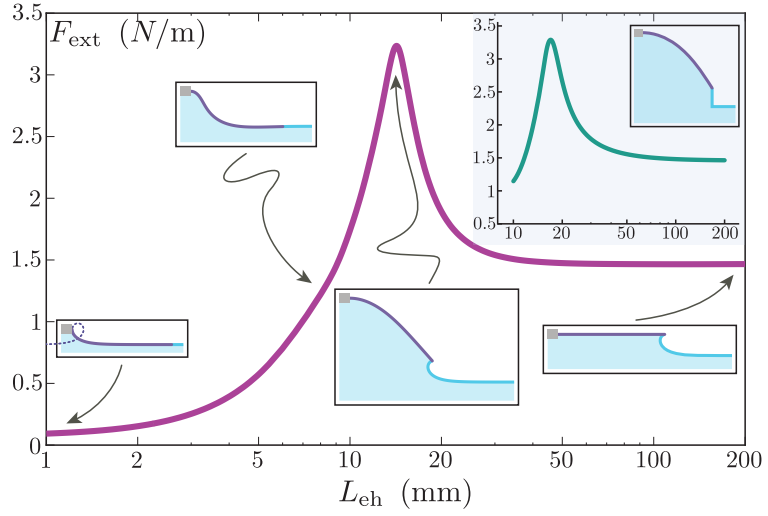
FIG. 3.6 - **Extraction force versus L_{eh}.** Relation between the dimensional extraction force per unit width F_{ext} (in N/m) and the rigidity of a fixed-length strip, here measured in terms of the elasto-hydrostatic length L_{eh} (mm). The length of the strip taken here is 27 mm and the gravito-capillary length L_{gc} has been set to 2.7 mm. The figure clearly displays an adhesion peak for a specific value of L_{eh} around 0.5 L. Representative snapshots of the elasto-capillary meniscus at the moment of extraction are disposed along the curve. These snapshots correspond to different régimes; From left to right: capillary limit, elasto-hydrostatic régime, optimal adhesion, rigid limit. In the inset, a rudimentary model where the strip is approximated with a linearly varying curvature rod and the meniscus with a vertical liquid wall proves to capture the main features of the main graph, both qualitatively and quantitatively.

more or less than their rigid counterpart? To answer this question we represent Fig. 3.6 the dimensional extraction force (which corresponds to the maximal force force reached in the extraction process, which does not correspond necessarily to the force at the maximal depth) versus the rigidity of a fixed-length lamella, measured with L_{eh}. For plotting purposes, the fixed length of the lamella and gravity-capillary length were chosen so as to match our experiment: $L = 27$ mm and $L_{\text{gc}} = 2.7$ mm, but the features presented appear to be generic. In the limit where L_{eh} is very large, the extraction force reaches a plateau corresponding to the rigid Laplace/Gay-Lussac limit. In the other extreme limit where L_{eh} tends to 0, the strip is so soft that it deforms with virtually no resistance. In this limit of vanishing elasticity, the whole shape of the elasto-capillary meniscus is that of a classic meniscus, entirely relying on capillarity and gravity, and the extraction force tends to 0. When L_{eh} is slightly larger, but still such that $L_{\text{eh}} \ll L$, it is the only relevant length as far as the strip deformation is concerned. This corresponds to a self-similar regime where $F \sim \rho g L_{\text{eh}}^2$. For still higher values of L_{eh} an adhesion peak clearly enters into the picture. This peak, occurring for $L \sim 0.5 L_{\text{eh}}$, signs the end of the self-similar regime imposed by

end effects, and points to a configuration where a soft object does stick more than its rigid counterpart. Note however that there is no simple answer to the original question we asked, as demonstrated Fig. 3.6.

To conclude this part, it is known that elasticity increases the energetic costs in adhesion phenomena, and to induce hysteric cycles with different deformations back and forth. For example, the long polymer chains in elastomers can store all the more elastic energy that the chain is long. This energy is lost when the chains rupture and that cracks initiate (Lake and Thomas, 1967). This feature is reproduced here, but a key point of the present analysis is also to highlight the existence of optimal strip stiffness corresponding to a maximal extraction force (conversely, this force can be as low as the material is soft). This could be exploited for example to improve the design of soft micro-manipulators or MEMS such as elastopipettes (Reis *et al.*, 2010).

Let's finally note that capillary adhesion, even in this elastocapillary version, is ultimately controlled by the capillary failure of the fluid meniscus – which at some point starts slipping, thereby promoting air invasion beneath the strip and finally the release of the stuck object. In the next two sections we now review two different elastocapillary dynamics which this time markedly depend on the elastic properties of the drop/strip compound.

3.3   Elastocapillary snapping, a capillary-induced elastic instability

When an arch or a buckled beam is loaded (see inset from Timoshenko, 1935), the structure may fail not necessarily as a result of yield or crack formation but because of an elastic instability. Snapping – or snap-through buckling – refers to this phenomenon. While such an instability is certainly detrimental for bridges, it may also be harnessed and promoted for
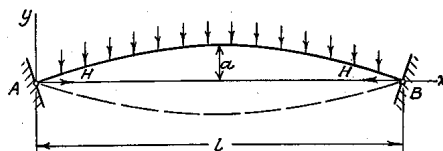
the design of bistable switches and actuators, and most notably of thermo-bimetallic strips able to snap on and off the electrical circuit of a boiler or a fridge according to the surrounding temperature (Timoshenko, 1935). Achieving a neat function and easily built, bistable elastic structure have since then popped up in our environment and are even used as toys (jumping poppers, see Lapp, 2008). Nowadays, if mechanical bistable switches tend to be replaced in various devices by electronic switches, snapping is perceived as a means to design responsive surfaces with applications to on-demand drug delivery, optical surface properties modification, or on-command frictional changes (Holmes and Crosby, 2007). Recently, it has also been increasingly realized that this elastic elastibility was also exploited in Nature in the most surprising contexts. Plants for example, though not known for their rapidity, can exploit snapping instabilities to defeat the physiological barrier on their movement duration. This is how the Venus flytrap can catch a fly in a tenth of a second (Forterre *et al.*, 2005). Other examples include the fast suction of small underwater plants (Vincent *et al.*, 2011) or the snapping of malaria infected red blood

cells propelling parasites in the body (Abkarian *et al.*, 2011). All these examples differ in their triggering mechanisms, but they all involve a snapping instability including fast movements and curvature reversals that are a consequence of the sudden release of stored elastic energy and its transfer into kinetic energy.
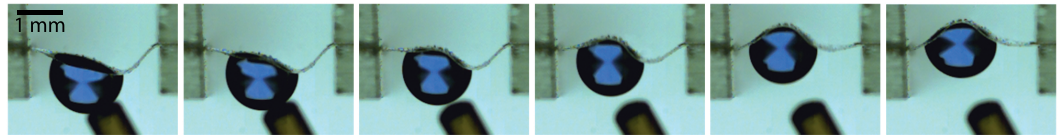

FIG. 3.7 - **Snapping against gravity.** Using a PTFE coated needle, a drop is gently deposited under a downward buckled PDMS strip. Within a few milliseconds, capillary forces induce a snap-through elastic instability of the strip which jumps to the upward buckled state. Note that in this setup surface tension overcomes both elastic forces and gravity. The time interval between each snapshot is 5 ms (Fargette *et al.*, 2014).

With Aurélie Fargette and Sébastien Neukirch we got interested into this problem and wanted to know if (and how) capillary forces could induce snap-through instabilities. For so, we designed an experiment where a drop deposited onto (or hung below) a buckled elastomeric strip could trigger the strip snapping. This is illustrated Fig. 3.7, where a drop is released from a hydrophobic needle onto the lower side of a PDMS strip. Within a few milliseconds, elastocapillary snapping occurs: capillary forces overcome elastic forces and, as a byproduct, gravity as well thereby clearing the weight of the drop as the root cause for this phenomenon. So as to accustom with the mechanics of snapping, we started by investigating a dry version of the setup. By means of minute force measurements performed with a sensor using capacitive deflection measurement (Femtotools FT-S270, see Sun *et al.*, 2005) and a nano-positioner (SmarAct SLC-1730) we monitored the force-deflection curve during a point-loading experiment on a PDMS strip, see Fig. 3.8. Initially the sensor exerts no force, but there is already a deflection because of the buckled shape of the strip. While the sensor tip pushes down the arch, the exerted force increases up to $F^\star$, at which point a negative stiffness regime appears: as the deformation gets larger the force reduces, up to the tipping point of snapping. Note that in this regime, the observed states are no more symmetric. Negative stiffness is quite common in structural mechanics (Thompson, 1982), but we can shed some further light over the whole behaviour of the system by computing the paths followed by equilibria of an Elastica subject to the same forces and constraints as in the experiments. These computations, also presented Fig. 3.8, reveal a set of bifurcation branches corresponding to symmetric and asymmetric states. Interestingly, it appears that the symmetric path followed initially suddenly becomes unstable at a point where an asymmetric branch emerges. In our displacement controlled experiment, the latter is a stable path that corresponds to the negative-stiffness part observed earlier. Note that it is not necessarily a good idea to apply the indentation right at the middle point of the beam if one wishes to induce snapping at minimal cost. Indeed, there is a sharp dependence of the critical force F^* with the horizontal position of the point load, as illustrated in inset.
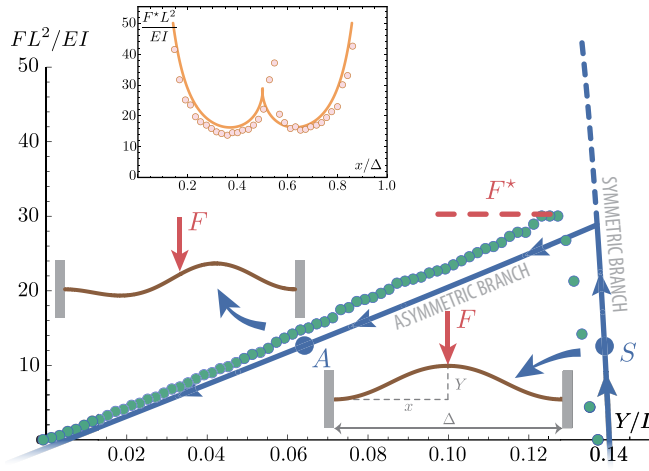
FIG. 3.8 – **Dry snapping experiment.** An elastic strip, clamped at both ends with fixed compression $\Delta = 0.95\,L$ is indented vertically at $x/\Delta = 1/2$. The bifurcation diagram (theory: blue curve, experiments: filled circles) is made up of a symmetric and an asymmetric branch connecting at $F = F^\star$ (experimentally measured $F^\star = 55\;\mu$N). Inset: Evolution of the snapping threshold $F^\star$ as a function of the indentation position x, evidencing two preferential positions where the threshold is minimal: $x/\Delta \simeq 0.37$ and 0.63.

Another important point to emphasize is that at the verge of instability, the force felt by the sensor vanishes. This means that no additional external force is required to observe the actual shape of the Elastica, which is therefore an (admittedly unstable) equilibrium state. In other words, **at the point of instability, the shape of the Elastica is exactly that of the second mode of buckling**.

Now back to elastocapillary snapping, we performed a series of experiments with a drop hanging under a downwards-buckled PDMS strip, see Fig. 3.9(c). The parameters of the experiment are the total weight F of the drop and the abscissa x_M of the middle point of the wet region of the beam. The experiments reveal that snapping only occurs for specific values of F and x_M, as summarized in the phase diagram of Fig. 3.9(b). For small enough drops (*i.e.* small F), capillary forces exceed self-weight (a drop deposited under a rigid surface is stable if small enough) but are not powerful enough to overcome elastic forces. Why? Actually the combined action of Laplace and meniscus forces can be seen as two opposite effective bending moments. In the case of small drops, the lever arm of these effective bending moments is simply not large enough. In other words, this points to the wet length as a key factor determining the behavior of elastocapillary systems (see also §3.4). Consequently the system stays in the downward configuration. For moderate drops (with larger wet lengths) we see in Fig. 3.9(b) that provided the location of the drop is carefully chosen (that is, not perfectly centered) snapping occurs, resulting in a final state where the strip is bent upward: in this case capillary forces overcome both weight and elastic forces. For large drops capillarity still defeats elasticity but self-
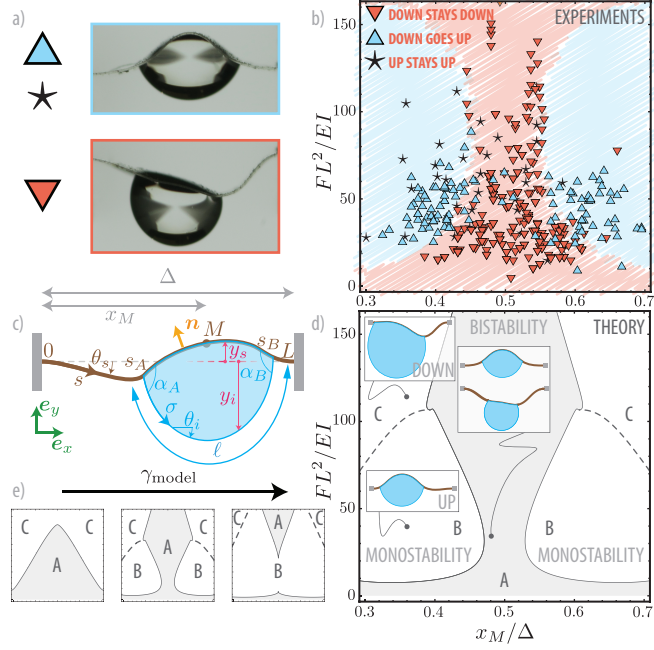
FIG. 3.9 - **Phase diagram for elastocapillary snapping**. A drop is hung under a strip and the conditions for snapping to occur are investigated. (a) Possible final states of the system. (b) Experimental phase diagram plotted in the (x_M, F) plane. Triangles (respectively $\star$) correspond to experiments where the drop is deposited on an initially downward (resp. upward) buckled strip. (c) Model notations. (d) Theoretical phase diagram showing bistable A and monostable B and C regions. Note that here FL^2/EI corresponds to $12\rho\mathcal{A}g/Eh^3$. (e) Evolution of the theoretical phase diagram as the surface tension used in the model γ_{model} takes the values $0.38\,\gamma$, $0.67\,\gamma$, and $0.96\,\gamma$ (from left to right).

weight is this time too large and the system stays in the downward configuration. To understand the different regions of the (x_M, F) phase diagram we numerically computed the equilibrium and stability of the drop/strip system using the methods presented earlier and the notations of Fig. 3.9. More specifically, we started by denoting the bending energy of the strip and gravity potential energy of the drop as:

$$E_{\mathrm{bend}} + E_{\mathrm{hydro}} = \frac{Eh^3}{24} \int_0^L \left[\theta'_{\mathrm{s}}(s)\right]^2 \mathrm{d}s + \rho g \iint_{\mathcal{A}} y\,\mathrm{d}\mathcal{A}, \qquad (3.19)$$

where $\mathcal{A} = \int_0^\ell y_{\mathrm{i}}(\sigma)\, x'_{\mathrm{i}}(\sigma)\, \mathrm{d}\sigma - \int_{s_A}^{s_B} y_{\mathrm{s}}(s)\, x'_{\mathrm{s}}(s)\, \mathrm{d}s$ is the area between the strip and the liquid-air interface. The energy per unit area of solid-liquid (respectively solid-air, and liquid-air) interface is noted $\gamma_{\ell s}$ (resp. γ_{sv} and γ). The total interface energy is then:

$$E_{\mathrm{surf}} = (s_B - s_A)\gamma_{\ell s} + \left[L - (s_B - s_A)\right]\gamma_{sv} + \gamma\,\ell \qquad (3.20)$$

We minimize the total potential energy $U = E_{\mathrm{bend}} + E_{\mathrm{hydro}} + E_{\mathrm{surf}}$ under the constraints of inextensibility $\boldsymbol{r}'_{\mathrm{s}}(s) = \boldsymbol{t}_{\mathrm{s}}$ (where $\boldsymbol{t}_{\mathrm{s}}$ is the unit tangent and $\boldsymbol{r}_{\mathrm{s}}(s) = (x_{\mathrm{s}}(s), y_{\mathrm{s}}(s))$), constant

area $\mathcal{A}$, and matching conditions $\boldsymbol{r}_s(s_A) = \boldsymbol{r}_i(0)$ and $\boldsymbol{r}_s(s_B) = \boldsymbol{r}_i(\ell)$, with $\boldsymbol{r}_i(\sigma)$ parametrizing the interface. This constrained minimization problem is solved by considering the following Lagrangian functional:

$$\mathcal{L}\left[\boldsymbol{r}_s(s), \theta_s(s), s_A, s_B, \boldsymbol{r}_i(\sigma), \theta_i(\sigma), \ell\right] = U - \boldsymbol{\mu} \cdot \boldsymbol{\psi} \tag{3.21}$$

where the vector $\boldsymbol{\psi}$ includes all the constraints and $\boldsymbol{\mu}$ is the vector of associated Lagrange multipliers. Classical minimization and continuation techniques are then used to track equilibrium states along branches in bifurcation diagrams, and the stability is assessed by computing the linearized dynamics about the equilibrium solution. The corresponding results are shown in Fig. 3.9(d). There, a continuous curve, later referred to as the instability curve, corresponds to loss of the stability of an equilibrium configuration. By contrast the dashed curve corresponds to a smooth transition from downward buckled states $(y_M < 0)$ to upward buckled states $(y_M > 0)$. These two curves divide the (x_M, F) plane in three regions. In region A, which lies below the instability curve, downward and upward buckled configurations are both found to be stable. As the crossing of the instability curve is associated with the loss of stability of one of the configurations, in the two regions above the instability curve there is only one stable configuration: upward for region B, below the dashed curve, and downward for region C, above the dashed curve. Note that the shape of the instability curve and hence the topology of the phase diagram is altered by changes in the value of surface tension, as shown in Fig. 3.9(e). These numerical results shed light on experimental findings: in the bistable region A, a drop deposited under a downward buckled strip leads to a downward final state unless the perturbation created during the deposition is too large and the system jumps to an upward final state, whereas in the monostable region B the final state is always an upward configuration. As a cross-check we have experimentally hung drops under upward buckled strips and found that in regions A and B the system stays in the upward configuration, thereby confirming the bi-stability of region A, see markers $\star$ in Fig. 3.9(b).

FIG. 3.10 – **Condensation-induced snapping.** The experiment approximately lasts three minutes.

Elastocapillary snapping opens interesting perspectives, with for example the possibility for its remote triggering. Indeed, when an elastomeric strip with a hydrophilic coating on one side is placed in a steam flow, water droplets start nucleating on this hydrophilic side. Past nucleation, coalescence events occur and eventually induce snapping, see Fig. 3.10. This phenomenon could be used to build moisture sensors that would snap once ambient humidity has reached a given threshold.
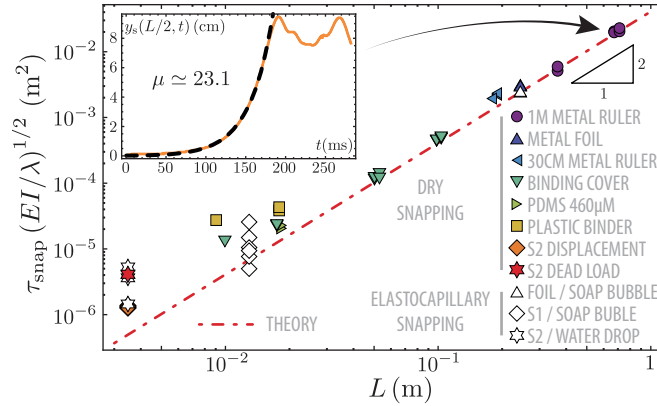
FIG. 3.11 – **Snapping dynamics.** Typical time τ_{snap} for snapping in different setups. The dashed line is the theoretical prediction for 'dry' snapping $\tau_{\text{snap}} = (L^2/24)\sqrt{\lambda/\text{EI}}$.

Now that the conditions for snapping have been outlined, we may wonder about the time needed to switch from one state to another: How fast is a snap? Curiously this question has hardly been asked in the literature, though dimensionwise there are not much alternatives and the duration should scale with $T = L^2\sqrt{\lambda/EI}$, λ being the lineic mass of the beam. To verify this we recorded experimentally the shape of the beam as it leaves the unstable equilibrium. We found that the vertical position of the beam mid-point was well captured with the law $y_{\text{s}}(L/2,t) = y_0 + y_1 e^{\mu t}$, where μ is the growth rate of the instability. From this growth rate μ we defined a snapping time $\tau_{\text{snap}} = 1/\mu$ and plotted τ_{snap} as a function of the length L of the beam. Interestingly, as said earlier the shape of the beam as it starts to snap is the second mode of buckling of an Elastica. The growth rate μ should therefore be the growth rate of this mode. We verified this and computed numerically μ for different Δ. The dependence on the confinement Δ is quite weak so that the approximate theoretical prediction $\tau_{\text{snap}} = T/24$ holds for the range of confinements investigated here. Experiments performed with various materials and confinements, e.g. 'dry' setups involving $L = 0.7$ m metal beams, showed that, apart from a deviation at small lengths attributed to viscous effects in the strip, theory agrees nicely with experiments, see Fig. 3.11. Additional experiments with thin PDMS strips, but also with soap bubbles actuating $L = 0.25$ m metal foil strips, confirmed that the snapping time appears to be the same for 'dry' and 'wet' snapping.

As in adhesive film separation (Gay and Leibler, 1999) or in the pull-out of a soft object from a liquid bath (section §3.2, Rivetti and Antkowiak, 2013), the elastic energy stored in the system before the instability is suddenly released in the form of kinetic energy and is mainly lost, though part of it can allows to switch to another stable state and potentially lift the liquid drop. Note that here the elastocapillary dynamics is mainly driven by elastic forces and that fluid forces and fluid inertia only play a minor role: capillarity is driving the system towards instability but elasticity is ruling the subsequent dynamics. Finally, the typical scalings of surface forces makes elastocapillary snapping a good candidate to

miniaturization and its use as a micro-actuator might be envisaged.

3.4 Elastocapillary dynamics: instant fabrication of 3D structures

In the previous examples, the strip geometry, forces at play and resulting deformation/dynamics were essentially two-dimensional. We now turn to the complex 3D deformations imparted to a thin plate by an impacting drop, see Fig. 3.12. There, we
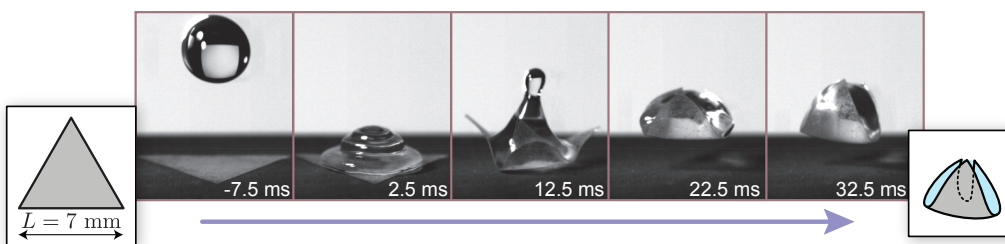

FIG. 3.12 – **Instant capillary origami,** obtained with a water droplet of radius $R = 1.55$ mm impacting a thin triangular polymer sheet with thickness $h = 55$ μm at velocity $U = 0.53$ m·s^{-1}. This time sequence reveals that encapsulation results from the interplay between the motion of fluid interface by capillary forces, and the large, dynamic deformations of the film (Antkowiak *et al.*, 2011).

observe a drop impacting at its center a triangular target of width 7 mm with velocity $U = 0.53$ m·s^{-1}. Just after impact, the drop spreads out over the target up to a maximal extent where inertia is balanced by the restoring action of capillarity. Next, surface tension drives a flow towards the center of the drop. This causes the rebound of the drop, and of the elastic film that sticks to it. While in free fall above the ground, the elastic sheet quickly wraps the drop. An elasto-capillary bundle with a tetrahedral shape is formed, and falls down to the ground. The whole sequence takes place in 40 ms, which is the typical duration of an hydrophobic rebound (Richard *et al.*, 2002). Such surface-tension-driven origami formation has actually a long history, rooted in the microfabrication of 3D hinged structures. Indeed, lithography techniques typically allow to manufacture planar objects but fail to produce 3D structures. Since the 90s however, it has been realised that surface tension (typically of a solder first electrodeposited, and then reheated) could help lift the parts of a planar articulated object to build various fans, lenses, Fabry-Pérot etalons, inductors etc. (see e.g. Gracias *et al.*, 2002; Syms *et al.*, 2003). Under the thrust of José Bico and Benoît Roman at ESPCI, this type of phenomena have been translated into the interaction between elastic sheets and liquid surfaces to form the broad field of elastocapillarity, with its iconic capillary origami (Py *et al.*, 2007). Such a capillary origami results from the interaction of a single flexible sheet and a liquid drop sitting on it. The hinges are now replaced by folds developing on the thin sheet. Upon drop

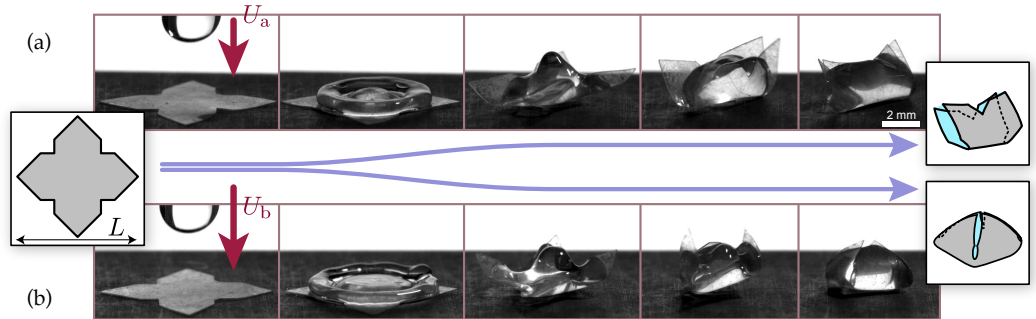evaporation, the structure self-closes, i.e. full encapsulation occurs.

FIG. 3.13 – **Shape selection.** A flower-shaped target reveals the possibility of pattern selection based on impact velocity U. Radius of the drop is R = 1.55 mm in both experiments, target width is L = 10 mm and $U_b > U_a$. *(a)* For low impact velocity, U_a = 0.68 m·s^{-1}, a cylindrical bundle is formed, having two-fold symmetry. *(b)* At higher velocity, U_b = 0.92 m·s^{-1}, the drop spreads more widely and almost wets the entire surface of the film; a pyramidal wrap is formed, having four-fold symmetry.

Interestingly the use of drop impact, more than just speeding up elastocapillary wrapping (over 5 decades – for wrapping time now scales with drop rebound rather than drop evaporation), also allows for final shape control. A typical illustration of this shape selection mechanism is presented in Fig. 3.13. In this experiment, a drop impacts a small flower-shaped film at its center. For a fixed drop radius, different folding scenarios can be observed depending on the impact velocity. At low impact speed, spreading of the drop is limited, and the final pattern is the cylindrical folding of figure 3.13a. At higher speeds, the drop quickly embraces the entire surface of the sheet, and upon retraction a pyramidal wrap is obtained, see figure 3.13b. Different instant origamis can thus be obtained by simply tuning the velocity of impact.

The phenomenon of dynamic elasto-capillary encapsulation can be understood with a simpler, 2D geometry where bistability of the final shape now arises thanks to a gravitational barrier rather than complicated folds, creases and geometric frustration effects proper to plate elasticity. We therefore carried out a series of systematic experiments using as a target a long and narrow rectangular strip of width $w = 2$ mm, length $L = 5$ cm and such that $L/\ell_{eg} = 14.3$, with the elasto-gravity length $\ell_{eg} = (B/(\mu g))^{1/3} \simeq 3.5$ mm above which gravity bends a cantilever beam has been introduced earlier (see §3.2). The 2D setting is sketched in figure 3.14a. Remarkably, shape selection can still be observed in 2D: the phase diagram in figure 3.14b reveals a competition between wrapped and non-wrapped final configurations. This diagram was obtained by systematically varying the distance x from the point of impact to the end of the strip, and the impact velocity U. For the purpose of plotting, the position of impact x was measured in units of ℓ_{eg}, and U in units of the capillary velocity $(\gamma/\rho R)^{1/2}$: the resulting dimensionless velocity is the square root of the Weber number $We = \rho U^2 R/\gamma$. In our experiments, the Weber number

varies from 0.21 to 15, which is the typical value at which the inkjet technology operates.
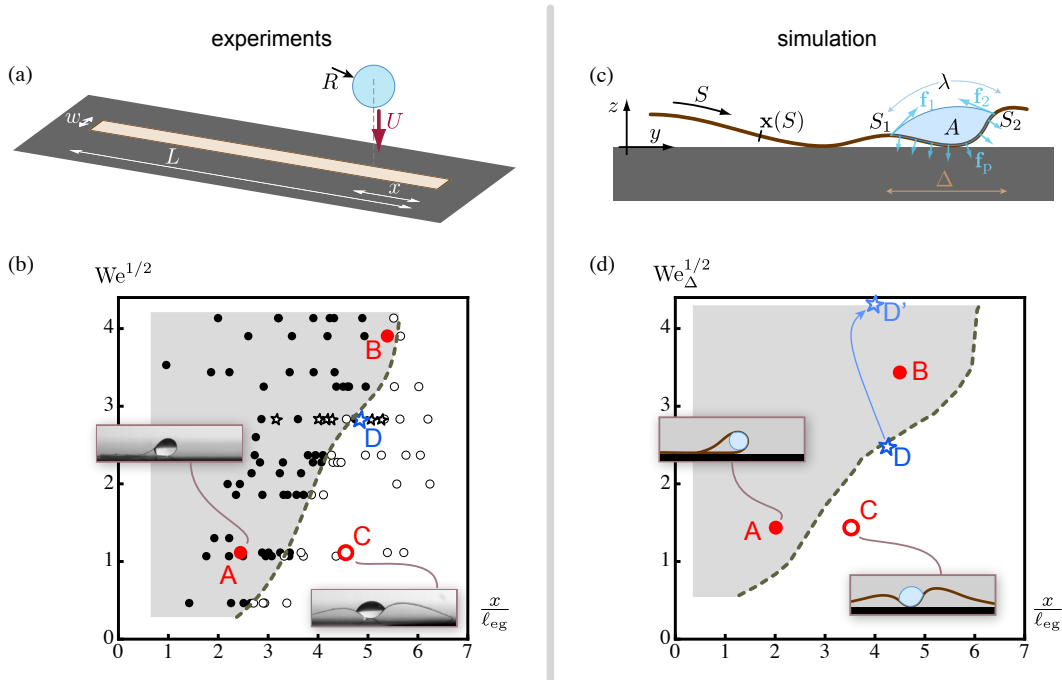
FIG. 3.14 – **Comparison between experiments and model on 2D encapsulation.** Comparison of experiments (a,b) and simulations (c,d) in a 2D geometry. (a) In these experiments, a drop impacts a long, thin polymer strip laying down on a substrate, at a variable distance x from its end, and with variable impact velocity U. Strip dimensions are L = 5 cm and w = 2 mm, and drop radius is R = 1.55 mm. (b) Phase diagram showing the outcome of the experiment: non-encapsulated drop (open circles), encapsulated drop (filled dots), or encapsulated drop with the help of a secondary drop obtained by pinch-off (stars). (c) Numerical model of a 2D dynamic Elastica coupled with a quasi-static, incompressible fluid with surface tension. (d) Phase diagram for the Elastica model. In (b,d), typical final shapes are shown in inset. During the simulation run labelled D in (d), the impact parameters are changed to account for the capture of a secondary drop, as shown by the light blue arrow.

Qualitatively, the process of encapsulation requires passing a gravitational energy barrier with the aid of the initial kinetic energy. The outcome of a particular experiment reflects the efficiency of this energy transfer. Indeed, since both L and R are larger than ℓ_{ec} (with $\ell_{ec} = (B/\gamma)^{1/2} \simeq 0.55$ mm being the elastocapillary length above which capillary forces can make slender objects buckle), the strip is flexible enough to bend around the drop and the energy is always minimum in the encapsulated state. However, for drops that are too slow, or impact too far from the edge, the barrier associated with lifting up the strip prevents the system from reaching this global minimum. When the drop is deposited near the end (small x), encapsulation involves lifting a short segment of the strip, making

the barrier lower. For small enough values of x, encapsulation can even be observed after nearly quasi-static deposition of the drop. For larger values of x, however, the barrier is higher and some amount of kinetic energy is required. This explains the existence of a threshold for the velocity U allowing encapsulation, and the increase of this threshold with x. This qualitative reasoning is consistent with the orientation of the boundary obtained in the experimental diagram, see figure 3.14b.

Before turning to the model, let's note that during the fast initial spreading of the drop, part of the incident kinetic energy is quickly and irreversibly transferred into surface energy. Irreversibility is here a consequence of contact line pinning: due to the roughness of the substrate, the contact line never recedes. It remains anchored to its maximal extent in all our experiments. This maximal extent, denoted Δ, is directly set by the impact parameters. It is a key mechanical quantity that determines how the capillary forces are distributed, and how efficiently they bend the film during the subsequent folding. Δ was measured in a separate series of experiments using the same film. We found that, in our range of parameters, spreading is well described by the empirical law $\frac{\Delta(U)-\Delta_0}{2\,R} = 0.32\,\mathrm{We}^{1/2}$. The parameter $\Delta_0 = \Delta(U=0)$ represents the amount of spreading for quasi-static deposition, as we are in partial wetting conditions. Note that the exponent $1/2$ is consistent with a conversion of kinetic energy $\sim \rho\,U^2\,R^3$ into surface energy $\sim \gamma\,\Delta^2$.

With the aim to predict encapsulation, we consider a mechanical model for the slow folding dynamics of the strip following the initial drop spreading. In this model, the two contact lines are anchored and separated by a prescribed curvilinear distance Δ. The value of Δ captures the initial transfer of kinetic into surface energy, and the rest of the motion is driven solely by capillary forces. The dynamics of the strip is governed by the following potential energy:

$$\mathcal{U} = \int_0^L \left[\frac{B}{2}\,|\mathbf{x}''(S,t)|^2 + \mu\,g\,\mathbf{x}(S,t)\cdot\mathbf{e}_z \right] \mathrm{d}S + \gamma\,\lambda(\mathbf{x}(\cdot,t),A,x,\Delta) \qquad (3.22)$$

and kinetic energy:

$$\mathcal{T} = \frac{1}{2}\int_0^L \mu\,|\dot{\mathbf{x}}(S,t)|^2\,\mathrm{d}S, \qquad (3.23)$$

Our numerical code integrates in time the equations of motion obtained by applying Lagrangian mechanics to our Lagrangian $\mathcal{L} = \mathcal{T} - \mathcal{U}$. In deriving these equations, we also consider the inextensibility constraint $|\mathbf{x}'| = 1$ and the presence of an impenetrable ground $\mathbf{x}\cdot\mathbf{e}_z \geq 0$. Fluid incompressibility is used during the reconstruction of the drop perimeter $\lambda(\mathbf{x}(\cdot,t),A,x,\Delta)$. The resulting equations of motion are the classical equations for the dynamics of a 2D Elastica subjected to gravity forces, to frictionless reaction from the ground in the event of contact, and to capillary forces. The capillary forces tend to make the potential energy $\mathcal{U}$ lower. They do so by bending the strip around the drop, thereby reducing the interfacial length λ while preserving the imposed area A. Note that in the expression for the kinetic energy only the elastic part has been considered ; fluid motions such as capillary waves are neglected in the model, and the drop is really a dummy drop; just a circular shell exerting Laplace pressure and point meniscus forces but unable to sustain motion (see Antkowiak *et al.*, 2011, for further details).

The numerical phase diagram in figure 3.14d has been obtained by varying the impact parameters systematically in a series of simulation runs. For the purpose of comparison with the experiments, the impact parameter Δ is then converted into an equivalent Weber number using our empirical law $\mathrm{We}_\Delta^{1/2} := (\Delta(U) - \Delta_0)/(0.64R)$ capturing the fast initial spreading of the drop. As revealed by the phase diagram in figure 3.14d, the model successfully explains the selection of the final shape by the impact parameters. The essential features of the experimental diagram are reproduced. Any value of the position of the center of impact x is associated with a critical value of the Weber number. This corresponds to a minimal value of the velocity U (or the spreading Δ) for encapsulation to occur. In addition, this critical value of the Weber number is an increasing function of x. Note that though the numerical model is based on simplifying approximations such as neglecting the weight and inertia of the drop, as well as three dimensional effects, capillary waves and depinning of the contact line, there is a close agreement on the boundaries between the encapsulated and non-encapsulated regions. The simulation parameters are set directly from their experimental values and there is no adjustable parameter.

The model not only predicts the final shape of the strip but also all the details of the dynamic sequence leading to encapsulation are captured with remarkable accuracy. For a small subset of the experiments however, confined to a limited region of the experimental phase diagram and labelled by stars in figure 3.14b, encapsulation takes a special route. In this region, the final state is not always reproducible even for fixed impact parameters. In addition, encapsulation can be observed for anomalously large values of x: the two stars to the right of the point D in figure 3.14b clearly stand out to the right of the boundary. This surprising behaviour can be explained by looking at the time sequence in figure 3.15a. Shortly after the initial spreading, a vertical jet is formed and a secondary drop detaches. Under the action of gravity, it accelerates downwards, catches up with the falling capillary bundle, and coalesces. In some experiments, such as that labelled D in the figure, the bouncing drop lands on the edge of the main drop and coalesces, thereby increasing the wet length Δ. This induces a redistribution of the capillary forces that substantially modifies the subsequent folding dynamics. Since the ejection of a secondary drop is ruled by the Weber number, this view is consistent with the observation that anomalous encapsulation events are all observed when the Weber number is close to a particular value, $\mathrm{We}^{1/2} \approx 2.8$. When the simulation is run as earlier, ignoring the secondary drop, encapsulation is not correctly predicted, as shown in figure 3.15c. The role of the secondary drop is captured by a simple extension of the model. From the experimental movies, we measure the time of ejection of the secondary drop and the position of the contact line after coalescence. This yields virtual impact parameters, labelled D$'$ in figure 3.14d, which are indeed well inside the region of encapsulation. We run again the simulation, now updating the position of the contact line at the time of coalescence. As shown in figure 3.15b, the key role of the secondary drop on the final pattern is accurately captured. Encapsulation is correctly predicted and comparison with the experiments reveals an excellent, frame by frame agreement.

To conclude, let's remark that as in the case of elastocapillary snapping considered earlier in §3.3, the outcome of the dynamical origami essentially relies on the strip bistability.
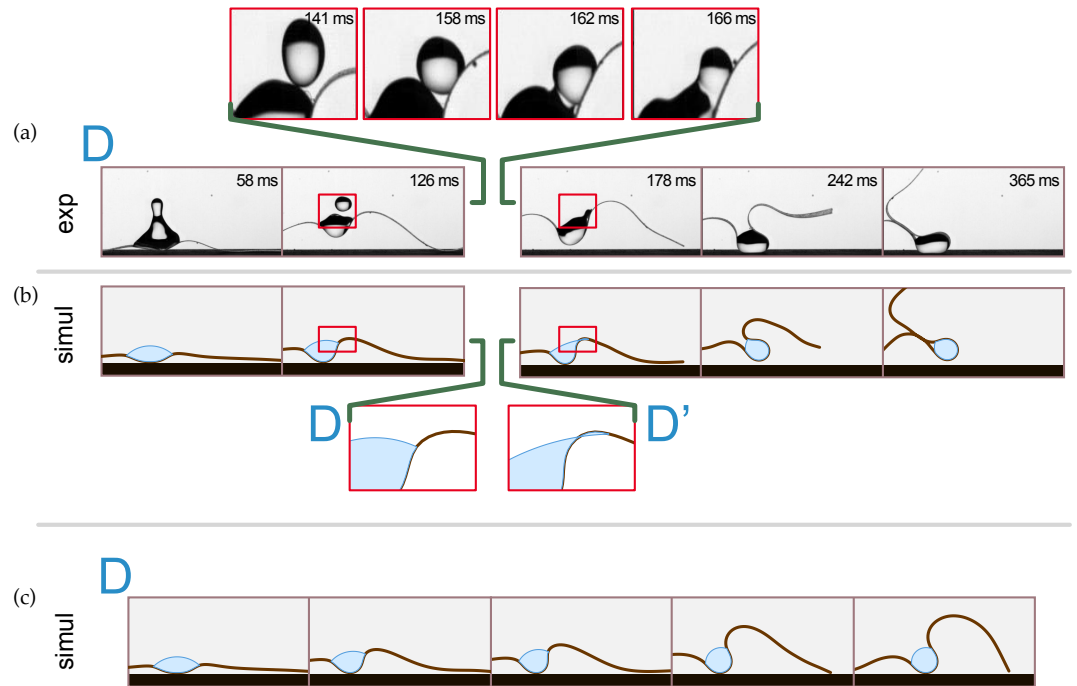
FIG. 3.15 – **Encapsulation aided by a topology change of the drop.** (a) In the experiments a secondary drop appears transiently by pinch-off and coalescence when $We^{\frac{1}{2}} \approx 2.8$. This detachment leads to encapsulation in a region where it would otherwise not be possible: the impact parameters for this experiment are denoted by the star labelled D, located to the right of the boundary in the phase diagram of figure 3.14b. (b) This transient topology change is accounted for by extending the footprint Δ of the drop in the middle of the simulation (inset D'), by an amount measured from the experimental frames. As a result, simulation correctly predicts encapsulation, and matches the experimental movie frame by frame. (c) When this footprint Δ is left unchanged, simulation fails to predict encapsulation.

Further, the thin sheet dynamics is here critical in the selection of the final folded state. The importance of kinetic energy in this problem is interesting. Indeed, at small scales, viscosity and capillarity are often considered as dominant, and inertia negligible. The impact of a drop is an exception to this rule: kinetic energy, when initially stored in the form of a rigid-body mode of translation, cannot be dissipated by viscosity. This energy ends up in selecting the final shape among competing equilibria. Note also that in the 2D setting considered, multistability arises from gravity. The dynamical shape selection uncovered here nonetheless works also at smaller scales, where gravity becomes unimportant. Indeed, there are other sources of multistability, such as nonlinear elasticity of thin films or the follower character of capillary forces. As a matter of fact, numerical experiments confirmed the persistence of shape selection in the absence of gravity. The robustness of

the selection mechanism opens up the perspective of scaling down the experiment to the size of an inkjet drop.

4 | Capillary Spools

In this last chapter we introduce a new type of material inspired from the spider capture silk and displaying a very strange behaviour: while it behaves as a regular solid in extension, its mechanical response totally switches in compression to become liquid-like. In what follows, we disentangle the physics underpinning this very particular mechanical response and trace back its origin to the formation of elastocapillary spools within the (glue) droplets decorating the fibre.

4.1 The spider capture silk

Back in 2012 we got interested with Sébastien Neukirch on the possible occurrences and outcomes of elastocapillary phenomena in the realm of biology. We stumbled on a 25 years old paper reporting on the appearance of balling of core thread fibre into the glue droplets decorating spider capture silk (Vollrath and Edmonds, 1989). Intrigued by this observation, we contacted Prof. Fritz Vollrath from the Oxford Silk Group at the Department of Zoology in Oxford University and have started a continuous and fruitful collaboration since then.

▷ **Spider web and spider silks.** Spiders are many, and so are their web architectures: regular, aerial, three-dimensional, horizontal, funnel-like, dry or wet, etc. The object of our study is a particular fibre found in the orb web spun by spiders like the garden spider Araneus Diadematus or the large (and impressive) Nephila Edulis living in New Guinea, and pictured in inset (Foelix, 2010). A typical web consists in a neatly arranged set of fibres, some forming the frame, some radiating from the centre, some other spiraling around the whole web. It appears that each of these distinctive architectural elements has different mechanical properties, and for good reasons: each type of fibre is spun by a different gland.
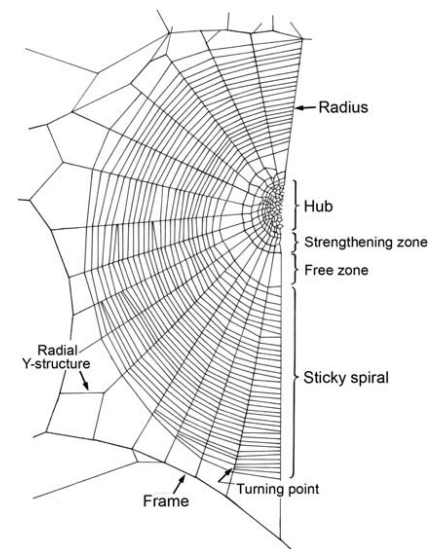
Modern spiders can have up to 7 different silk glands, each producing a silk designed for a proper function: the major ampullate gland produces a thick and stiff silk that will form the backbone of the web (radial spokes and frame), the flagelliform gland gives the core fibres of the capture spiral, others provide dedicated silks for cementing joints, or building the egg sac, and so on (Vollrath, 1992). The capture thread is the sticky thread spiraling over the web, and is obviously an essential element in the trap. The core fibre of this spiraling capture silk is non sticky by itself; spiders have evolved a specific gland producing an aqueous glue (a liquid silk really) sheating the core thread and endowing the fibre – and hence the web – with adhesion. Note here that capture silk is in essence a hybrid material composed of liquid (glue droplets) and solid (core thread).

Note: Orb-weaving spiders include modern ecribellate spiders and ancestral cribellate spiders. A key distinction between these species is the technology of capture silk. While ecribellate (discussed here) spin smooth fibres decorated with glue droplets, the cribellate's capture silk is totally dry and presents puffy structures constituted of thousands of nanofibrils, which provide a van der Waals type adhesion (Blackledge et al., 2009). Note that fog or humidity are detrimental for the latter, and induce a dramatic loss of adhesion (Elettro et al., 2015a)
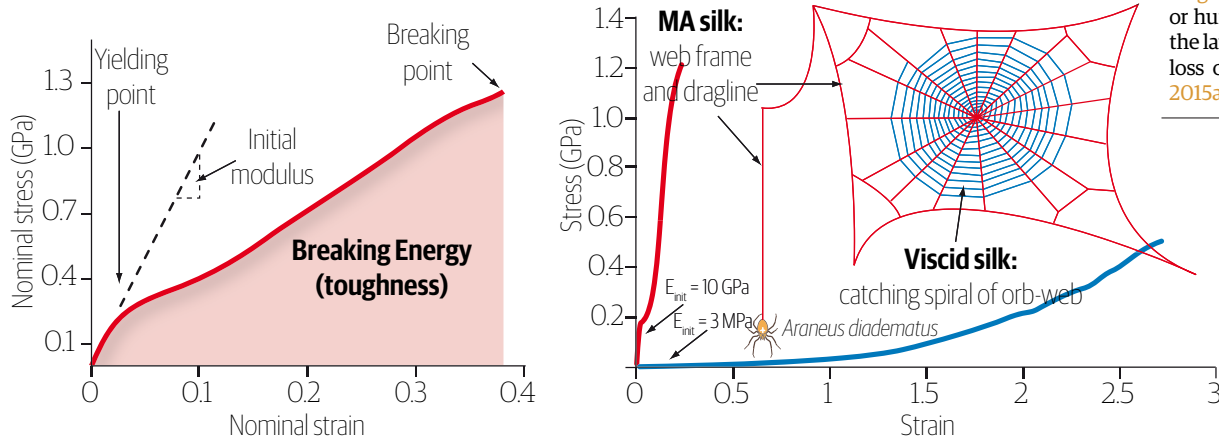

FIG. 4.1 - **Silk mechanics**. Left: sketch of a typical strain-stress response of silk, with key features (Young's modulus or stiffness, strength or breaking stress, and toughness) highlighted. Right: mechanical response of dragline silk (produced by the Major Ampullate gland, or MA) and of the capture (or viscid) silk. Both silks are neither particularly stiff nor extensible, but exhibit large toughnesses of $O(150\,\text{MJ/m}^3)$ (from Omenetto and Kaplan, 2010).

▷ **Silk mechanical response.** Orb-webs are particularly efficient aerial traps able to glue, cushion and secure insects weighing more than the whole web, and this impressive feat can be appreciated through its mechanical response. If neither the strength nor the maximal elongation are particularly remarkable with respect to those of man made fibres (see Fig. 4.1 and e.g. Denny, 1976; Omenetto and Kaplan, 2010), the combination of the two yields a truly massive toughness outperforming Kevlar or steel fibres. The substantial energy needed to rupture the threads prevents insects – even large – flying at full throttle to tear the web. Added to the fact that it can dissipate substantial amounts of energy with little volume (and hence prevent the trampoline fashion rebound of the incipient prey), the silk fibre therefore appears as a unique material to make deadly traps with.

Note: The mechanical properties of spider silk and its intrinsic biocompatibility makes it a material of choice for sutures and reconstructive surgery, for it can serve as a scaffold for bone and ligament repair. The optical clarity of the material also makes it a good candidate for the design of optical fibres with new functional features (Omenetto and Kaplan, 2010).
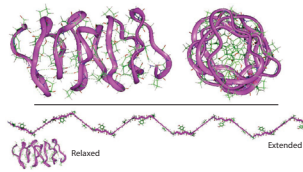
All the particular extensional properties of spider silk, and of capture silk especially, can be understood from processes at the molecular level. Becker *et al.*, (2003) have for example revealed that the flagelliform protein has a spring-like conformation and can be greatly extended (i.e. uncoiled) during stretching events (see inset). Capture silk, as a material made from such coils should therefore inherit the elasticity of its molecular constituents. Further, looking closely at force spectroscopy measurements it appears that rupture peaks routinely occur during the stretching of a flagelliform silk sample. These rupture peaks (sudden decrease in the mechanical response) are in fact attributed to sporadic tears of sacrificial bonds, which in turn contribute to the high fibre toughness. Similarly the supercontraction of radial silk in a highly humid environment (Work, 1977) can equally be understood on molecular grounds. Conversely, while the compressional behaviour of the capture silk is also very surprising, it stems from a really different – mesoscopic – origin, as we show next.

4.2   A liquid-like fibre
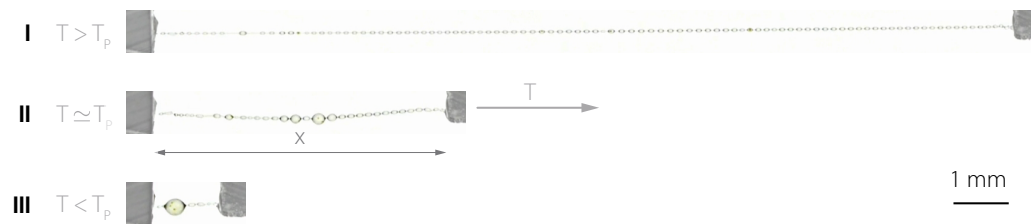
FIG. 4.2 - **A liquid-like fibre.** Whether stretched or relaxed, the typical capture silk thread of an araneid orb spider (here *Nephila edulis*) remains taut. Force monitoring reveals that when subjected to large tension T the fibre behaves like a spring (I). As T is decreased, a force plateau $T \simeq T_P$ is reached, along which the thread adopts a wide range of lengths, just as soap films do (II). At lower tensions, $T < T_P$, the thread is totally contracted (III).

While the extensional properties of capture silk have been analysed and mapped for years, far less studies have investigated its behaviour in compression, though truly unusual it is. Figure 4.2 reports on the singular response of capture silk in compression: unlike any solid/elastic fibre that would sag or buckle (and leave its original axis), capture silk remains taut and self-adapts to compression, as if it was telescopic. It is not uncommon in the experiments to make capture silk contract to up to 95% of its original web length without any noticeable sagging. This behaviour is actually much reminiscent of the response of liquid films to compression events. Indeed, liquid films do not buckle upon squeezing, but rather self-adapt. Of course this shape adaptation for liquids is made possible by the presence of a constant tension at the liquid surface (Boys, 1890; Maxwell, 1876). Forms and forces are intimately linked, and the liquid-like nature of capture silk in compression

already perceived in the photographs of Fig. 4.2 will be borne out by accurate force measurements in the following.

4.3 Geometry and mechanics

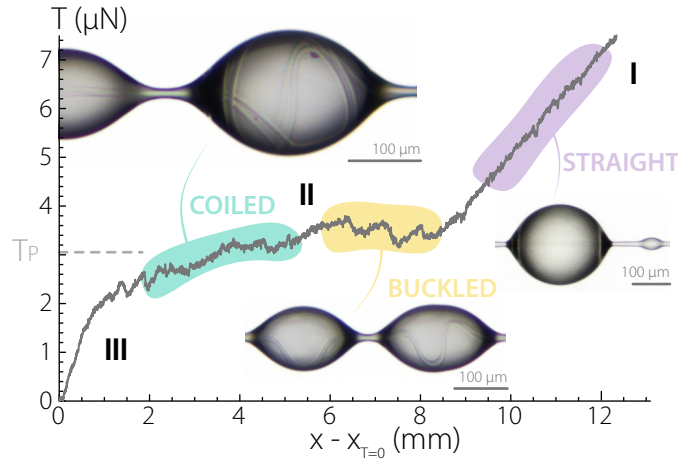FIG. 4.3 – **Shape-induced functionalization.** Quasi-static force measurements on spider capture threads combined with microscopic observations reveal that the core filament coils into the droplets ($\sim$ 250-300 μm wide) along a force plateau $T \sim T_\mathrm{P}$ (liquid-like response). For larger forces $T > T_\mathrm{P}$, the fibre straightens and a solid-like behaviour is recovered. The particular shape of this force-extension curve can be attributed to a shape-induced functionalization of the fibre by the glue droplets.

During the PhD thesis of Hervé Elettro, we looked in detail at the physics underpinning this liquid wire, and found that the behaviour of this hybrid material made of solid and liquid was rooted in geometry and mechanics (Elettro *et al.*, 2016). Actually, the spectacular macroscopic properties of hybrids often originate in a physical effect that occurs at the micro-structural level (which needs not be molecular, see *e.g.* the buckling of the walls of a unit cell in a cellular solid – Bertoldi *et al.*, 2010; Gibson and Ashby, 1997). To investigate the physics of the mechanical hybrid character of spider capture thread, we performed mechanical tests on a single thread alongside microscopic observations of its microstructure. Figure 4.3 shows the relaxation of a freshly harvested biological sample. Starting from a stretched state (region I), the force-elongation curve shows that the thread behaves as a regular elastic solid undergoing relaxation: the monitored tension decreases almost linearly with the imposed displacement. In this regime, the capture thread adopts a classic drop-on-straight filament conformation, evocative of unduloidal-shaped drops sitting astride textile fibres (Adam, 1937), glass filaments (Quéré, 1999), mammalian hairs (Carroll, 1989), or feathers (Duprat *et al.*, 2012). But as relaxation proceeds further, the mechanical behaviour of the capture thread switches from solid to liquid. This sudden

change can be read directly from the mechanical testing: in region II, the recorded tension becomes virtually independent of the imposed displacement. This plateau tension is the typical signature of the response of liquid or soap films to tensile or compressive sollic-itations. Strikingly, this behavioural change coincides with a sharp modification of the micro-structure: while the overall composite remains taut, the core filament now buckles within each glue droplet (see close-ups Fig. 4.3). At even higher compressions, spools of slack filament form within the drops and keep on accumulating until eventually the overall tension falls (region III). Such spools have previously been observed in samples of post-mortem capture threads, but the physics underlying their formation, and in particular the potential roles of the filament molecular structure or of the glue viscoelasticity in this formation, has remained unclear so far (Foelix, 2010).
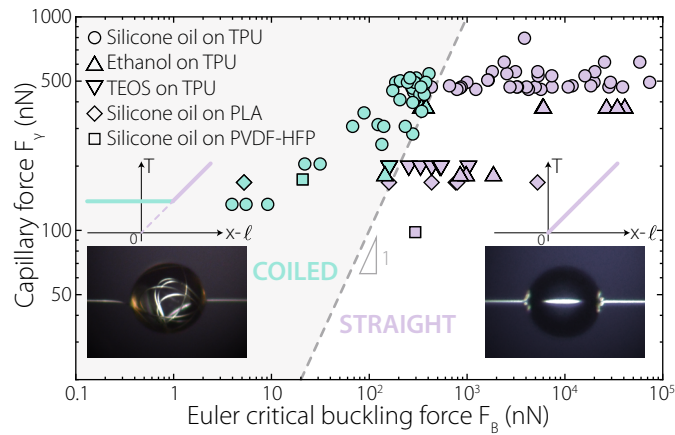
FIG. 4.4 – **Spooling activation.** In-drop spooling can also be achieved by synthetic fibres wet by droplets of various newtonian liquids. The phase diagram summarizes experiments performed with different materials and liquids in a quasi-static displacement-controlled setting. Each experiment consists in releasing the external tension on an initially taut sys-tem. Spooled or straight filament conformation are then observed within the droplets (blue or purple points respectively). These data demonstrate that the spooling threshold corre-sponds to a capillarity-induced buckling condition: spooling spontaneously occurs as soon as the capillary force exerted by the drop F_γ exceeds the Euler buckling load of the filament F_B. Note that, contrary to classic buckling, this spooling continues to proceed as long as the previous force condition is fulfilled, which suggests a subcritical nature for this elasto-capillary instability. The composite overall mechanical response (sketched in insets) also sharply changes past the threshold to exhibit a liquid-like plateau force.

▷ **Local in-drop buckling, global mechanical change.** The coincidence between the change in the mechanical responses of the capture thread at the global scale and the change in the conformations of the core filament at the drop scale is intriguing and requires further investigation. For so, let us consider a composite system consisting of a synthetic

core filament and of a liquid droplet, and examine the link between the global mechanical response of the system and the local filament geometry. Specifically we investigate the possibility of a buckling-induced activation of the composite. Surface tension is known to promote buckling (Neukirch *et al.*, 2007; Roman and Bico, 2010), snapping (see chapter 3 and Fargette *et al.*, 2014), or wrinkling (Huang *et al.*, 2007) of thin lamellar structures. In the drop-filament composite, and in absence of any external load, local buckling is initiated when the capillary force developed near each meniscus of a single drop $F_\gamma = 2\pi h \gamma \cos\theta$ exceeds the Euler buckling load $F_B = kEI/D^2$, where h, γ, θ, EI, D, and k denote respectively the filament radius, the liquid-air surface tension, the contact angle of the liquid on the filament, the bending stiffness of the core filament, the wet length, and the Euler buckling factor. The h^4 scaling of the filament's bending stiffness constitutes however a strong restriction for capillarity-induced buckling, typically limiting the manifestation of this phenomenon in filaments in the nm-μm range – thereby supporting the observed in-drop buckling of micronic spider capture threads, while explaining why hairs of 80 μm diameter do not buckle when wet, but rather simply clump (Bico *et al.*, 2004). This fully mechanical scenario, involving capillarity and elasticity as only ingredients, suggests that any drop sitting astride any filament could make it buckle, provided the force condition $F_\gamma > F_B$ is satisfied. To test this hypothesis, we conducted extensive experiments with various Newtonian liquid drops surrounding synthetic (i.e. non-biological) filaments of different diameters and made of diverse materials. Upon release of external tension, we found in-drop elastocapillary buckling to be indeed activated as soon as the capillary force overcomes the Euler buckling load, irrespective of the materials involved, see Fig. 4.4. Note that we have here used the value $k = \pi^2$ for the Euler buckling factor, expressing the fact that the fibre can freely rotate at the meniscii (simply supported buckling), see Elettro *et al.*, (2015b) for further details.

Before proceeding further, let's note that the geometry of slender elastic objects is known to control their mechanical response; a spring made of a thin metal wire has a markedly different mechanical response from the same wire having a straight conformation, and we could think of many manifestations of this link between geometry and mechanics (Audoly and Pomeau, 2010; Lazarus *et al.*, 2012). The composite under study here is no exception and we explain in the following how the in-drop filament geometry leads the thread to inherit the solid core filament mechanical properties when stretched, but the liquid drop properties when compressed.

4.4   Spooling and subcriticality

Contrary to conventional buckling, past the elastic instability threshold the core filament is not gently deformed but literally spooled and packed within the droplets, although the applied capillary force is constant. This behaviour, along with the localization of the bending deformation, are typical signatures of a subcritical instability. Furthermore, the global mechanical response of the composite changes instantly as soon as buckling is initiated at the drop scale: under large stretching, the composite behaviour is that of the core filament, but switches to that of a liquid film when compressed past the threshold.

Thus the droplets have the double role of storing the excess thread and putting the whole composite in a state of tension. This behaviour is all the more arresting because real liquid cylinders instantaneously disintegrate due to Rayleigh-Plateau instability, making the liquid-like response of the composite truly unusual.

FIG. 4.5 - **Why is there a tension?** Left: a drop can slide over a rigid fibre at no energetical cost, $\delta E = 0$. The tension in the fibre is therefore zero, as expected from the cancelling of the facing meniscus forces. Right: if some slack fibre is spooled inside the droplet, an energy is required to pull out the fibre from the droplet: the fibre is under tension.

▷ **Why is there a tension?** We mentioned (and experimentally observed) that capillary spooling implied fibre tension. But how does it work? After all, a single drop sitting astride a straight fibre exerts no net force on it: the two meniscus forces just cancel each other. Figure 4.5 left recasts this observation in terms of energy. Take a drop on a rigid fibre and impose a differential motion between the drop and the fibre so that the drop is displaced from a distance $\delta\ell$. The cost of wetting the small fibre is $2\pi h \Delta\gamma \delta\ell$ but this displacement also implies that a segment of length $\delta\ell$ is dewetted, corresponding to an energetical cost of $-2\pi h \Delta\gamma \delta\ell$: the drop can be displaced at no cost $\delta E = 0$, and the capillary tension in the fibre $\delta E/\delta\ell$ is equally nil. Now consider the situation depicted Fig. 4.5 right: a drop sitting on a fibre contains some slack. A differential motion between the fibre and the drop does not imply any more the same balance between wetting and dewetting as before. It is notably possible to unwind the fibre and extract a portion $\delta\ell$ from the drop without a dewetting event. The energy difference between the two configurations therefore amounts to $\left(-2\pi h \Delta\gamma - \frac{1}{2}EI\kappa^2\right)\delta\ell$, with κ the fibre curvature in the drop. Suppose further that a external force T assists the unrolling process. The work done by this force is naturally $-T\delta\ell$. The equilibrium condition requires these energies to cancel out, hence the force T to be non zero. In other words, the fibre is now under tension with $T = -2\pi h \Delta\gamma - \frac{1}{2}EI\kappa^2$.

▷ **A phase transition process.** To shed further light on the connection between the micro-structure and the global mechanical response, we continue to consider the simple

model pictured Fig. 4.5 but take into account the stretching properties of the thread and also the external force T introduced earlier. Elastocapillary spooling activation can be described as a phase transition between a wet and coiled phase – where the filament is entirely packed within the liquid drop – and a dry and extended phase – where the filament runs straight outside the drop. The extended phase is characterized by a stretching modulus EA and a rest length ℓ_e. Under an applied tension, its extension is $x_e = (1+\epsilon_e)\ell_e$, where ϵ_e is the extensional strain. The strain energy of the phase is then $\frac{1}{2}\ell_e EA\epsilon_e{}^2$, to which we add the solid-air interface energy $2\pi h\gamma_{sv}\ell_e$. The coiled phase is made up of the drop and the spooled filament inside the drop. The spools certainly adopt a complicated shape and the bending energy of the filament is $\frac{1}{2}EI\int_0^{\ell_c}\kappa(s)^2\,\mathrm{d}s$ where κ is the curvature of the filament and $I = \pi h^4/4$. Approximating the drop as spherical and the spools as arcs of circle, we write $\kappa = 2/D$ where D is the diameter of the drop. The bending energy is then $2\,\ell_c\,EI/D^2$. We note that in this approximation the extension of the phase $x_c = D$ is constant. We add the solid-liquid interface energy $2\pi h\gamma_{sl}\ell_c$ (the liquid-air interface energy, a constant, is not included) to obtain the total energy of the system $V = \left(\frac{1}{2}EA\epsilon_e{}^2 + 2\pi h\gamma_{sv}\right)\ell_e + \left(2\,EI/D^2 + 2\pi h\gamma_{sl}\right)\ell_c$. We replace ℓ_c and, discarding constant terms, re-write the total energy as $V = \left(\frac{1}{2}EA\epsilon_e{}^2 - 2\,EI/D^2 + 2\pi h\gamma\cos\theta\right)\ell_e$. Note that we have used Young-Dupré wetting relation $\gamma_{sv} - \gamma_{sl} = \gamma\cos\theta$, where θ is the liquid contact angle on the filament and γ the liquid-air interface energy per area. We note that the latent energy cost per unit length $\epsilon_0 = 2\pi h\gamma\cos\theta - \pi Eh^4/2D^2$ (already identified in the small introductory model) involved in the transformation from the coiled to the extended phase is a typical signature of a first-order phase transition problem. From this expression we readily obtain a condition for spooling to be sustained. Indeed, for the coiled phase to be stable at small forces ϵ_0 has to be positive (equivalently, the tension T has to be positive). This condition can be recast into a condition for the radius, where we recover the fact that only thin filaments exhibit in-drop spooling:

$$h < (4\gamma\cos\theta)^{1/3}\ E^{-1/3}\,D^{2/3} \tag{4.1}$$

Introducing the ratio $\rho = \ell_e/\ell$, we minimize V under the constraints of fixed extension $x = x_c + x_e$, and bounded ratio $0 \leq \rho \leq 1$. In the limit where $D \ll \ell$ and $\epsilon_0 \ll EA$, we find that the system can be entirely in the coiled phase ($\rho = 0$; filament fully packed in the drop) with tension $0 < T < \epsilon_0$, or entirely in the extended phase ($\rho = 1$) with tension $T = EA(x/\ell - 1) > \epsilon_0$. A third interesting possibility consists in a mixture of phases $0 < \rho < 1$. In this latter case, part of the filament is packed in the drop while the outer part is taut, consistent with our observations. As ρ is changed, the tension remains constant to a plateau value $T = T_P = \epsilon_0$, with

$$T_P = 2\pi h\gamma\cos\theta - \pi E\,h^4/2D^2 \tag{4.2}$$

To further explore the mechanical response of the composite system, we also performed detailed numerical computations of equilibrium of an inextensible and flexible elastic filament (Antkowiak *et al.*, 2011; Audoly and Pomeau, 2010; Elettro *et al.*, 2015b). The filament, held at both extremities with imposed distance x, is subjected to attracting meniscus forces F_γ at entrance and exit of a confining sphere. The loading (x, T) diagram,
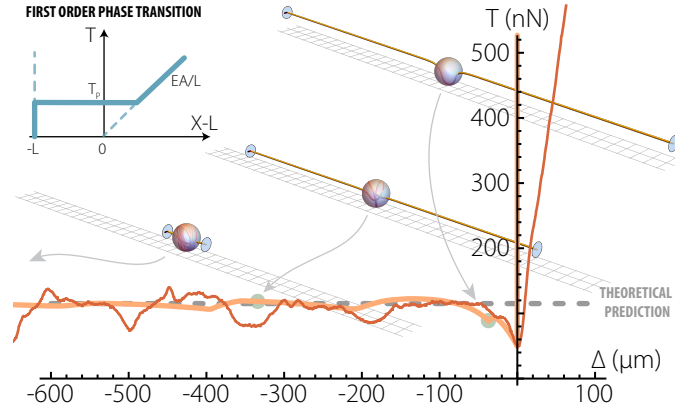
FIG. 4.6 – **Structural phase transition and detailed mechanical response.** Comparison between nano-Newton-resolved measurements on a composite polyurethane filament/silicone oil thread (red line), detailed simulations of an Elastica interacting with a droplet (orange line) and the first-order phase transition model (dashed grey line, full behavior also sketched in inset). Experiments were performed with a drop of wet length $D = 62 \pm 2\ \mu$m and a filament of radius $h = 1 \pm 0.2\ \mu$m and Young modulus $E = 17 \pm 3$ MPa. Numerical equilibria are here followed with a continuation procedure, with $F_\gamma = 35\ EI / D^2$ and $L = 20\ D$. The plateau tension T_P given by the phase transition model (4.2) is here 115 nN. Beyond the nice overall agreement, the results reveal a difference between the buckling threshold and the plateau tension. This difference points to the subcritical nature of elastocapillary buckling, also evidenced by the sudden localisation of the filament visible in the insets. The numerical simulations allow to capture the fine details in the micro-mechanical response observed in the experiments, resulting in inhomogeneities in the Maxwell plateau. Sensor drift forced us to adjust the reference level for the experimental measurements, but the level difference between buckling threshold and plateau tension is well recovered.

shown in Fig. 4.6, reveals inhomogeneities in the Maxwell line (Maxwell, 1875). These inhomogeneities are due to fine details in the micro-mechanical response of the system. Setting $F_\gamma = 2\pi h\gamma\cos\theta$, we plot in Fig. 4.6 the phase transition prediction given by Eq. (4.2), and we observe a nice agreement not only with the numerical computations, but also with nano-Newton-resolved mechanical testing of synthetic composites (here made of polyurethane filament and silicone oil droplet). We also note that both experiments and numerical simulations exhibit a kink between the two regimes that reveals a difference between the buckling threshold and the plateau tension, as already anticipated by our simple models and by the subcritical nature of the spooling (Fig. 4.4).

▷ **Post-buckling behaviour and subcriticality.** Capillary spooling is particularly striking because it is subcritical: the fibre remains straight up to the threshold, and then keeps on spooling just above. This binary behaviour is fully linked to the neat change

observed in the mechanical response of the fibre. But why is buckling in this configuration subcritical? From the simple models elaborated earlier we have already witnessed that the force needed to keep the spool packed was lower that the force needed to make it buckle. This behaviour was also apparent in the full numerical solutions (subcriticality being embodied with the kink in Fig. 4.6). But these elements, although consistent with subcriticality, do not explain its origin. In standard buckling, the force needed to deform the Elastica keeps on increasing past the buckling threshold, according to:

$$\frac{PL^2}{EI} = 4\pi^2 \left(1 + \frac{\Delta}{2L} \right),$$
(4.3)

where Δ is the imposed shortening (note that in this example we make use of clamped-clamped boundary conditions, but this is not important for the purpose of the argument, see Bažant and Cedolin, 2010, §1.9). This postbuckling behaviour is supercritical, or, equivalently, the system exhibits a positive stiffness past the threshold. Now, in spider capture silk, the situation is a bit different; the forces are exerted near the contact line (or more generally in a region where a surface energy gradient exists) but **the contact line is not attached to the fibre**. This means that the fibre can slide and enter the droplet while the force is still exerted at the drop boundary. This fundamental difference is at the root of subcriticality. Indeed, replacing in the previous equation the fibre length L with $D + \Delta$ – the length of the straight fibre traveling across the drop plus some slack – we can rewrite at first order equation (4.3) as:

$$\frac{PD^2}{EI} = 4\pi^2 \left(1 - \frac{3}{2}\frac{\Delta}{D} \right).$$
(4.4)

The change of sign in equation (4.4) has dramatic consequences, for now the system exhibits a negative stiffness: past the threshold, buckling, coiling and spooling can proceed without limit (until all the thread is gobbled or other phenomena such as e.g. steric effects show up). Buckling is now subcritical. Interestingly Bigoni and collaborators have designed a (macroscopic) experiment having similar ingredients: an Elastica is allowed to grow between fixed endpoints and suddenly snaps to a teardrop shape (see Fig. 4.7). Though the applied force is no more constant, there are similitudes with the fact that the forces are not following the Elastica tip, making the system subcritical.

▷ **A note on hybrid materials.** Hybrids made of different materials often display effective properties far exceeding those of their components (Ashby and Bréchet, 2003): zinc-coated steel is both strong and corrosion-resistant, metal foams (hybrids of metal and air) are stiff, light and crushable at the same time, making them perfect candidates to absorb energy in a car crash. Nature also provides many exquisite examples of hybrid design such as the seashell nacre, both stiff and tough thanks to its inner 'brick-and-mortar' structure composed of rigid, though brittle, inclusions surrounded by a crack arresting soft organic matrix, or the bamboo stem with its hollow core and honeycomb-shaped cells that maximize the ratio of bending rigidity over weight. Spider capture silk constitutes yet another example of such an hybrid material, here composed of liquid and

FIG. 4.7 - **Elastica dripping**. Bottom: an Elastica of variable length grows between end-points having a fixed separation distance. Past the buckling, the Elastica deforms up to self-contact where it adopts a teardrop shape. Top: for reference, the shape adopted by a falling drop (Bosi *et al.*, 2015).

solid, sometimes inheriting the properties of the solid, and sometimes those of the liquid. Note that, as in hybrids or in metamaterials, a classic effect acting at the micro-scale (sub-wavelength resonance or, as in here, in-drop buckling) reflects into a most striking and unusual phenomenon at the macro-scale.

▷ **Capillary spooling without spiders.** To conclude this chapter, let's remark that capillary spools, although forming naturally in spider webs, are not exclusive to spider (note by the way that the biological function of this spooling mechanism – if any – is still somewhat unclear. It could play a role in the web retention but this is an hypothesis). We demonstrated that this effect could be reproduced and exploited with synthetic materials, provided the fibre is sufficiently soft and/or thin. Note that this condition should particularly be met in soft biological objects, with e.g. the packing of DNA or RNA

in viral capsids for example. We could also mention an hypothetical model for the mor-

phology of elastin initially developed by Weis-Fogh and Andersen also involved a spooling mechanism at the protein level (pictured in inset – see Gordon, 1978, for an account). At the microscopic scale, other examples should abound if we know where to look. Figure 4.8 represents an amoeba gobbling a blue alga, which is gently packed and spooled within the amoeba. But at some point the alga violently springs out and explodes the amoeba (which then self-repairs). All these examples could be studied through the prism of the capillary spooling of thread in a single droplet. This micro-laboratory could help to understand and identify the different modes of packing and e.g. the fibre pressure exerted and the soft container.
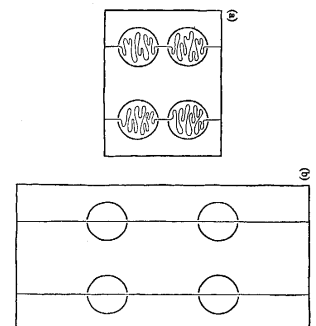
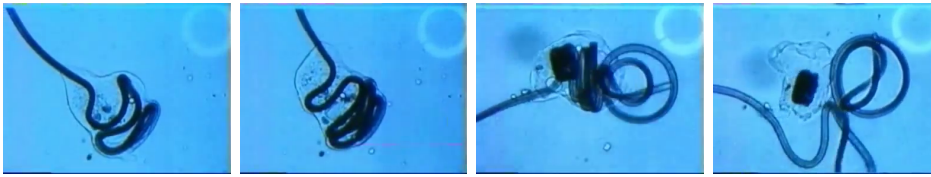FIG. 4.8 – **Amoeba vs alga**. An amoeba ingests a blue alga. In the process, the blue alga is spooled within the amoeba, but the amoeba cannot bear the alga pressure (resulting from the stored elastic energy), and the plant suddenly springs out and uncoils, tearing the amoeba apart in the process (from the TV documentary *"L'aventure des plantes"* by Jean-Marie Pelt and Jean-Pierre Cuny, 1986).

Perspectives

To end this manuscript I shall briefly outline three axes that will form the core of my research for the upcoming years. These axes arise from important questions/appealing prospects identified in former studies and also from opportunities, interactions with skilful and curious researchers and serenpidity. The three tracks will consist in extending and deepening our research on capillary spools, investigating the link between fast interfacial hydrodynamics and acoustics and finally studying the hydrodynamics of liquid films made of different chemical components.

▷ **Liquid wires.** The discovery we made during the PhD thesis of Hervé Elettro has prompted us to deepen our understanding of these liquid wires and also design new types of materials benefiting from these new mechanical functions. This is the purpose of an ANR grant we obtained recently and, within this framework, of the PhD thesis of Paul Grandgeorge (2015-2018). With Paul we investigate how our liquid wires could convey information, and be a vehicle for electricity or light. Among interesting possibilities, the capillary spooling mechanism allows for a fibre to exert a tension, and possibly on-demand. This is reminiscent of the functioning of sarcomeres in muscles and opens interesting perspectives in the area of artificial muscle fibres. Other tracks, including the extension to smart fabrics with novel properties are investigated as well. As these different research tracks require really different skills, we have started new and exciting collaborations with a chemistry lab (Natacha Krins, Laboratoire de Chimie de la Matière Condensée de Paris) and an optics lab in Lausanne (Kenny Hey Tow, Group For Fiber Optics, EPSL). Meanwhile our fruitful collaboration with the Oxford Silk Group and Fritz Vollrath continues in particular to unravel the biological function of the capillary spools.

▷ **Interfacial acoustics.** Bursting soap films (de Gennes, 1996), impacting raindrops or capillary jets forming from rupturing bubbles all exhibiting a fast dynamics, but still with velocities significantly lower than the sound speed, warrantying the accuracy of an incompressible description. Typically the Mach numbers (built with the celerity of sound in the air) of these fast interfacial dynamics can be of the order of 0.1, marking the

inception of weak compressible effects. During the postdoc of Adrien Bussonnière we analysed the acoustic

signature of such rapid capillary events in the context of a bursting soap bubble. Most interestingly we have been able to decipher the acoustic signals and measure the position of the bursting point, the bubble radius and even the film thickness profile, which noteworthy enough, is largely subwavelength. This exciting project, opening the way to measure not only forms but forces in fast interfacial hydrodynamics will be investigated with Régis Wunenburger, François Ollivier and Juliette Pierre from Institut d'Alembert.
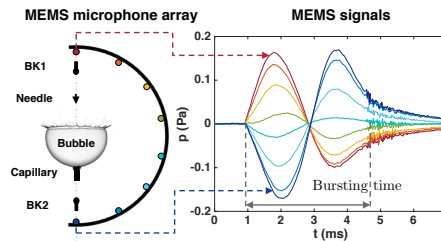
▷ **Heterogeneous liquid films hydrodynamics.** Part of my current research is performed in the Saint-Gobain/CNRS joint laboratory and focuses on the dynamics of heterogeneous thin liquid films, with application to the liquid coating of plane substrates. In the framework of this project, we pay particular attention to the way an heterogeneity in composition (typically a binary mixture composed

of a solvent and an other liquid) can drive thin film rupture or, conversely, smoothing of inhomogeneities through Marangoni forces. Recently there has been an upsurge of interest for the dynamics of evaporating binary droplets in the academic community. Indeed, though the thermodynamics of mixture and the forces resulting from surface tension contrasts are well known, the fluid dynamics of evolving mixtures exhibits phenomena previously unidentified. With this timely resonance between academic and industrial interests, a PhD thesis should start by the end of 2016. This project is in collaboration with Jérémie Teisseire, Alban Sauret and Pierre Jop from Saint-Gobain.
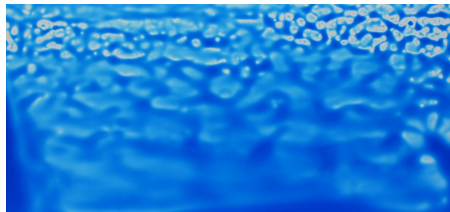
Literature Cited

Abkarian, M., G. Massiera, L. Berry, M. Roques, and C. Braun-Breton (2011). "A novel mechanism for egress of malarial parasites from red blood cells". *Blood* **117**(15), pp. 4118–4124.

Adam, N. K. (1937). "Detergent Action and its Relation to Wetting and Emulsification". *Journal of the Society of Dyers and Colourists* **53**(4), pp. 121–129.

Adamson, A. and A. Gast (1997). *Physical chemistry of surfaces.* John Wiley & Sons.

Antkowiak, A., B. Audoly, C. Josserand, S. Neukirch, and M. Rivetti (2011). "Instant fabrication and selection of folded structures using drop impact". *Proc. Natl Acad. Sci. U.S.A.* **108**(26), pp. 10400–10404.

Antkowiak, A., N. Bremond, S. Le Dizès, and E. Villermaux (2007a). "Short-term dynamics of a density interface following an impact". *J. Fluid Mech.* **577**, pp. 241–250.

Antkowiak, A., N. Bremond, J. Duplat, S. Le Dizès, and E. Villermaux (2007b). "Cavity jets". *Physics of Fluids* **19**(9).

Ashby, M. and Y. Bréchet (2003). "Designing hybrid materials". *Acta Materialia* **51**(19), pp. 5801–5821.

Audoly, B. and Y. Pomeau (2010). *Elasticity and geometry: from hair curls to the nonlinear response of shells.* Oxford University Press.

Bagnold, R. A. (1939). "Interim report on wave-pressure research". *J. Inst. Civil Eng.* 12. , pp. 201–226.

Batchelor, G. K. (1967). *An introduction to fluid dynamics.* Cambridge University Press.

Bažant, Z. P. and L. Cedolin (2010). *Stability of structures: elastic, inelastic, fracture and damage theories.* World Scientific.

Becker, N. *et al.* (2003). "Molecular nanosprings in spider capture-silk threads". *Nat. Mater.* **2**(4), pp. 278–283.

Bergmann, R., E. Dejong, J.-B. Choimet, D. Van Der Meer, and D. Lohse (2008). "The origin of the tubular jet". *J. Fluid Mech.* **600**, pp. 19–43.

Bertoldi, K., P. M. Reis, S. Willshaw, and T. Mullin (2010). "Negative Poisson's Ratio Behavior Induced by an Elastic Instability". *Adv. Mater.* **22**(3), pp. 361–366.

First experimental evidence of the relevance of pressure impulse in the description of liquid impact

Bico, J., B. Roman, L. Moulin, and A. Boudaoud (2004). "Adhesion: Elastocapillary coalescence in wet hair". *Nature* **432**(7018), pp. 690–690.

Birkhoff, G., D. P. MacDougall, E. M. Pugh, and S. G. Taylor (1948). "Explosives with Lined Cavities". *J. Appl. Phys.* **19(6). , pp. 563–582.**

Bisighini, A., G. E. Cossali, C. Tropea, and I. V. Roisman (2010). "Crater evolution after the impact of a drop onto a semi-infinite liquid target". *Phys. Rev. E* **82**, p. 036319.

Blackledge, T. A. *et al.* (2009). "Reconstructing web evolution and spider diversification in the molecular era". *Proc. Natl Acad. Sci. U.S.A.* **106**(13), pp. 5229–5234.

Blanchard, D. C. (1967). *From raindrops to volcanoes.* Doubleday.

Bonometti, T. and J. Magnaudet (2006). "Transition from spherical cap to toroidal bubbles". *Phys. Fluids* **18**(5), p. 052102.

Bosi, F., D. Misseroni, F. Dal Corso, and D. Bigoni (2015). "Self-encapsulation, or the 'dripping' of an elastic rod". *Proc. R. Soc. A* **471**(2179).

Boussinesq, J. (1877). *Essai sur la théorie des eaux courantes.* Imprimerie nationale.

Bowden, F. P. and M. P. McOnie (1965). "Cavities and Micro Munro Jets in Liquids: Their Role in Explosion". *Nature* **206(4982). , pp. 380–383.**

Boys, C. V. (1890). *Soap-bubbles and the forces which mould them. Being a course of three lectures delivered in the theatre of the London institution on the afternoons of Dec. 30, 1889, Jan. 1 and 3, 1890, before a juvenile audience.* Reprinted by Thomas Y. Crowell Company (1962).

Brujan, E.-A., K. Nahen, P. Schmidt, and A. Vogel (2001). "Dynamics of laser-induced cavitation bubbles near an elastic boundary". *J. Fluid Mech.* **433**, pp. 251–281.

Carroll, B. J. (1989). "Droplet formation and contact angles of liquids on mammalian hair fibres". *J. Chem. Soc., Faraday Trans. 1* **85**(11), pp. 3853–3860.

Cointe, R. (1989). "Two-Dimensional Water-Solid Impact". *J. Offshore Mech. Arct.* **111**(2), pp. 109–114.

Cooker, M. and D. H. Peregrine (1995). "Pressure-impulse theory for liquid impact problems". *J. Fluid Mech.* **297**, pp. 193–214.

Copeland, J. (1982). "Work–energy theorem for variable mass systems". *Am. J. Phys.* **50**(7), pp. 599–601.

Darrozès, J.-S. and C. François (1982). *Mécanique Des Fluides Incompressibles (Lecture Notes in Physics).* Springer-Verlag.

Davies, R. M. and G. Taylor (1950). "The Mechanics of Large Bubbles Rising through Extended Liquids and through Liquids in Tubes". *Proc. R. Soc. London A* **200**(1062), pp. 375–390.

de Gennes, P.-G., F. Brochard-Wyart, and D. Quéré (2003). *Capillarity and Wetting Phenomena: Drops, Bubbles, Pearls, Waves.* Springer.

de Gennes, P.-G. (1996). "Introductory lecture. Mechanics of soft interfaces". *Faraday Discuss.* **104. , pp. 1–8.**

First solid study on shaped-charge jets led by Birkhoff and Taylor and declassified after WWII

On the role of impact-driven jets in nitro-glycerine ignition

Interesting discussion on the energy losses occurring in a bursting soap film

Dear, J. P., J. E. Field, and A. J. Walton (1988). "Gas compression and jet formation in cavities collapsed by a shock wave". *Nature* **332**(6164), pp. 505–508.

Denny, M. (1976). "The physical properties of spider's silk and their role in the design of orb-webs". *J. Exp. Biol.* **65**(2), pp. 483–506.

DiPersio, R., J. Simon, and M. T. H. (1960). *A study of jets from scaled conical shaped charge liners.* **Tech. rep. . Army ballistic research laboratories – Aberdeen proving ground, Maryland.**

Duchemin, L., S. Popinet, C. Josserand, and S. Zaleski (2002). "Jet formation in bubbles bursting at a free surface". *Phys. Fluids* **14**(9), pp. 3000–3008.

Duprat, C., S. Protiere, A. Y. Beebe, and H. A. Stone (2012). "Wetting of flexible fibre arrays". *Nature* **482**(7386), pp. 510–513.

Eggers, J. and E. Villermaux (2008). "Physics of liquid jets". *Rep. Prog. Phys.* **71**(3).

Eggers, J. and M. A. Fontelos (2009). "The role of self-similarity in singularities of partial differential equations". *Nonlinearity* **22**(1), R1–R44.

Elettro, H., S. Neukirch, A. Antkowiak, and F. Vollrath (2015a). "Adhesion of dry and wet electrostatic capture silk of uloborid spider". *The Science of Nature* **102**(7-8).

Elettro, H., S. Neukirch, F. Vollrath, and A. Antkowiak (2016). "In-drop capillary spooling of spider capture thread inspires hybrid fibers with mixed solid–liquid mechanical properties". *Proc. Natl Acad. Sci. U.S.A.* **113**(22), pp. 6143–6147.

Elettro, H., F. Vollrath, A. Antkowiak, and S. Neukirch (2015b). "Coiling of an elastic beam inside a disk: A model for spider-capture silk". *Int. J. Nonlinear Mech.* **75**, pp. 59–66.

Engel, O. G. (1955). "Waterdrop collisions with solid surfaces". *J. Res. Nat. Bur. Stand.* **54(5). , pp. 281–298.**

Fargette, A., S. Neukirch, and A. Antkowiak (2014). "Elastocapillary Snapping: Capillarity Induces Snap-Through Instabilities in Small Elastic Beams". *Phys. Rev. Lett.* **112**, p. 137802.

Foelix, R. (2010). *Biology of spiders.* Oxford University Press.

Fontelos, M., J. Snoeijer, and J. Eggers (2011). "The Spatial Structure of Bubble Pinch-Off". *SIAM Journal on Applied Mathematics* **71**(5), pp. 1696–1716.

Föppl, A. (1897). *Vorlesungen über technische Mechanik.* B. G. Teubner, Leipzig.

Forterre, Y., J. M. Skotheim, J. Dumais, and L. Mahadevan (2005). "How the Venus flytrap snaps". *Nature* **433**(7024), pp. 421–425.

Foulk, C. (1932). "Foaming and Priming of Boiler Water". *Trans. Am. Soc. Mech. Eng. – Advance Papers* **54**(RP-54-5), pp. 105–113.

Frankel, I. and D. Weihs (1985). "Stability of a capillary jet with linearly increasing axial velocity (with application to shaped charges)". *J. Fluid Mech.* **155**, pp. 289–307.

Gay, C. and L. Leibler (1999). "On Stickiness". *Physics Today* **52**(11), pp. 48–52.

Gekle, S. and J. M. Gordillo (2010). "Generation and breakup of Worthington jets after cavity collapse. Part 1. Jet formation". *J. Fluid Mech.* **663**, pp. 293–330.

Experimental evidence of the linear velocity profile in shaped-charge jets

First use of cinematography in the study of drop impact

Ghabache, É., A. Antkowiak, C. Josserand, and T. Séon (2014a). "On the physics of fizziness: How bubble bursting controls droplets ejection". *Phys. Fluids* **26**(12),

Ghabache, É., T. Séon, and A. Antkowiak (2014b). "Liquid jet eruption from hollow relaxation". *J. Fluid Mech.* **761**, pp. 206–219.

Gibson, L. J. and M. F. Ashby (1997). *Cellular solids: structure and properties.* Cambridge university press.

Gordon, J. E. (1978). *Structures: or why things don't fall down.* Penguin books.

Gracias, D., V. Kavthekar, J. Love, K. Paul, and G. Whitesides (2002). "Fabrication of Micrometer-Scale, Patterned Polyhedra by Self-Assembly". *Adv. Mater.* **14**(3), pp. 235–238.

Guo, S. *et al.* (2013). "Direct Measurement of Friction of a Fluctuating Contact Line". *Phys. Rev. Lett.* **111**, p. 026101.

Hertz, H. (1884). "Über das Gleichgewicht schwimmender elastischer Platten". *Annalen der Physik* **258**(7), pp. 449–455.

Holmes, D. and A. Crosby (2007). "Snapping Surfaces". *Adv. Mater.* **19**(21), pp. 3589–3593.

Howison, S. D., J. R. Ockendon, and S. K. Wilson (1991). "Incompressible water-entry problems at small deadrise angles". *J. Fluid Mech.* **222**, pp. 215–230.

Huang, J. *et al.* (2007). "Capillary Wrinkling of Floating Thin Polymer Films". *Science* **317**(5838), pp. 650–653.

Joseph, D. D. (2006). "Potential flow of viscous fluids: Historical notes". *Int. J. Multiph. Flow* **32**(3), pp. 285–310.

Josserand, C. and S. Thoroddsen (2016). "Drop Impact on a Solid Surface". *Annu. Rev. Fluid Mech.* **48**(1), pp. 365–391.

Keller, J. B. and M. J. Miksis (1983). "Surface Tension Driven Flows". *SIAM Journal on Applied Mathematics* **43**(2), pp. 268–277.

Knight, R. C. (1936). "The potential of a sphere inside an infinite circular cylinder". *The Quarterly Journal of Mathematics* **os-7**(1), pp. 124–133.

Lake, G. J. and A. G. Thomas (1967). "The Strength of Highly Elastic Materials". *Proc. R. Soc. London A* **300**(1460), pp. 108–119.

Lamb, H. (1932). *Hydrodynamics.* Cambridge University Press.

Landau, L. D. and E. Lifshitz (1959). *Course of Theoretical Physics Vol 7: Theory and Elasticity.* Pergamon Press.

Laplace, P. S. de (1805). *Traité de mécanique céleste. Supplément au livre X.* Courcier, Paris.

Lapp, D. R. (2008). "Exploring 'extreme' physics with an inexpensive plastic toy popper". *Physics Education* **43**(5), p. 492.

Lavrentiev, M. and B. Chabat (1980). *Effets hydrodynamiques et modèles mathématiques.* Éditions MIR.

Layzer, D. (1955). "On the Instability of Superposed Fluids in a Gravitational Field." *The Astrophysical Journal* 122. , pp. 1–12.

Lazarus, A., H. C. B. Florijn, and P. M. Reis (2012). "Geometry-Induced Rigidity in Nonspherical Pressurized Elastic Shells". *Phys. Rev. Lett.* **109**, p. 144301.

A very simple potential model to describe the evolution of unsteady and nonlinear free surface flows is presented

Lorenceau, E., D. Quere, J.-Y. Ollitrault, and C. Clanet (2002). "Gravitational oscillations of a liquid column in a pipe". *Phys. Fluids* **14**(6), pp. 1985–1992.

Lundgren, T. S. and N. N. Mansour (1991). "Vortex ring bubbles". *J. Fluid Mech.* **224**, pp. 177–196.

Marchand, A., S. Das, J. H. Snoeijer, and B. Andreotti (2012). "Capillary Pressure and Contact Line Force on a Soft Solid". *Phys. Rev. Lett.* **108**, p. 094301.

Marchand, A., J. H. Weijs, J. H. Snoeijer, and B. Andreotti (2011). "Why is surface tension a force parallel to the interface?" *Am. J. Phys.* **79**(10), pp. 999–1008.

Maxwell, J. C. (1875). "On the dynamical evidence of the molecular constitution of bodies". *Nature* **11**, pp. 357–359.

— (1876). "Capillary action". *Encyclopædia Britannica* **5**.

Maxworthy, T. (1960). "Flame propagation in tubes". PhD thesis. Harvard University.

Milgram, J. H. (1969). "The motion of a fluid in a cylindrical container with a free surface following vertical impact". *J. Fluid Mech.* **37**, pp. 435–448.

Mirels, H. (1955). "laminar boundary layer behind shock advancing into stationary fluid." *NACA* **TN 3401**, 25p.

Munroe, C. E. (1888). "Modern explosives". *Scribners Magazine* **3**, p. 563.

Nethercote, W., M. Mackay, and B. Menon (1986). *Some warship slamming investigations.* Defence Research Establishment Atlantic.

Neukirch, S., A. Antkowiak, and J.-J. Marigo (2014). "Soft beams: When capillarity induces axial compression". *Phys. Rev. E* **89**, p. 012401.

Neukirch, S., A. Antkowiak, and J.-J. Marigo (2013). "The bending of an elastic beam by a liquid drop: A variational approach". *Proc. R. Soc. A* **469**(2157), p. 20130066.

Neukirch, S., B. Roman, B. de Gaudemaris, and J. Bico (2007). "Piercing a liquid surface with an elastic rod: Buckling under capillary forces". *J. Mech. Phys. Solids* **55**(6), pp. 1212–1235.

Oliver, J. M. (2002). "Water entry and related problems". PhD thesis. University of Oxford.

Omenetto, F. G. and D. L. Kaplan (2010). "New Opportunities for an Ancient Material". *Science* **329**(5991), pp. 528–531.

Peregrine, D. H. (2003). "Water-wave impact on walls". *Annu. Rev. Fluid Mech.* **35**(1), pp. 23–43.

Philippi, J., P.-Y. Lagrée, and A. Antkowiak (2016). "Drop impact on a solid surface: short-time self-similarity". *J. Fluid Mech.* **795**, pp. 96–135.

Plesset, M. S. and A. Prosperetti (1977). "Bubble Dynamics and Cavitation". *Annu. Rev. Fluid Mech.* **9**(1), pp. 145–185.

Popinet, S. (2000). "Stabilité et formation de jets dans les bulles cavitantes". PhD thesis. Université Pierre et Marie Curie.

— (2003). "Gerris: a tree-based adaptive solver for the incompressible Euler equations in complex geometries". *J. Comp. Phys.* **190**(2), pp. 572–600.

Popinet, S. (2009). "An accurate adaptive solver for surface-tension-driven interfacial flows". *J. Comp. Phys.* **228**(16), pp. 5838–5866.

Poulter, T. C. and B. M. Caldwell (1957). "The development of shaped charges for oil well completion". *Petroleum Transactions* **210**.

Py, C. *et al.* (2007). "Capillary Origami: Spontaneous Wrapping of a Droplet with an Elastic Sheet". *Phys. Rev. Lett.* **98**(15), p. 156103.

Quéré, D. (1999). "Fluid coating on a fiber". *Annu. Rev. Fluid Mech.* **31**(1), pp. 347–384.

Rein, M. (1993). "Phenomena of liquid drop impact on solid and liquid surfaces". *Fluid Dyn. Res.* **12**(2), pp. 61–93.

Reis, P. M., J. Hure, S. Jung, J. W. M. Bush, and C. Clanet (2010). "Grabbing water". *Soft Matter* **6**, pp. 5705–5708.

Richard, D., C. Clanet, and D. Quéré (2002). "Surface phenomena: Contact time of a bouncing drop". *Nature* **417**(6891), pp. 811–811.

Rioboo, R., M. Marengo, and C. Tropea (2002). "Time evolution of liquid drop impact onto solid, dry surfaces". *Exp. Fluids* **33**(1), pp. 112–124.

Rivetti, M. and A. Antkowiak (2013). "Elasto-capillary meniscus: pulling out a soft strip sticking to a liquid surface". *Soft Matter* **9**(27), pp. 6226–6234.

Roman, B. and J. Bico (2010). "Elasto-capillarity: deforming an elastic structure with a liquid droplet". *J. Phys. Condens. Matter* **22**(49), p. 493101.

Schlichting, H. (1968). *Boundary-layer theory.* McGraw-Hill series in mechanical engineering. New York: McGraw-Hill.

Schmieden, C. (1953). "Der Aufschlag von Rotationskörpern auf eine Wasseroberfläche. Richard v. Mises zum 70. Geburtstag gewidmet". *ZAMM - Z. Angew. Math. Mech.* **33**(4), pp. 147–151.

Séon, T. and A. Antkowiak (2012). "Large Bubble Rupture Sparks Fast Liquid Jet". *Phys. Rev. Lett.* **109**, p. 014501.

Seveno, D., T. D. Blake, and J. De Coninck (2013). "Young's Equation at the Nanoscale". *Phys. Rev. Lett.* **111**, p. 096101.

Shaw, L. L., S. A. Muelder, D. W. Baum, and K. A. Winer (1994). "Hypervelocity Explosive-Driven Metal Jet in Air". *Phys. Fluids* **6**(9), S10–S10.

Sneddon, I. N. (1960). "The elementary solution of dual integral equations". *Glasgow Mathematical Journal* **4**, pp. 108–110.

— (1995). *Fourier Transforms.* Dover.

Sommerfeld, A. (1952). *Mechanics.* Vol. I. Lectures on Theoretical Physics. Academic Press.

Stokes, G. (1851). "On the Effect of the Internal Friction of Fluids on the Motion of Pendulums". *Transactions of the Cambridge Philosophical Society* **9**, p. 8.

Stow, C. D. and M. G. Hadfield (1981). "An Experimental Investigation of Fluid Flow Resulting from the Impact of a Water Drop with an Unyielding Dry Surface". *Proc. R. Soc. A* **373**(1755), pp. 419–441.

Stow, C. D. and R. D. Stainer (1977). "The Physical Products of a Splashing Water Drop". *J. Meteor. Soc. Japan. Ser. II* **55**(5), pp. 518–532.

Interesting analysis of the shape of transient jets

Stuhlman, O. J. (1932). "The Mechanics of Effervescence". *Physics* 2(6). , pp. 457–466.

Style, R. W. *et al.* (2013). "Universal Deformation of Soft Substrates Near a Contact Line and the Direct Measurement of Solid Surface Stresses". *Phys. Rev. Lett.* **110**, p. 066103.

Sun, Y., S. Fry, D. Potasek, D. Bell, and B. Nelson (2005). "Characterizing fruit fly flight behavior using a microforce sensor with a new comb-drive configuration". *J. Microelectromech. Syst.* **14**(1), pp. 4–11.

A review paper on the technological applications of surface-tension-driven folding in the microfabrication area

Syms, R., E. Yeatman, V. Bright, and G. Whitesides (2003). "Surface tension-powered self-assembly of microstructures - the state-of-the-art". *J. Microelectromech. Syst.* 12(4). , pp. 387–417.

Tagawa, Y. *et al.* (2012). "Highly Focused Supersonic Microjets". *Phys. Rev. X* **2**, p. 031002.

Thompson, J. M. T. (1982). "'Paradoxical' mechanics under fluid flow". *Nature* **296**(5853), pp. 135–137.

Timoshenko, S. P. (1935). "Buckling of Flat Curved Bars and Slightly Curved Plates". *J. Appl. Mech.* **2**, pp. 17–20.

van der Bos, A. *et al.* (2014). "Velocity Profile inside Piezoacoustic Inkjet Droplets in Flight: Comparison between Experiment and Numerical Simulation". *Phys. Rev. Applied* **1**, p. 014004.

Van Dyke, M. D. (1975). *Perturbation methods in fluid dynamics.* Parabolic Press.

Villermaux, E. and B. Bossa (2011). "Drop fragmentation on impact". *J. Fluid Mech.* **668**, pp. 412–435.

Vincent, O. *et al.* (2011). "Ultra-fast underwater suction traps". *Proc. R. Soc. B* **278**(1720), pp. 2909–2914.

Vollrath, F. and D. T. Edmonds (1989). "Modulation of the mechanical properties of spider silk by coating with water". *Nature* **340**(6231), pp. 305–307.

Vollrath, F. (1992). "Spider webs and silks." *Scientific American* **266**(3), pp. 70–76.

Wagner, H. (1932). "Über Stoß- Gleitvorgange an der Oberflache von Flussigkeiten (Phenomena Associated with Impacts and Sliding on Liquid Surfaces)". *ZAMM - Z. Angew. Math. Mech.* **12**(4), pp. 193–215.

Walters, J. K. and J. F. Davidson (1963). "The initial motion of a gas bubble formed in an inviscid liquid – Part 2. The three-dimensional bubble and the toroidal bubble". *J. Fluid Mech.* **17**(03), pp. 321–336.

Woodcock, A. H., C. F. Kientzler, A. B. Arons, and D. C. Blanchard (1953). "Giant Condensation Nuclei from Bursting Bubbles". *Nature* **172**(4390), pp. 1144–1145.

Work, R. W. (1977). "Dimensions, Birefringences, and Force-Elongation Behavior of Major and Minor Ampullate Silk Fibers from Orb-Web-Spinning Spiders— The Effects of Wetting on these Properties". *Textile Research Journal* **47**(10), pp. 650–662.

Worthington, A. (1908). *A study of splashes.* Longmans, Green and co.

Xu, L., W. W. Zhang, and S. R. Nagel (2005). "Drop Splashing on a Dry Smooth Surface". *Phys. Rev. Lett.* **94**(18), pp. 184505–4.

Yafetto, L. *et al.* (2008). "The Fastest Flights in Nature: High-Speed Spore Discharge Mechanisms among Fungi". *PLoS ONE* **3**(9), e3237–.

Zeff, B. W., B. Kleber, J. Fineberg, and D. P. Lathrop (2000). "Singularity dynamics in curvature collapse and jet eruption on a fluid surface". *Nature* **403**(6768), pp. 401–404.